Entry no. 64

Analysis and Visualization of Tissue-motion of Cranial Ultrasonogram Image Sequences for Newborn Babies

By

Muhammad Muinul Islam

A thesis submitted in partial fulfillment of the requirement for the degree of
Master of Science in Electrical and Electronic Engineering

Khulna University of Engineering & Technology
Khulna 9203, Bangladesh

May 2011

Entry No. 64

Declaration

This is to certify that the thesis work entitled " **Analysis and Visualization of Tissue-motion of Cranial Ultrasonogram Image Sequences for Newborn Babies** " has been carried out by **Muhammad Muinul Islam** in the Department of Electrical and Electronic Engineering, Khulna University of Engineering & Technology, Khulna, Bangladesh. The above thesis work or any part of this work has not been submitted anywhere for the award of any degree or diploma.

18/5/2011
Signature of Supervisor

18.05.11
Signature of Candidate

Approval

This is to certify that the thesis work submitted by *Muhammad Muinul Islam* entitled "*Analysis and Visualization of Tissue-motion of Cranial Ultrasonogram Image Sequences for Newborn Babies*" has been approved by the board of examiners for the partial fulfillment of the requirements for the degree of M.Sc. Engineering in the Department of *Electrical and Electronic Engineering*, Khulna University of Engineering & Technology, Khulna, Bangladesh in May 2011.

BOARD OF EXAMINERS

1. _____ Chairman
Prof. Dr. Mohiuddin Ahmad (Supervisor)
Dept. Electrical and Electronic Engineering
Khulna University of Engineering & Technology
Khulna-9203

2. _____ 18.05.11 Member
Prof. Dr. Md. Abdur Rafiq
Head, Dept. of Electrical and Electronic Engineering
Khulna University of Engineering & Technology
Khulna-9203

3. _____ 18/5/11 Member
Prof. Dr. Md. Rafiqul Islam
Dept. of Electrical and Electronic Engineering
Khulna University of Engineering & Technology
Khulna-9203

4. _____ 18.05.11 Member
Prof. Dr. Md. Abdur Rafiq
Dept. of Electrical and Electronic Engineering
Khulna University of Engineering & Technology
Khulna-9203

5. _____ 18/05/11 Member
Prof. Dr. Md. Al-Amin Bhuiyan (External)
Dept. of Computer Science & Engineering
Jahangirnagar University
Dhaka

ACKNOWLEDGEMENTS

First of all, I acknowledge my gratitude and thanks to almighty ALLAH for successful completion of my thesis.

I am indeed fortunate to have work under the guidance of Prof. Dr. Mohiuddin Ahmad. His contagious suggestions, encouragement, patience, originality and desired to succeed have helped me complete this thesis. His proper guidelines, inspiration and helpful contribution in the research work and spent-time played a vital role in completion this thesis work. Dr. Mohiuddin Ahmad is an intellectual in tissue motion analysis and comprehension. He is the source of vast ideas, profound knowledge and feedback all the time for authors. For all of these the author gratefully acknowledges his profound indebtness to him.

I would like to thank Professor Dr. Md. Rafiqul Islam, Dean, Faculty of Electrical & Electronic Engineering, KUET for his advice and inspiration to work under Dr. Mohiuddin Ahmad.

I am very thankful to professor Dr. Md. Abdur Rafiq, head of the department, Electrical & Electronic Engineering, KUET, for his suggestion, encouragement and providing the departmental facilities for completion of this work.

I am also grateful to Professor Dr. Md. Al-Amin Bhuiyan, Chairman, Department of Computer Science & Engineering, Jahangirnagar University, Dhaka -1342, Bangladesh, for his valuable discussion and suggestions to complete this work.

Furthermore, I would like to thank all the faculty members of Electrical & Electronic Engineering Department, KUET for helping in various ways in formulating this dissertation.

Finally, I would like to thank my parents for being the ultimate source of strength and encouragement throughout my academic career and personal life and particularly to my wife who has always supported my education with her love and encouragement.

Abstract

Cranial ultrasound scans are very essential part of the routine investigation of neonatal intensive care. The scan ultrasound image sequence are not only used for real-time diagnosis but also recorded as moving images in video recorder as ultrasonographic movie for future diagnosis, offline analysis of ultrasonogram images and the study of tissue velocity in neonatal cranium. The tissue motion in neonatal cranium is an important physical parameter which is considered in discussing the pulsation strength of newborn baby for pediatric diagnosis. The artery pulsation has a strong correlation with the blood flow in the newborn baby head and tissue-motion has a relationship with artery pulsation. Optical flow technique finds an excellent application in determining the tissue motion velocity quantitatively in cranial ultrasonogram of newborn baby.

Cranial ultrasonogram of newborn babies for different coronal and sagittal sections are studied and the tissue motion velocity of neonatal cranium is analyzed using the optical flow techniques. In order to calculate tissue motion velocity, gradient-based approaches of optical flow techniques with different optical flow optimizations are used. Ultrasonogram image sequences of 32 frames, 640×480 pixels/frame, 8bits/pixel, 33 ms/frame for different coronal and sagittal sections are used. Whole ultrasonogram is not useful for analysis and small portion of ultrasonogram images are selected during analysis in the region inside cranial bone. Tissue- motions are estimated in different coronal sections and their errors are also estimated.

Further, the time variant tissue-motions are analyzed using discrete Fourier transform of optical flow velocity. The pulsation is observed in the time variant tissue motion images and strong pulsation is occurred in the harmonic frequencies of tissue-motion that has a relation to the heartbeat frequency of a newborn baby which is helpful for pediatric diagnosis.

Pulsation amplitudes, caused by artery pulsation due to blood flow are also analyzed and visualized from a video stream of ultrasound image sequence by using 1D fast Fourier transform in brightness mode for future diagnosis using direct pixel value. A new imaging technique, named pulsation amplitude image is proposed. In the proposed method, the tissue motion of typical coronal and sagittal sections of normal and asphyxiated neonates are analyzed and visualized. Significant differences have been observed in cranial tissue motion between normal and abnormal neonate. The results obtained in the present study lead to determine pulsation amplitude that strongly contribute pediatricians in diagnosis of newborn baby's ischemic diseases.

Contents

LIST OF TABLES

LIST OF FIGURES

List of Abbreviation

ACA	Anterior cerebral artery
BPM	Beat per minute
CBF	Cerebral blood flow
CNS	Central nervous system
CT	Computed tomography
CUS	Cranial ultrasonography
CLG	Combined Local and Global
DFT	Discrete Fourier transform
FT	Fourier transform
FFT	Fast Fourier transform
GF	Global flow
HIE	Hypoxic-ischemic encephalopathy
IVH	Intraventricular hemorrhage
LBW	Low birth weight
LF	Local flow
MRI	Magnetic resonance imaging
OFC	Optical flow constraint
OI	Original image
MCA	Middle cerebral artery
PVL	Periventricular leukomalacia
PDE	Partial differential equation
ROI	Region of Interest
Th	Threshold
USG	Ultrasonogram

CHAPTER 1

Introduction

1.1 Medical Ultrasound

Ultrasonography is an imaging technique in which deep structures of the body are visualized by recording the reflections (echoes) of ultrasonic waves directed into the tissues. The use of ultrasound in medical application can be divided into two major areas, the therapeutic and the diagnostic. In therapeutic application, the systems operate at ultrasonic power level up to several watts per square centimeter while the diagnostic equipment operates properly at power levels below $100\ mW/cm^2$. The therapeutic equipment is designed to agitate the tissue to the level where the thermal heating occurs in the tissue. Diagnostic Medical ultrasonography is an imaging technique hereby high-frequency acoustic energy is transmitted into the human body using transducers in contact with the skin. The ultrasound waves produced by the transducer reflect from boundaries between organs and surrounding fluid, and between regions of differing tissue density and are used to visualize subcutaneous body structures including tendons, muscles, joints, vessels and internal organs for possible pathology. For diagnostic purposes, as long as a sufficient amount of signal has returned for electronic processing, no additional energy is necessary. Diagnostic ultrasounds are used in two modes: either in continuous waves or in the pulse wave mode. Fetal heart detector and blood flow measuring instruments are based on continuous-wave mode. Echocardiograph works on pulse-wave mode. Using this it can be scan brain tumor, diameter of eye ball and retinal detachment. Neonatal cranial ultrasonogram is a regular part of neonatal intensive care unit. From ultrasonogram movie or ultrasonogram image sequence the neonatal brain tissue motion can be observed. Observations are used in real time diagnosis and also recorded as moving images in video tapes as ultrasonographic movie for future diagnosis. It plays a role in decisions on continuation or withdrawal of intensive treatment.

1.2 State of the art

Despite the major advances in monitoring technology and knowledge of fetal and neonatal pathologies, perinatal asphyxia or, more appropriately, hypoxic-ischemic encephalopathy (HIE), remains a serious condition that causes significant mortality and long-term morbidity. The incidence of hypoxic-ischemic encephalopathy is reportedly high in countries with limited resources; however, precise figures are not available. Birth asphyxia

is the cause of 23% of all neonatal deaths worldwide. It is one of the top 20 leading causes of burden of disease in all age groups (in terms of disability life adjusted years) by the World Health Organization and is the fifth largest cause of death of children younger than 5 years (8%). Although data are limited, birth asphyxia is estimated to account for 920,000 neonatal deaths every year and is associated with another 1.1 million intrapartum stillbirths. More than a million children who survive birth asphyxia develop problems such as cerebral palsy, mental retardation, learning difficulties, and other disabilities [1]. Perinatal asphyxia results in hypoxic injury to various organs including kidneys, lungs and liver but the most serious effects are seen on the central nervous system (CNS) [2]. Hypoxic ischemic encephalopathy (HIE) refers to the CNS dysfunction associated with perinatal asphyxia. HIE is the foremost concern in an asphyxiated neonate because of its potential to cause serious long-term neuromotor squeal among survivors. Hypoxic-ischemic encephalopathy is characterized by clinical and laboratory evidence of acute or sub-acute brain injury due to asphyxia (i.e. hypoxia, acidosis). Most often, the exact timing and underlying cause remain unknown. Brain hypoxia and ischemia due to systemic hypoxemia, reduced cerebral blood flow (CBF), or both are the primary physiological processes that lead to hypoxic-ischemic encephalopathy [1]. Good supportive care is essential in the first 48 hours after asphyxia to prevent ongoing brain injury in the penumbra region [2].

A key point of diagnosis of Ischemic disease whether there is the artery pulsation accompanied with blood flow or not [3] [4]. Tissue motion in neonatal cranium is an important physical parameter that is considered in discussing the pulsation strength of newborn baby for pediatric diagnosis. Ultrasonography is widely used in observing different organs in human body due to its convenience, easy to use and low cost in compared with magnetic resonance imaging (MRI) and X-ray computed tomography (CT). In general, observations are recorded as stationary images by medical doctors for medical diagnosis. Observations are also recorded as moving images in video tapes as ultrasonographic movie for future diagnosis. In case of newborn baby, the pediatricians can observe the brain tissue by ultrasonography, since they can observe the brain tissue through the anterior fontanelle [4].

Pediatricians use an ultrasonogram to find the cranial abnormalities in a newborn baby. Scanning of cranial ultrasound is an essential part of the routine investigation during neonatal intensive care. The scan ultrasound image sequences are not only used for real-

time diagnosis but also recorded for future diagnosis. In this thesis brain tissue motion due to artery pulsation in neonatal cranium has been tried to analyze quantitatively in case of both normal and asphyxiated neonate from cranial ultrasonogram image sequences to assist pediatricians for early detection of ischemia.

The main point of pediatric diagnosis is the intensity of pulsation associated with blood flow [4]. In order to detect artery pulsation from a series of noisy ultrasound echo images of a newborn baby head for pediatric diagnosis, a digital image processing system was developed by using an algorithm based on Fourier transform [4]. In this method, the time sequence variations of each pixel value in a series of moving images were analyzed. In order to observe artery pulsation in neonatal cranium at the site of diagnosis, a real-time processing system was developed for continuous detection and display of artery pulsation from moving images of neonatal cranial ultrasonogram [5]. For clinical diagnosis of neonatal cranial diseases, a real-time processing of ultrasound-echo moving images was used by using a one dimensional processor array system [6]. By using artery pulsation image, the distribution of artery pulsation was analyzed in cranial ultrasonogram of newborn babies with intraventricular hemorrhage (IVH) [7]. All the algorithms used above were mainly based on the time sequence variation of pixel value in a series of ultrasound echo images. But the pixel value can be easily varied. Therefore, the above methods were very sensitive to the brightness of the B-mode ultrasonogram movie. The brightness can be easily varied by the condition in taking ultrasonographic movie or by the pediatricians.

Optical flow is widely used for analysis of object motion in image sequences. Several optical flow approaches are available for analyzing the velocities of tissue motion, such as matching based approach and gradient-based approach. The gradient-based methods [8]-[11] that utilize spatial and temporal derivatives of image brightness to form a gradient constraint equation for the estimation of two dimensional motion field find diverse applications in many situations including computer vision as well as video processing and coding.

Being compared to different approaches of optical flow technique, gradient based approach is better than matching based approach because matching based approach is computationally impractical to estimate matches for a large number of points and matching based approach is highly sensitive to ambiguity among the structures to be matched [11].

In gradient based approach, two optimization methods are available, global optimization method and local optimization method. In global optimization method, the velocity field is determined by minimizing an error function which is based on the gradient constraint and a global smoothing term over the whole image [12]. But in local optimization method, no extra smoothing operator is needed. It works within a very small region. Therefore, gradient based approach with local optimization method was used to calculate the tissue motion velocity at each pixel over the ultrasonographic movie. Since tissue motion velocities are not large, so gradient based method may work well. Using optical flow with local optimization technique, tissue motions were quantitatively analyzed due to artery pulsation accompanied with blood flow in neonatal cranial ultrasonogram [13]. But both local and global optimization method have some disadvantages. Local optical flow optimization is very robust under noise but does not yields dense flow field and global optical flow optimization yields dense flow field but very sensitive to noise. So, combined local global (CLG) optical flow can overcome the difficulty of either local or global flows [14].

In this thesis, the tissue-motion due to artery pulsation in cranial ultrasound image sequences has been analyzed by using different optical flow techniques, which are not sensitive to image brightness change. This is very helpful for quantitative characterization of tissue motion velocity. Moreover, the time variant tissue-motions are analyzed by using Fourier transform, emphasizing that the tissue motion at a particular frequency. Time sequence variation of optical-flow velocities are presented for characterizing tissue motion velocities with blood flow. The tissue motion velocities were assumed periodic. The periodicity was observed easily by using Fourier transform analysis. The Fourier transform analysis may be done by discrete Fourier transform (DFT) or fast Fourier transform (FFT). The analyses of tissue-motion of different coronal and sagittal sections and visualization of the tissue-motion in B-mode ultrasonogram images can be very useful for assisting medical doctors especially pediatricians in the diagnosis of ischemic diseases of neonatal cranium.

1.3 Objectives

This research will modernize the study of cranial ultrasonogram of newborn baby and make experiments in the field of biomedical engineering, integrating modern techniques and information.

The objective of this work is to develop some analytical tools for medical diagnosis of premature newborn babies easily or to detect disease easily and transfer the advanced technology to others.

In other sense, it will help pediatricians from engineering point of view. The specific objectives of the proposed research work are summarized as follows:

- Propose a new imaging technique named pulsation-amplitude image
- Detect and analyze tissue-motion from ultrasound image sequence and find relation of pulsation strength with artery pulsation.
- Develop software facilities for quantitative characterization of brain tissue motion.
- Visualize the brain tissue-motion caused by artery pulsation of blood flow from a video stream of ultrasonogram in brightness mode for future diagnosis.

1.4 Thesis Outlines

The thesis is organized as follows:

Chapter 2: This chapter contains the background knowledge on the Ultrasonogram basic principle and neonatal cranial ultrasonography of different coronal and sagittal sections.

Chapter 3: In this chapter the prepossessing of ultrasonogram image sequences such as filtering, region of interest selection etc are discussed.

Chapter 4: In this section the brain tissue motion velocities are analyzed using optical flow techniques and the frequency of brain tissue motion velocity are analyzed using Fourier transform of optical flow velocity for different coronal and sagittal sections. Afterward the brain tissue motions are analyzed with Fourier transform using direct pixel value of B-mode ultrasonogram image sequences for different coronal and sagittal sections.

Chapter 5: This section contains the visualization of the brain tissue motion using optical flow techniques and Fourier transform of optical flow velocity for different coronal and sagittal sections. The brain tissue motions are also visualized with Fourier transform using direct pixel value of B-mode ultrasonogram image sequences for different coronal and sagittal sections.

Chapter 6: Finally the thesis concludes with some closing remarks and directions of further research in this chapter.

CHAPTER 2

Neonatal Cranial Ultrasonography

2.1 Introduction

Cranial ultrasonography (CUS) was introduced into neonatology in the late 1970s and has become an essential diagnostic tool in modern neonatology. The non-invasive nature of ultrasonography makes it an ideal imaging technique in the neonate. In the neonate and young infant, the fontanels and many sutures of the skull are still open, and these can be used as acoustic windows to "look" into the brain [15]. Ultrasonogram is routinely used at the various sites of medical diagnosis because of its convenience, easy to use, low cost in compared with magnetic resonance imaging (MRI) and X-ray computed tomography (CT). Scanning of cranial ultrasound is essential part of the routine investigation during neonatal intensive care. As a result of ongoing development in ultrasonography, image quality is high nowadays and it provides optimal settings and techniques which are applied. Therefore, CUS is a reliable tool for detecting congenital and for acquiring anomalies of the perinatal brain and the most frequently occurring patterns of brain injury in both preterm and full-term neonates.

2.2 Ultrasonography

Ultrasonography is an imaging technique in which deep structures of the body are visualized by recording the reflections (echoes) of ultrasonic waves directed into the tissues. Frequencies in the range of 1MHz to 10MHz are used in diagnostic ultrasonography. The lower frequencies provide a greater depth of penetration and are used to examine abdominal organs; those in the upper range provide less penetration and are used predominantly to examine more superficial structures such as the eye. Ultrasonography is a procedure in which high-frequency sound waves that cannot be heard by human ears are bounced off internal organs and tissues. These sound waves produce a pattern of echoes that are then used by the computer to create sonograms or pictures of areas inside the body. Ultrasonogram is routinely used at the various sites of medical diagnosis because of its convenience, easy to use, low cost in compared with magnetic resonance imaging (MRI) and X-ray computed tomography (CT). Scanning of cranial ultrasound is essential part of the routine investigation during neonatal intensive care. In diagnostic ultrasonography the ultrasonic waves are produced by electrically stimulating a piezoelectric crystal called a transducer. As the beam strikes an interface or boundary

between tissues by varying acoustic impedance (e.g. muscle and blood) some of the sound waves are reflected back to the transducer as echoes. The echoes are then converted into electrical impulses that are displayed on an oscilloscope, presenting a 'picture' of the tissues under examination.

2.2.1 Continuous wave Doppler ultrasonography

In a continuous wave Doppler system, a sound wave is continuously transmitted and received with two different transducers. The transmitted and reflected beams begin to overlap a short distance from the surface of the probe, and the overlap extends until the beams attenuate. When several vessels are focused within the sensitive volume, the Doppler signals are superimposed and detected simultaneously. Continuous Doppler ultrasonography is not dependent on the depth of the location and speed of the blood flow.

2.2.2 Pulsed wave Doppler ultrasonography

A Doppler system with range resolution allows the selection of location where the Doppler signals are obtained. This is possible by sending the ultrasound waves in pulses and thus only waves from certain areas return back before the next pulse is transmitted. In order to analyze reflected waves during a certain time period after pulse transmission, it is possible to set a sample volume located in predetermined range. The axial length of the sample volume is determined by the time period when the gate is open. Changing frequency of waves, which are reflected from a moving target, limits the use of pulsed Doppler. The maximum measurable Doppler shift frequency is related to half of the pulse repetition frequency (Nyquist limit). The pulse repetition frequency must be increased with high velocities, and thus the depth reached by the ultrasound decreases. The velocity of the blood flow and the depth of the object are limitations of pulsed Doppler ultrasonography.

2.2.3 Color Doppler ultrasonography

Phase quadrature detection in the demodulators enables the observer to distinguish between higher or lower received signals from the transmitted frequency, corresponding to Doppler shifts toward or away from the transducer. Flow toward the transducer is visually demonstrated as red and flow away from the transducer as blue, and non-moving targets remain grey. The saturation of the color is related to the velocity of the flow. The limitations of color flow imaging are similar to pulsed Doppler ultrasonography.

2.2.4 3D ultrasound

3D ultrasound is a medical ultrasound technique, often used during pregnancy, providing three dimensional images of the fetus. Often these images are captured rapidly and animated to produce a "4D ultrasound". In 3D fetal scanning, however, instead of the sound waves being sent straight down and reflected back, they are sent at different angles. The returning echoes are processed by a sophisticated computer program resulting in a reconstructed three dimensional volume image of fetus's surface or internal organs; in much the same way as a CT scan machine constructs a CT scan image from multiple x-rays. 3D ultrasounds allow one to see width, height and depth of images, in much the same way as 3D movies but no movement is shown. *4D* ultrasounds involve the addition of movement by stringing together frames of 3D ultrasounds in quick succession. 3D ultrasound was first developed by Olaf von Ramm and Stephen Smith at Duke University in 1987. Clinical use of this technology is an area of intense research activity especially in fetal anomaly scanning. There are also popular uses that have been shown to improve fetal-maternal bonding. 4D baby scans are similar to 3D scans except that they show fetal movement as shown in the video clip.

2.3 Cranial Ultrasonography

Neurosonographers use transducers to perform sonograms on areas of the nervous system, however, the frequencies they use, are beam of different shapes than those that are used by abdominal or obstetric sonographers. By scanning blood vessels in the brain and nervous system, they can check for abnormalities that can be indicative of a potential stroke or brain aneurysm. Scans can be performed in order to examine the inner structure of the brain as well as to find abnormal tumors or masses that may be cause the patients to have abnormal symptoms.

Cranial ultrasound usually is done only on babies:

- As a part of routine screening of babies, born prematurely to detect bleeding in the brain, such as intraventricular hemorrhage (IVH).
- To monitor any complications or to detect periventricular leukomalacia (PVL). IVH and PVL increase a baby's risk of developing disabilities, including cerebral palsy or mental retardation.
- To screen brain problems that may be present from birth (such as congenital hydrocephalus).
- To evaluate an enlarging head.

- To detect infection or abnormal growths in or around the brain.
- In adults, cranial ultrasound may be done during brain surgery to help for locating a brain mass.

2.4 Capturing of Neonatal Cranial Ultrasonogram

Neurosonographers may work in the area of neonatal care at hospitals in the Neonatal Intensive Care Units. They perform sonograms on premature infants and assist doctors with the diagnosis of neurological and nervous system disorders. They can scan fetuses' brains for the purpose of diagnosing brain disease or other related health problems. Sonograms are used on infants to determine abnormalities such as congenital defects, intracranial hemorrhage, or hyrdocephalus. Neonatal neurosonographers can also work with infants who have been diagnosed with sickle cell anemia, scanning their blood vessels in order to check for abnormalities that may be indicative of a stroke. Sonographers generally capture the neonatal cranial ultrasonogram movie or image using Port-Royal method. Port-Royal method is used to capture the ultrasonogram image in different planes of neonatal cranium. In this method an ultrasonic probe is placed on the anterior fontanelle of a neonate as shown in figure 2.1. Figure 2.2 shows tissue scheme in the anterior coronal section of a neonatal cranium. Willis ring, middle cerebral artery (MCA), anterior cerebral artery (ACA), and fine arteries around corpus callosum are illustrated in the figure 2.2.

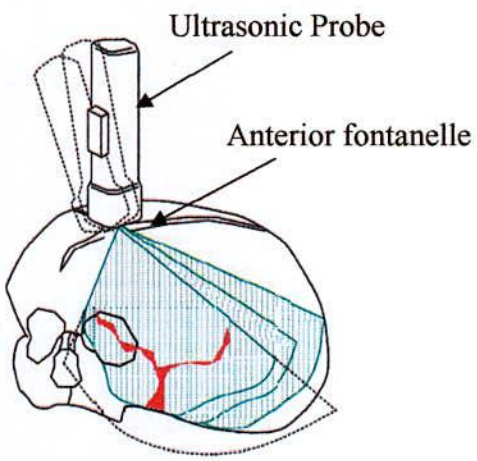

Figure 2.1: Placement of ultrasonic probe on the anterior fontanelle of a neonate

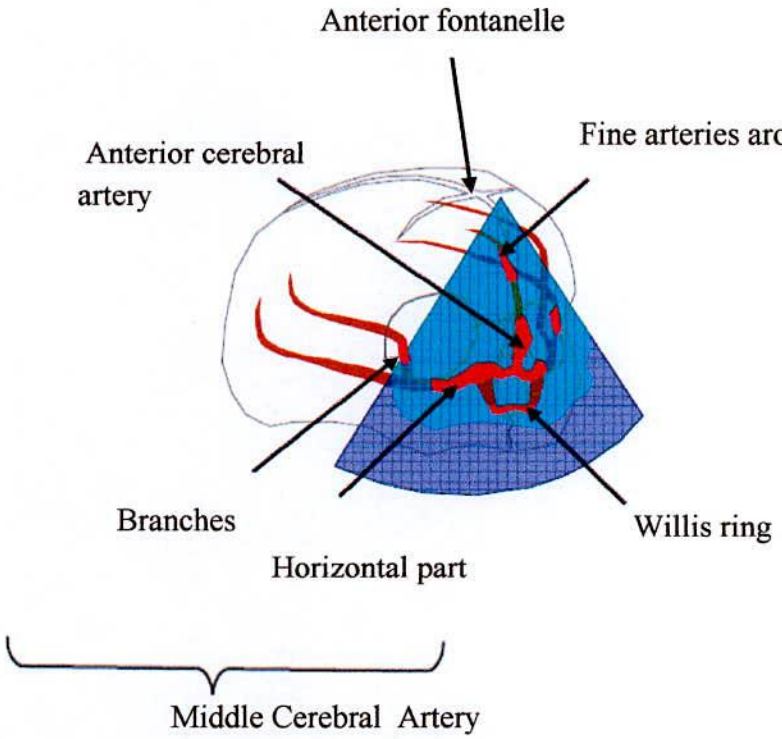

Figure 2.2: Tissue scheme in the anterior coronal section f a neonatal cranium.

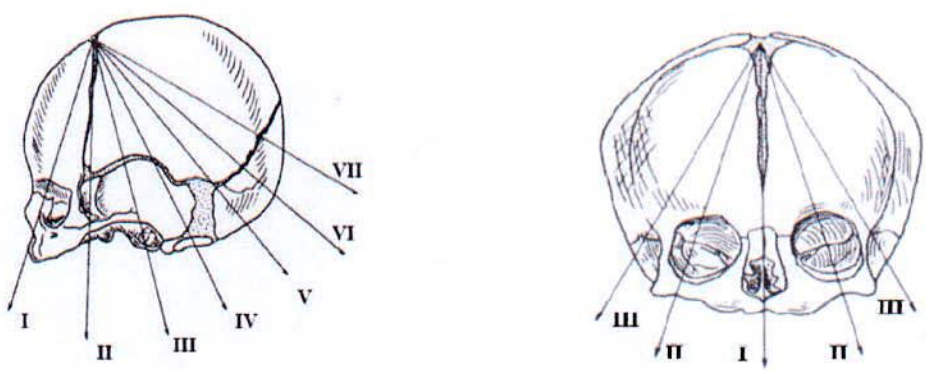

(a) (b)

Figure 2.3: Different scanned sections. (a) Coronal sections. (b) Sagittal sections.

Different coronal and sagittal sections are shown in Table 2.1 and Table 2.2, respectively. Since, coronal section 2 (anterior coronal section) contains more tissues and organs, then anterior coronal section can be assumed as reference coronal section. Similarly, midline sagittal section contains more tissues and organs, and this section can be regarded as reference sagittal section. Each section contains special arteries and organs. We show the

angular displacement of each section with Ref. coronal and sagittal section. Different coronal and sagittal sections are shown in the Figure 2.3.

Table 2.1: Seven coronal section

Section	Name	Angle with Ref.
I	Frontal	18°
II	Anterior coronal	Ref.
III	Coronal through foramen of Monro	18°
IV	Coronal through foramen magnum	28°
V	Slightly posterior coronal	42°
VI	Posterior Coronal	52°
VII	Most posterior coronal	62°

Table 2.2: Five sagittal sections

Section	Name	Angle with Ref.
I	Midline sagittal	Ref.
LII	Lateral sagittal, left	17°
RII	Lateral sagittal, right	37°
LIII	Most lateral sagittal, left	18°
RIII	Most lateral sagittal, right	38°

2.5 Coronal sections

We have mentioned that seven coronal sections are scanned. The coronal series is performed by scanning through the anterior fontanelle. Scans are made starting interiorly and by working posteriorly. The transducer is angled to the back of the head for the more posterior scans. We have shown the brain tissue, ultrasonogram image and essential organs for each section [3, 33].

2.5.1 Frontal

The brain tissue, ultrasonogram image and essential organs of Frontal are given in Fig. 2.4. The legends of essential tissues corresponding to the number in Fig. 2.4(c) are as follows:

1. Falx cerebri-interhemispheric fissure
2. Frontal lobe
3. Cribriform lobe
4. Orbit

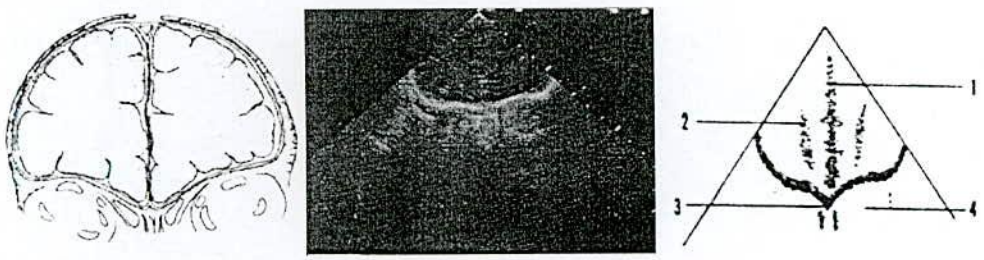

(a) (b) (c)

Figure 2.4: (a) Brain tissue, (b) ultrasonogram image and (c) essential organs of Frontal.

2.5.2 Anterior coronal

The brain tissue, ultrasonogram image and essential organs of anterior coronal are shown in Fig. 2.5. The legends of essential tissues corresponding to the number in Fig. 2.5(c) are as follows:

1. Corpus callosum
2. Lateral ventricle frontal horn
3. Head of caudate nucleus
4. Sylvian fissure
5. Lenticular nucleus
6. Middle cerebral artery
7. Body of sphenoid bone
8. Temporal lobe

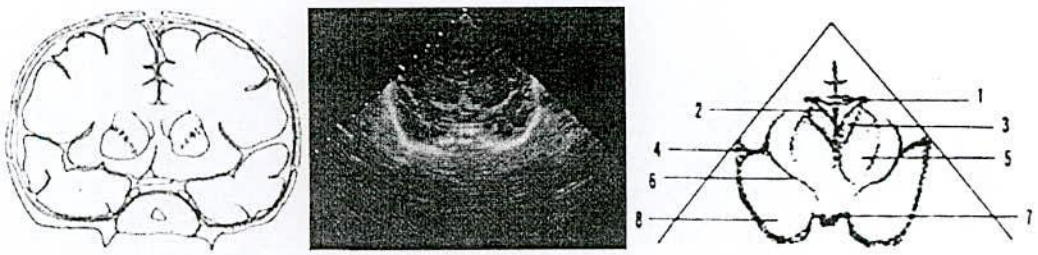

(a) (b) (c)

Figure 2.5: (a) Brain tissue, (b) ultrasonogram image and (c) essential organs of anterior coronal.

2.5.3 Coronal through the foramen monro

The brain tissue, ultrasonogram image and essential organs of Coronal through the foramen monro are shown in Fig. 2.6. The legends of essential tissues corresponding to the number in Fig. 2.6(c) are as follows:

1. Lateral ventricle
2. Choroid plexus foramen of monro
3. Third ventricle

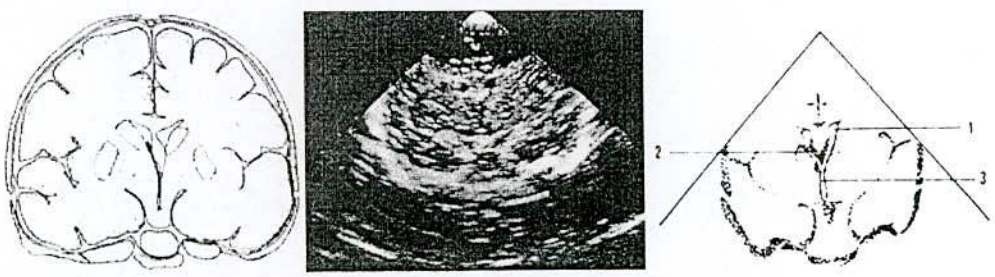

(a) (b) (c)

Figure 2.6: (a) Brain tissue, (b) ultrasonogram image and (c) essential organs of Coronal through the foramen monro.

2.5.4 Coronal through the foramen magnum

The brain, ultrasonogram image and tissues of Coronal through the foramen magnum are shown in Fig. 2.7. The legends of essential tissues corresponding to the number in Fig. 2.7(c) are as follows:

1. Falx cerebri interhemispheric fissure
2. Corpus callosum
3. Lateral ventricle body
4. Sylvian fissure
5. Third ventricle

6. Thalamus
7. Squamoparietal suture
8. Hippocampal gyrus
9. Pars petrosa

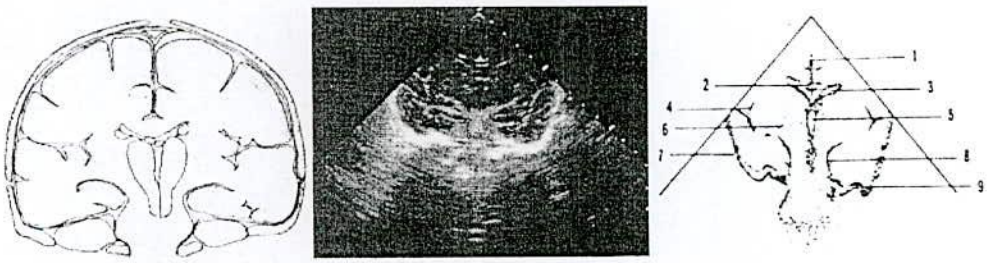

(a) (b) (c)

Figure 2.7: (a) Brain tissue, (b) ultrasonogram image and (c) essential organs of Coronal through the foramen magnum

2.5.5 Slightly posterior coronal

The brain tissue, ultrasonogram image and essential organs of slightly posterior coronal are shown in Fig. 2.8.

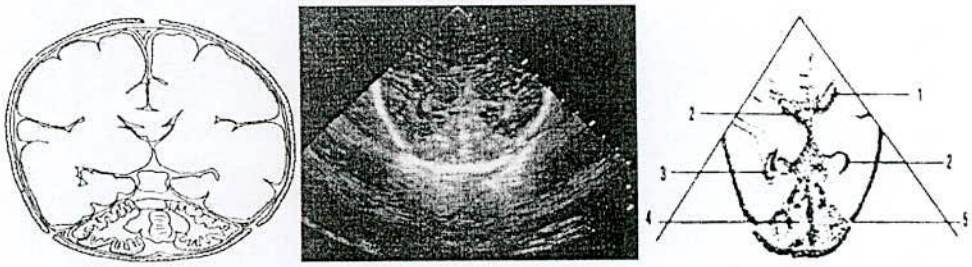

(a) (b) (c)

Figure 2.8: (a) Brain tissue, (b) ultrasonogram image and (c) essential organs of slightly posterior coronal.

The legends of essential tissues corresponding to the number in Fig. 2.8(c) are as follows:

1. Lateral ventricle (body)
2. Choroid plexus
3. Lateral ventricle(inferior horn)
4. Cerebellum
5. Lambdoid suture

2.5.6 Posterior coronal

The brain tissue, ultrasonogram image and essential organs of Posterior coronal are shown in Fig. 2.9.

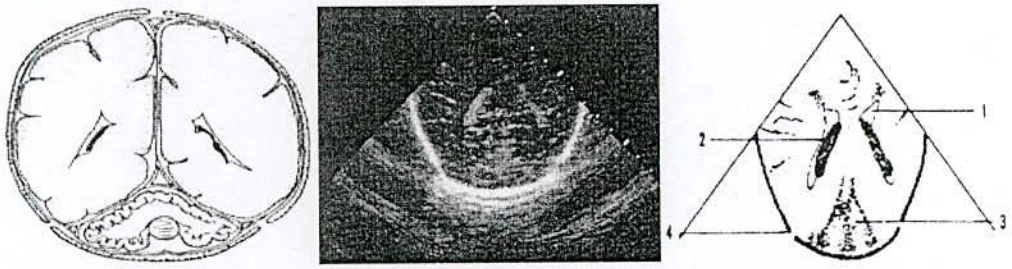

(a) (b) (c)

Figure 2.9: (a) Brain tissue, (b) ultrasonogram image and (c) essential organs of Posterior coronal.

The legends of essential tissues corresponding to the number in Fig. 2.9(c) are as follows:

1. Lateral ventricle
2. Choroid plexus
3. Cerebellum
4. Lambodoid suture

2.5.7 Most posterior coronal

The brain tissue, ultrasonogram image and essential organs of most posterior coronal are shown in Fig. 2.10.The legends of essential tissues corresponding to the number in Fig. 2.9(c) are as follows:

1. Falx ceribri-interhemispheric fissure
2. Occipital lobe
3. Lambodoid suture

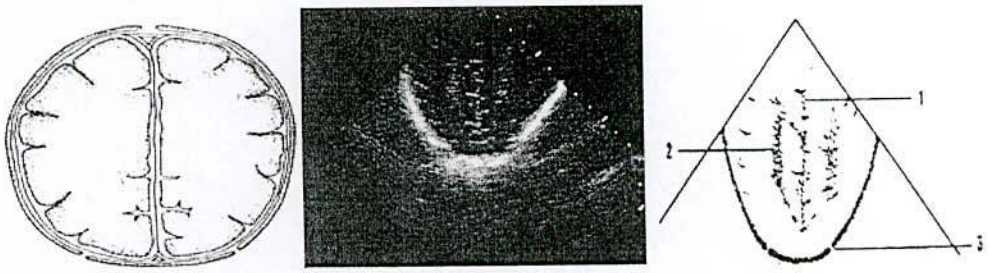

(a) (b) (c)

Figure 2.10: (a) Brain tissue, (b) ultrasonogram image and (c) essential organs of Most Posterior coronal.

2.6 Sagittal sections

Sagittal scans are easily obtained with the sector real-time transducer by scanning through the anterior fontanels. A midline scan is obtained to demonstrate the third and fourth ventricles. By angling the transducer to direct at right and left the lateral ventricles can be imaged. We have mentioned that three sagittal sections are scanned. For each section we have shown the brain tissue, ultrasonogram image and essential organs for each section [3].

2.6.1 Midline sagittal

The brain tissue, ultrasonogram image and essential organs of Midline sagittal are shown in Fig. 2.11. The legends of essential tissues corresponding to the number in Fig. 2.11(c) are as follows:

1. Corpus callosum
2. Choroid plexus
3. Foramen of monro
4. Third ventricle
5. Aqueduct of sylvius
6. Optic recess
7. Clivus
8. 4^{th} ventricle
9. Cerebellum
10. Pons
11. Cistern magna
12. Foramen magnum

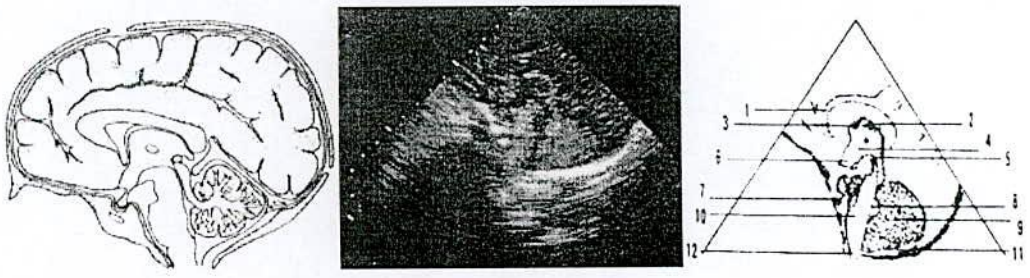

(a) (b) (c)

Figure 2.11: (a) Brain tissue, (b) ultrasonogram image and (c) essential organs of Midline sagittal.

2.6.2 Lateral sagittal

The brain tissue, ultrasonogram image and essential organs of Lateral sagittal are shown in Fig. 2.12. The legends of essential tissues corresponding to the number in Fig. 2.12(c) are as follows:

1. Lateral ventricle
2. Head of caudate nucleus
3. Thalamocaudate notch
4. Anterior cranial fossa (pars orbitalis)
5. Thalamus
6. Choroid plexus
7. Middle cranial fossa(pars petrosa)
8. Lambdoid suture
9. Cerebellum
10. Posterior cranial fossa (occipital bone)

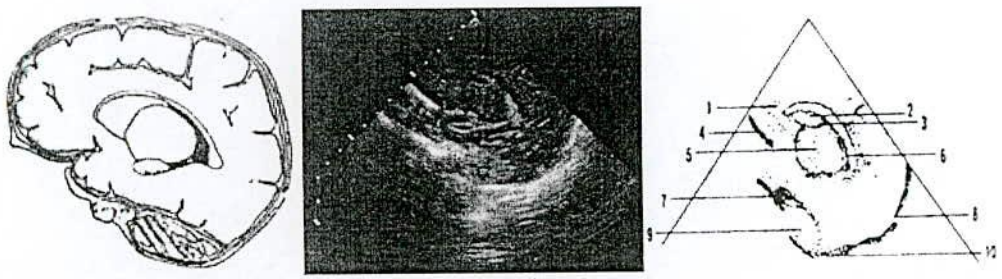

(a) (b) (c)

Figure 2.12: (a) Brain tissue, (b) ultrasonogram image and (c) essential organs of Lateral sagittal.

2.6.3 Most lateral sagittal

The brain tissue, ultrasonogram image and essential organs of most lateral sagittal are shown in Fig. 2.13.

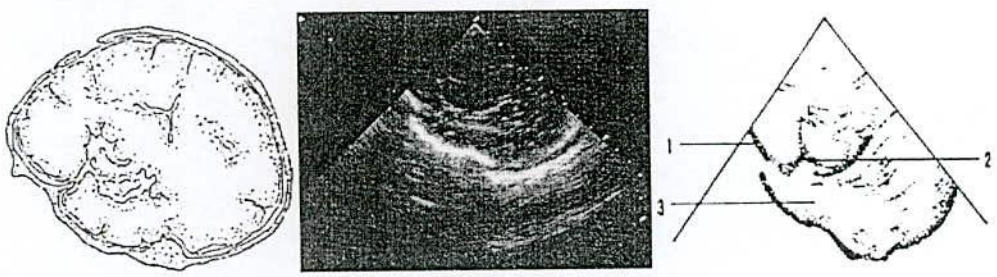

(a) (b) (c)

Figure 2.13: (a) Brain tissue, (b) ultrasonogram image and (c) essential organs of Most lateral sagittal.

The legends of essential tissues corresponding to the number in Fig. 2.13(c) are as follows:

1. Anterior cranial fossa
2. Sylvian fissure
3. Temporal lobe

2.7 Tissue with pulsation motion:

All tissues in the neonatal cranium do not contain pulsation tissue motion due to blood flow in artery. For the analysis of tissue motion it is necessary to know the tissues with pulsation motion in different coronal and sagittal section. Table 2.3 shows typical tissues with pulsation motion in major coronal section and Table 2.4 shows typical tissues with pulsation motion in major sagittal sections.

Table 2.3: Typical tissues with pulsation motion in major coronal sections.

No.	Section name	Tissues with pulsation motion
I	Frontal	falx cerebri, interhemispheric fissure
II	Anterior coronal	MCA(horizontal), ACA, Sylvian fissure, corpus callosum
III	Coronal through the foramen of Monro	MCA, lateral ventricle, foramen of Monro
IV	Coronal through the foramen magnum	MCA(branch), lateral ventricle
V	Slightly posterior coronal	MCA(branch), lateral ventricle, choroid plexus, cerebellum
VI	Posterior coronal	lateral ventricle, choroid plexus
VII	Most posterior coronal	falx cerebri, interhemispheric fissure

Table 2.4. Typical tissues with pulsation motion in major sagittal sections.

No.	Section name	Tissues with pulsatile or pulsation motion
I	Middle sagittal	corpus callosum, cerebellum, MCA, ACA, etc.
II	Lateral sagittal	lateral ventricle, choroid plexus, cerebellum
III	Most lateral sagittal	anterior cranial fossa, Sylvian fissure, temporal lobe

CHAPTER 3

Preprocessing of ultrasonogram image sequences

3.1 Critical situations during capturing ultrasonogram image sequences

At the time of capturing ultrasonogram movie, some critical situations may happened, such as

- Sway of the ultrasound probe: USG probes may not be in proper alignment with the desired sector of scan, in that case we will unable to get actual image. Expert Neuro sonographer is needed for obtaining good results.
- Sway of the head of baby: During capturing the USG movie a helper should physically hold the infant's head in place thereby maintaining the correct positioning for various views
- Discontinuity of the image frames, and
- Complete dark or bright of any image frame in the sequence.

These critical conditions of ultrasonographic images are avoided because they produce large errors in calculation. In order to avoid the critical conditions, the ultrasonogram was taken carefully with a constant brightness condition and contrast while fixing the position of ultrasound probe.

3.2 Noise elimination

Today ultrasound and magnetic resonance imaging are essential tools for noninvasive medical diagnosis. One of the fundamental problems in this field is speckle noise, which is a major limitation on image quality especially in ultrasound imaging. The presence of the speckle noise affects image interpretation by human and the accuracy of computer-assisted diagnostic techniques. Low image quality is an obstacle for effective feature extraction, analysis, recognition and quantitative measurements. The key point in effective speckle noise removing is balance between speckle suppression and feature preservation. Diffusion filter is an effective technique for goal achievement. Behind this, development is solution of partial differential equation (PDE) of transient permeability for 2D domain. Due to its nonlinear nature and adaptive anisotropy, the filter has excellent properties of both speckle reduction and detail preserving properties. Effective realization of the diffusion algorithm allows using of the filter for real-time image processing in medical and industrial devices. Another widely used despeckle technique is the median filter. The

advantage of the median filter is its simplicity and algorithmic straightforwardness. But due to its nonadaptive nature, it deteriorates not only speckles but details as well.

3.3 Region of Interest (ROI) selection

For any section, the whole ultrasonogram consists of the following item:

- Tissue with organs
- Cranial bone or other bone
- Echo artifact

The ultrasonogram image of different coronal and sagittal sections are different. Whole ultrasonogram is not useful for analysis. That is why small portion of ultrasonogram images are selected during analysis. The ultrasonographic images are of conic shapes but according to the structure of cranial bone various types of ROI are used. Such as oval shape, hexagonal shape, discrete line type etc. The region inside cranial bone was considered as the ROI for both coronal and sagittal sections. In Figure 3.1 one typical coronal and sagittal sectional ultrasonographic image with the region of interest were shown. The ROIs are indicated by the bright regions in the Figure 3.1 (b) and (d). The Figure 3.1(b) shows the ROI of the anterior coronal section and Figure 3.1(d) shows the ROI of the lateral sagittal (right) section

The cranial bone and the echo artifacts were not included in the ROI because

- There is no artery in the cranial bone
- Echo artifacts which are echo images that appear on the image posterior to the cranial bone that do not correspond to the location or intensity to the actual interfaces in the neonatal cranium

For calculating the absolute value of tissue motion velocity, only the region inside cranial bone was considered because the portion contains only tissues and organs.

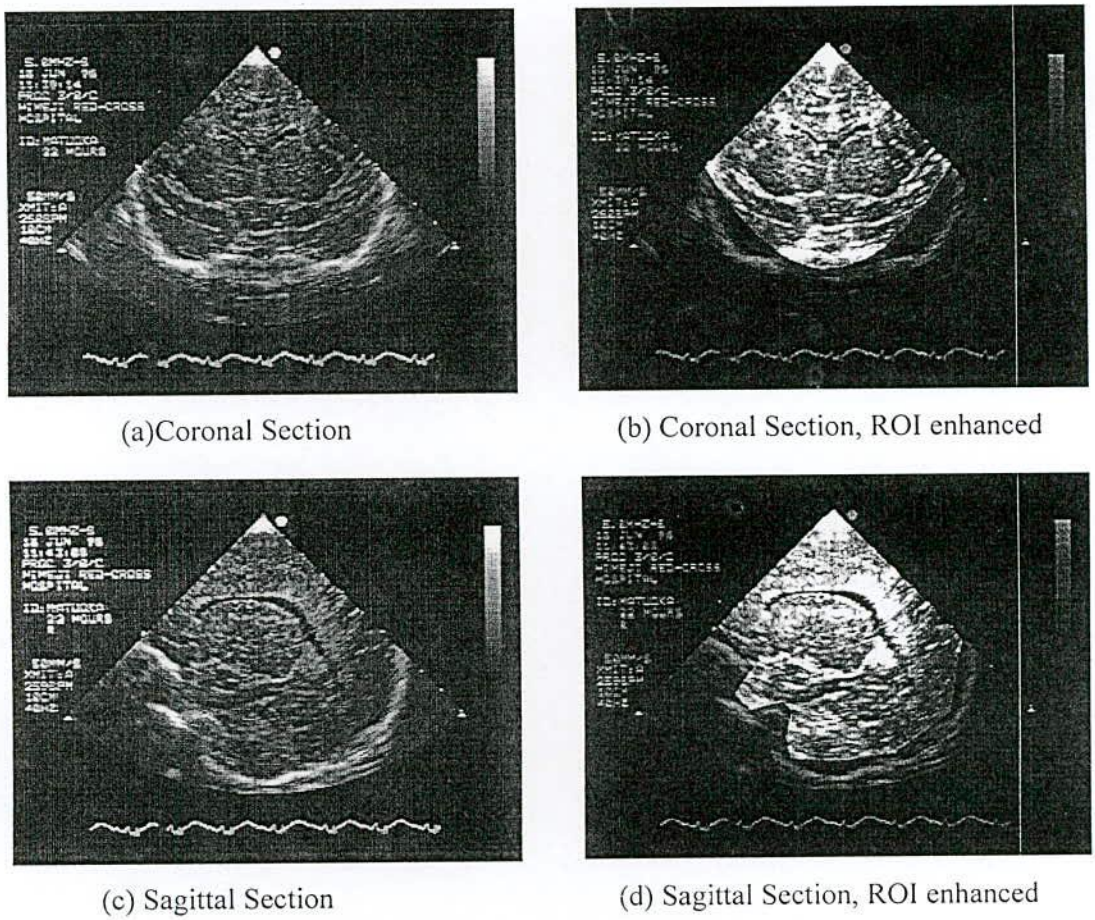

(a)Coronal Section

(b) Coronal Section, ROI enhanced

(c) Sagittal Section

(d) Sagittal Section, ROI enhanced

Figure 3.1: Original Ultrasonographic images of coronal and sagittal sections with mask inside the cranial bone. Regions of interest (ROI) are shown as bright region in the images (b) and (d)

3.4 Masking

Since entire ultrasonogram image is not useful for analysis hence these images are pre-processed for the analysis. For example, inside cranial bone, there are necessary tissues and organs. Outside it, there are cranial bones and echo artifacts. The ultrasonogram movie of the coronal sections is symmetrical with the left and right parts but sagittal sections are not symmetrical. Therefore, it is not necessary to analyze the entire portion of the ultrasonogram image. In case of off-line analysis, relatively a smaller part in the ultrasonogram image can be used. In our analysis, different masks for different sections are used. These masks are designed to specify regions of interest (ROI) for the simplification of the analysis.

3.4.1 Hexagonal Mask

In designing hexagonal mask six points are used. Hexagonal mask design procedure is described below. Location of six points is shown in the Figure 3.2.

Using these six points following algorithm produces the desired mask file:

Step 1: Variation of x values from x_{left} to x_{mid} per unit variation of y values from y_{top} to y_{mid} is determined.

Step 2: Two corresponding x values are determined by subtracting and adding the offset value with the x_{mid} for every y values from y_{top} to y_{mid}. The offset values vary in every step and it is equal to the i^{th} multiple of result from step 1, where i indicates the current step and it varies from 0 1 2.....(y_{mid}-y_{top}).

Step 3: Step 2 is repeated for the values of y_{mid} to yend and x_{left}, x_{right} instead of x_{mid}.

Step 4: Step 2 is repeated for the values of y_{end} to y_{bottom} and x_{lend}, x_{rend} instead of x_{mid}.

From the x values at the output file together with information y_{top} and y_{bottom}, we generated the hexagonal mask.

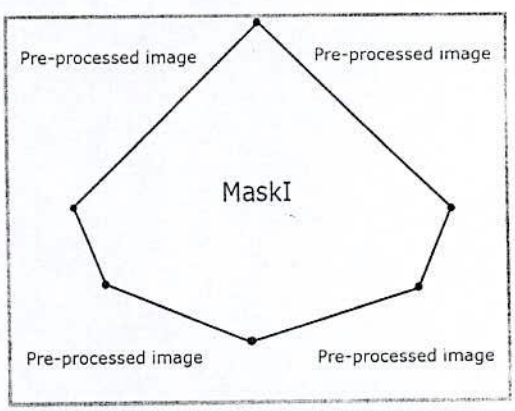

Figure 3.2: ROI selection using 6 point masking procedure.

3.4.2 Parabolic mask

We used four points to design parabolic mask. Parabolic mask design procedure is described below. Location of four points is shown in the Figure 3.3. Using these four points following algorithm produces the desired mask file:

Step 1: Variation of x values from x_{left} to x_{mid} per unit variation of y values from y_{top} to y_{mid} is determined.

Step 2: Two corresponding x values are determined by subtracting and adding the offset values with the x_{mid} for every value from y_{top} to y_{mid}. The offset values vary in every step

and it is equal to the i^{th} multiple of result from step 1, where i indicates the current step and it varies from 0 1 2..... (y_{mid}-y_{top}).

Step 3: Two corresponding x values are determined using x_{left} and x_{right} for every values from y_{mid} to y_{bottom} using parabolic/circle equation for the offset determination.

From the x values at the output file together with information of y_{top} and y_{bottom} we generated the parabolic mask.

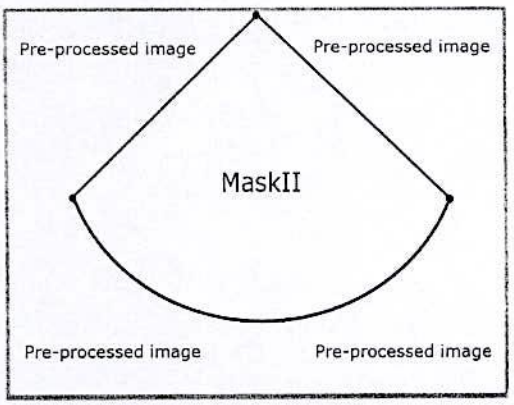

Figure 3.3: ROI selection using 4 point masking procedure.

3.4.3 Format of Mask file

Mask file is a two column ASKII file and the format of mask file is shown below

Column 1	Column 2
y_{top}	y_{bottom}
x_{start}	x_{end} (Start from y_{top})
x_{start}	x_{end}
.....	.....
.....	.....
x_{start}	x_{end} (up to y_{bottom})

An example of mask file is shown in Figure 3.4.

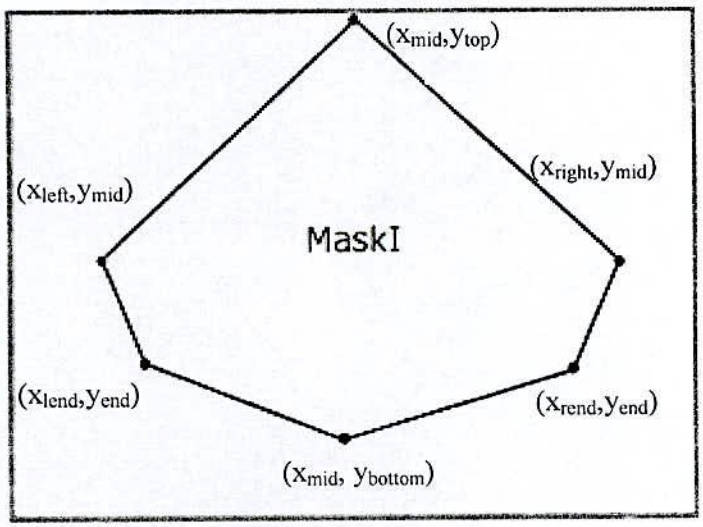

(a)

Column 1	Column 2	Column 1	Column 2
		.....	.....
0 (y_{top})	224 (y_{bottom})	68	291
180	180 (Start from y_{top})	69	291
178	181	70 (x_{lend})	290 (x_{rend})
177	182	86	273
.....	.....	105	254
.....	.....	.....	.....
45	314	.....	.....
44 (x_{left})	315 (x_{right})	179	180 (x_{mid})
45	314		

(b)

Figure 3.4: (a) Graphical demonstration and (b) example of a six point mask file.

3.5 Ultrasonogram image sequences

The original ultrasonographic movies or ultrasonogram image sequences were captured by using an ultrasound probe of 5 MHz at the side of pediatricians. Port Royal method is used for selections scanned through the anterior fontanelle. Then a series of ultrasound images was captured by a PCI-based PC with video digitizer. The specifications of the ultrasonogram image sequences are given in Table 1

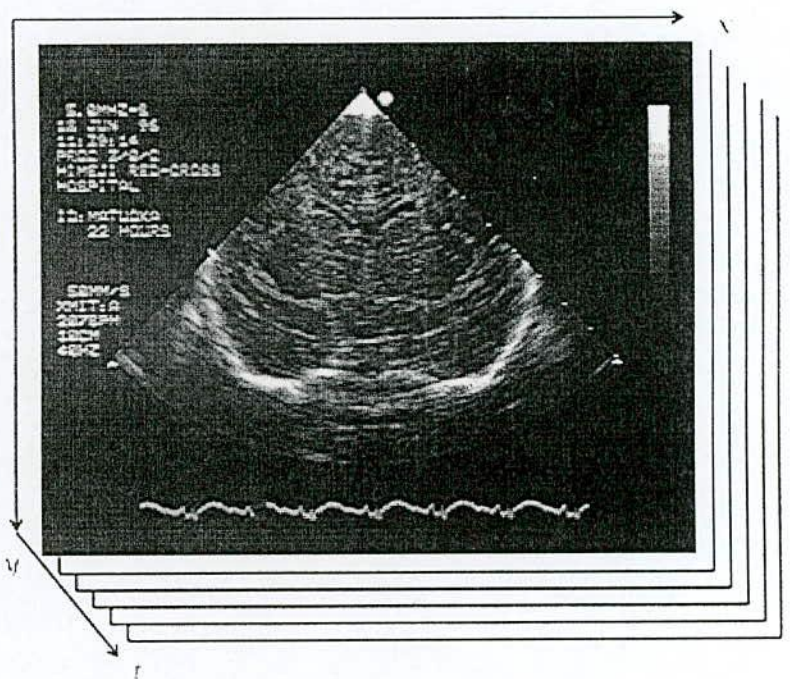

Figure 3.5: Ultrasonogram image sequences

Table 3.1: Specification of ultrasonogram image sequences

Number of frames in each sequences	32 frames
Size of each frame	640×480 pixels
Depth of each pixel	8 bits
Frame Rate	33ms

CHAPTER 4

Analysis of neonatal tissue velocity

4.1 Introduction

4.1.1 Tissue motion and tissue motion velocity

The brain tissues experience motion due to blood flow through the brain. The blood flow is due to heartbeat. The velocity experience by brain tissue is called tissue-motion velocity. The nature of the tissue motion velocity is periodic. The tissue motion velocities repeat themselves due to the periodic nature of the heartbeat. Since the heartbeat is also varied due to physical condition of newborn babies, the tissue motion velocities are varied from time to time, baby to baby.

4.1.2 Pulsation and pulsation strength

Pulsation is the periodic beating of arteries as blood is pumped through arteries. Pulsation strength represents the rating of blood flow through arteries. The tissue motion velocity is associated with blood flow. Therefore, pulsation strength can be considered as the magnitude of tissue motion velocity around the arteries. The motion velocity is periodic in nature. The variation of blood flow is according with heartbeat. So, pulsation has a relation with heartbeat interval. Therefore, pulsation strength is lower or higher depends upon the blood flow rate or flow velocity.

4.2 Direct interpretation of ultrasonogram images

Using direct pixel value of neonatal cranial ultrasonogram brain maturation, the presence of structural brain abnormalities and/or brain injury, the timing of cerebral injury, the neurological prognosis of the infant can be assessed. Seriously in ill neonates and in neonates with serious cerebral abnormalities, either congenital or acquired, it plays a role in decisions on continuation or withdrawal of intensive treatment. In neonates surviving with cerebral injury, it may help to optimize treatment of the infant and support of the infant and his or her family, both during the neonatal period and thereafter. From ultrasonogram movie or ultrasonogram image sequence, the neonatal cranial tissue motion can be observed.

4.3 Relation between tissue-velocity and heartbeat interval

There is a strong correlation of the blood flow in the newborn baby head with the artery pulsation and the tissue-motion has a relationship with artery pulsation. Medical doctors observe the brain tissue of the newborn baby through the soft tissue named anterior fontanel. The velocity experience by brain tissue due to blood flow is known as tissue-motion velocity. The nature of the tissue motion velocity is periodic due to periodic nature of heartbeat and it varies time to time, baby to baby, and it depends on physical conditions of the prematured baby. Therefore, tissue motion contains many harmonic components of the pulsation frequency. The tissue-motion velocities repeat themselves due to the periodic nature of heartbeat. Since the heartbeat also varies due to physical condition of newborn babies, the tissue motion velocities vary from time to time, baby to baby. Artery pulsation is the periodic beating of arteries as blood pumps through arteries, and pulsation strength represents the rating of blood flow to the brain-tissue through essential arteries in the brain. The tissue motion velocity is associated with blood flow. Therefore, pulsation strength can be considered as the magnitude of tissue motion velocity, and therefore, a relationship exists between motion and heartbeat interval. Therefore, pulsation strength is lower or higher depends upon the blood flow rate or flow velocity.

4.4 Motion analysis using optical flow velocity

4.4.1 Why optical flow?

Optical flow or optic flow is the pattern of apparent motion of objects, surfaces, and edges in a visual scene caused by the relative motion between an observer (an eye or a camera) and the scene. Optical flow techniques are used in motion detection, object segmentation, time-to-collision and focus of expansion calculations, motion compensated encoding, and stereo disparity measurement utilize this motion of the objects surfaces, and edges.

The term of optical flow is used to denote the temporal shift of observable gray value structure in image sequences [16]. The velocity field that represents the motion of the object points across an image is called the optical flow field. Optical flow can be used to determine the object motion in an image sequence. Two main approaches are available for real time motion field estimation. They are matching based (correspondence) and gradient based approaches. Gradient based approaches utilize a relationship between the motion of the surfaces and the derivative of image brightness [8~11] and [17~24]. Matching techniques [25] locate and track small, identifiable regions of the image over time.

Gradient-based approaches have several advantages over matching-based approaches. Matching techniques are highly sensitive to ambiguity among the structures to be matched. Since it is computationally impractical to estimate matches for a large number of points, so gradient based approach allows optical flow to be simply computed at a more dense sampling points than can be obtained with matching methods.

4.4.2 Gradient constraint equation

Gradient-based approaches provide a solution to motion estimation from the observation in time of changes in the image brightness. These changes are modeled by means of partial differential equations, which are called constraint equations. The field of velocity vector obtained by solving such partial differential equations is normally called as optical flow or image flow. Optical flow is based on the observation of the changes in the image brightness. The most important partial differential equation for modeling optical flow fields is obtained by considering the change of image brightness as stationary with respect to time, 't'. Let $p(x, y, t)$ be the image brightness in an image sequence at location (x, y) of the image at time t. Let $v_x(x, y) = \frac{dx}{dt}$ and $v_y(x, y) = \frac{dy}{dt}$ be the optical flow velocity components in horizontal and vertical directions. Then following Horn and Schunck [8~10], the brightness value at time t at point $(x, y)$and at time $t + \delta t$ at point $(x + \delta x, y + \delta y)$, *where* $\delta x = v_x \delta t$ and $\delta y = v_y \delta t$; will be the same:

$$p\big(x + v_x\delta t, y + v_y\delta t, t + \delta t\big) = p(x, y, t) \tag{4.4.1}$$

If we expand left hand side by Taylor series expansion,

$$p(x, y, t) + \frac{\partial p}{\partial x} v_x \delta t + \frac{\partial p}{\partial y} v_y \delta t + \frac{\partial p}{\partial t} \delta t + \epsilon = p(x, y, t) \tag{4.4.2}$$

where ϵ contains second and higher order terms in $v_x\delta t$, $v_y\delta t$ and δt. After subtracting $p(x, y, t)$ from both sides and dividing by δt, the result is

$$\frac{\partial p}{\partial x} v_x \frac{\delta t}{\delta t} + \frac{\partial p}{\partial y} v_y \frac{\delta t}{\delta t} + \frac{\partial p}{\partial t} \frac{\delta t}{\delta t} + \epsilon = \mathcal{O}(\delta t) \tag{4.4.3}$$

where $\mathcal{O}$ is a term of order δt that includes the first and higher variation of x *and* y since we assume that $v_x\delta t$ and $v_y\delta t$ will depend on δt. The second and higher order terms can be neglected. If the velocity is assumed locally stationary $[\frac{\partial v_x}{\partial x} = \frac{\partial v_x}{\partial y} = \frac{\partial v_y}{\partial x} = \frac{\partial v_y}{\partial y} = 0]$ to the limit $\delta t \to 0$, the equation (4.4.3) becomes

$$\frac{\partial p}{\partial x}v_x + \frac{\partial p}{\partial y}v_y + \frac{\partial p}{\partial t} = 0 \tag{4.4.4}$$

Eq. (4.4.4) is the constraint equation of optical flow which relates the temporal gradient, $\frac{\partial p}{\partial t}$ and spatial gradients, $\frac{\partial p}{\partial x}$ *and* $\frac{\partial p}{\partial y}$ at a point (x, y) in the image plane to the instantaneous velocity (v_x, v_y) at that point in the image. The gradient constraint equation can be represented by graphical representation in the (v_x, v_y) plane in Figure 4.1.

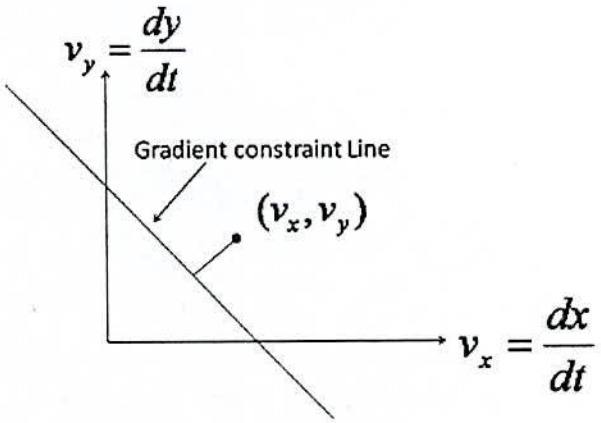

Figure 4.1: Gradient constraint line in the v_x *and* v_y plane. D is normalized distance from any pixel point to gradient constraint line

4.4.3 Local optimization

The method of local optimization estimates optical flow by solving a group of gradient constraints obtained from a small region of the image as a system of linear equations. Least-square solution of the gradient constraint equation is used in local optimization technique [9] without going into the different task of assigning any smoothen constraint operator. Suppose there are N points in a local region S. For considering a unique velocity in the local region, the following system of equations can be obtained.

$$\begin{aligned}
&\frac{\partial p^{(1)}}{\partial x} v_x + \frac{\partial p^{(1)}}{\partial y} v_y + \frac{\partial p^{(1)}}{\partial t} = 0 \\
&\frac{\partial p^{(2)}}{\partial x} v_x + \frac{\partial p^{(2)}}{\partial y} v_y + \frac{\partial p^{(2)}}{\partial t} = 0 \\
&\frac{\partial p^{(3)}}{\partial x} v_x + \frac{\partial p^{(3)}}{\partial y} v_y + \frac{\partial p^{(3)}}{\partial t} = 0 \\
&\qquad\qquad\vdots \\
&\frac{\partial p^{(N)}}{\partial x} v_x + \frac{\partial p^{(N)}}{\partial y} v_y + \frac{\partial p^{(N)}}{\partial t} = 0
\end{aligned} \tag{4.4.5}$$

The above system of equations can be arranged as a matrix of equations which is an over determined form.

$$\begin{bmatrix} \frac{\partial p^{(1)}}{\partial x} & \frac{\partial p^{(1)}}{\partial y} \\ \frac{\partial p^{(2)}}{\partial x} & \frac{\partial p^{(2)}}{\partial y} \\ \frac{\partial p^{(3)}}{\partial x} & \frac{\partial p^{(3)}}{\partial y} \\ \vdots & \vdots \\ \frac{\partial p^{(N)}}{\partial x} & \frac{\partial p^{(N)}}{\partial y} \end{bmatrix} \begin{bmatrix} v_x \\ v_y \end{bmatrix} = - \begin{bmatrix} \frac{\partial p^{(1)}}{\partial t} \\ \frac{\partial p^{(2)}}{\partial t} \\ \frac{\partial p^{(3)}}{\partial t} \\ \vdots \\ \frac{\partial p^{(N)}}{\partial t} \end{bmatrix} \tag{4.4.6}$$

Let us define,

$$G = \begin{bmatrix} \frac{\partial p^{(1)}}{\partial x} & \frac{\partial p^{(1)}}{\partial y} \\ \frac{\partial p^{(2)}}{\partial x} & \frac{\partial p^{(2)}}{\partial y} \\ \frac{\partial p^{(3)}}{\partial x} & \frac{\partial p^{(3)}}{\partial y} \\ \vdots & \vdots \\ \frac{\partial p^{(N)}}{\partial x} & \frac{\partial p^{(N)}}{\partial y} \end{bmatrix}, \vec{v} = \begin{bmatrix} v_x \\ v_y \end{bmatrix}, I_t = \begin{bmatrix} \frac{\partial p^{(1)}}{\partial t} \\ \frac{\partial p^{(2)}}{\partial t} \\ \frac{\partial p^{(3)}}{\partial t} \\ \vdots \\ \frac{\partial p^{(N)}}{\partial t} \end{bmatrix}$$

If an overdetermined system of equations is used to estimate optical flow, the measurement error in the gradients and in compatibilities among the constraint equations due to differential motion will be reflected in the residual of the solution. The residual vector, r can be estimated by [11]:

$$r \equiv G\vec{v} + I_t \tag{4.4.7}$$

In general, the over determined system has no exact solution. An approximate solution was found by minimizing the residual vector r defined by eq. (4.4.7).

$$r \equiv \frac{\partial p}{\partial x} v_x + \frac{\partial p}{\partial y} v_y + \frac{\partial p}{\partial t} \tag{4.4.8}$$

Now the equation is solved by least square technique. Therefore, summation of error, S is,

$$S = \sum\sum r^2 = \sum\sum \left(\frac{\partial p}{\partial x} v_x + \frac{\partial p}{\partial y} v_y + \frac{\partial p}{\partial t} \right)^2 \tag{4.4.9}$$

Now, $\frac{ds}{dv_x} = 0, \frac{ds}{dv_y} = 0$ gives

$$\frac{ds}{dv_x} = \Sigma\Sigma 2.\left(\frac{\partial p}{\partial x}v_x + \frac{\partial p}{\partial y}v_y + \frac{\partial p}{\partial t}\right)\frac{\partial p}{\partial x} = 0$$

$$\frac{ds}{dv_y} = \Sigma\Sigma 2.\left(\frac{\partial p}{\partial x}v_x + \frac{\partial p}{\partial y}v_y + \frac{\partial p}{\partial t}\right)\frac{\partial p}{\partial y} = 0$$

Which gives,

$$\Sigma\Sigma\left(\frac{\partial p}{\partial x}\frac{\partial p}{\partial x}v_x + \frac{\partial p}{\partial x}\frac{\partial p}{\partial y}v_y + \frac{\partial p}{\partial t}\frac{\partial p}{\partial x}\right) = 0$$

$$\Sigma\Sigma\left(\frac{\partial p}{\partial x}\frac{\partial p}{\partial y}v_x + \frac{\partial p}{\partial y}\frac{\partial p}{\partial y}v_y + \frac{\partial p}{\partial t}\frac{\partial p}{\partial y}\right) = 0$$

The above equation can be arranged as a matrix

$$\begin{bmatrix}\Sigma\Sigma\left(\frac{\partial p}{\partial x}\frac{\partial p}{\partial x}\right) & \Sigma\Sigma\left(\frac{\partial p}{\partial x}\frac{\partial p}{\partial y}\right)\\ \Sigma\Sigma\left(\frac{\partial p}{\partial x}\frac{\partial p}{\partial y}\right) & \Sigma\Sigma\left(\frac{\partial p}{\partial y}\frac{\partial p}{\partial y}\right)\end{bmatrix}\begin{bmatrix}v_x\\ v_y\end{bmatrix} = -\begin{bmatrix}\Sigma\Sigma\left(\frac{\partial p}{\partial t}\frac{\partial p}{\partial x}\right)\\ \Sigma\Sigma\left(\frac{\partial p}{\partial t}\frac{\partial p}{\partial y}\right)\end{bmatrix} \quad (4.4.10)$$

The approximated value of $v_{x(i,j,k)}$ *and* $v_{y(i,j,k)}$ at any pixel location in the local region can be determined by the following summations [Appendix I.]

$$v_{x(i,j,k)} = \frac{\Sigma_i\Sigma_j\left(\frac{\partial p}{\partial x}\right)\left(\frac{\partial p}{\partial y}\right)\Sigma_k\Sigma_j\left(\frac{\partial p}{\partial t}\right)\left(\frac{\partial p}{\partial y}\right) - \Sigma_j\Sigma_j\left(\frac{\partial p}{\partial y}\right)^2\Sigma_k\Sigma_j\left(\frac{\partial p}{\partial t}\right)\left(\frac{\partial p}{\partial x}\right)}{\Sigma_i\Sigma_i\left(\frac{\partial p}{\partial x}\right)^2\Sigma_j\Sigma_j\left(\frac{\partial p}{\partial y}\right)^2 - (\Sigma_i\Sigma_j\left(\frac{\partial p}{\partial x}\right)\left(\frac{\partial p}{\partial y}\right))^2} \quad (4.4.11)$$

$$v_{y(i,j,k)} = \frac{\Sigma_i\Sigma_j\left(\frac{\partial p}{\partial x}\right)\left(\frac{\partial p}{\partial y}\right)\Sigma_k\Sigma_j\left(\frac{\partial p}{\partial t}\right)\left(\frac{\partial p}{\partial x}\right) - \Sigma_j\Sigma_j\left(\frac{\partial p}{\partial x}\right)^2\Sigma_k\Sigma_j\left(\frac{\partial p}{\partial t}\right)\left(\frac{\partial p}{\partial x}\right)}{\Sigma_i\Sigma_i\left(\frac{\partial p}{\partial x}\right)^2\Sigma_j\Sigma_j\left(\frac{\partial p}{\partial y}\right)^2 - (\Sigma_i\Sigma_j\left(\frac{\partial p}{\partial x}\right)\left(\frac{\partial p}{\partial y}\right))^2} \quad (4.4.12)$$

The absolute value of flow velocity is given by

$$|V|_{(i,j,k)} = \sqrt{v_{x(i,j,k)}{}^2 + v_{y(i,j,k)}{}^2} \quad (4.4.13)$$

The normalized error at any pixel is defined as the normalized distance from the pixel point to the gradient constraint line in the local region.

$$d_{(i,j,k)} = \frac{\left|\frac{\partial p}{\partial x}_{(i,j,k)}v_x + \frac{\partial p}{\partial y}_{(i,j,k)}v_y + \frac{\partial p}{\partial t}_{(i,j,k)}\right|}{\sqrt{\frac{\partial p^2}{\partial x}_{(i,j,k)} + \frac{\partial p^2}{\partial y}_{(i,j,k)}}} \quad (4.4.14)$$

If constraint line completely satisfied over the local region, then d become zero. If the error has some value, then gradient constraint line is not completely satisfied over local region.

4.4.4 Global Optimization

In global optimization technique [8], [10], [16], [19], [26] the velocity field is determined by minimizing an error function based on the gradient constraint and a global smoothing term over the entire image.

According to above definition, the error function $p(\alpha)$ consists of two terms, p_0 and p_s, where

- The first term $p_0(x,y,t) = (\frac{\partial p}{\partial x}v_x + \frac{\partial p}{\partial y}v_y + \frac{\partial p}{\partial t})^2$ is the square of the error from the optical flow constraint, and
- the term $p_s(x,y,t) = (\frac{\partial v_x}{\partial x})^2 + (\frac{\partial v_x}{\partial y})^2 + (\frac{\partial v_y}{\partial x})^2 + (\frac{\partial v_y}{\partial y})^2$ is a penalty that encourages smoothness:

Now,

$$p(\alpha) = \iint p_0(x,y,t) + \alpha^2 p_s(x,y,t)dxdy \tag{4.4.15}$$

α is a weighting factor that controls the influence of the smoothness constraint. The error function is minimized by using the calculus of variations, which leads to a system of two coupled differential equations from the Euler-Lagrange equations.

$$\nabla^2 v_x = \frac{\frac{\partial p}{\partial x}}{\alpha^2}\left(\frac{\partial p}{\partial x}v_x + \frac{\partial p}{\partial y}v_y + \frac{\partial p}{\partial t}\right) \tag{4.4.16}$$

$$\nabla^2 v_y = \frac{\frac{\partial p}{\partial y}}{\alpha^2}\left(\frac{\partial p}{\partial x}v_x + \frac{\partial p}{\partial y}v_y + \frac{\partial p}{\partial t}\right) \tag{4.4.17}$$

Where ∇^2 is the Laplacian operator, $\nabla^2 = \frac{\partial^2}{\partial x^2} + \frac{\partial^2}{\partial y^2}$

The Laplacians of v_x, v_y are approximated by

$$\nabla^2 v_x \approx \bar{v}_{x(i,j,k)} - v_{x(i,j,k)} \tag{4.4.18}$$

$$\nabla^2 v_y \approx \bar{v}_{y(i,j,k)} - v_{y(i,j,k)} \tag{4.4.19}$$

Where $\bar{v}_{x(i,j,k)}$ and $\bar{v}_{y(i,j,k)}$ denote the Gaussian weighted averages of the neighbor points around the point at pixel position (i,j,k)Therefore,

$$\bar{v}_x - v_x = \frac{\frac{\partial p}{\partial x}}{\alpha^2}\left(\frac{\partial p}{\partial x}v_x + \frac{\partial p}{\partial y}v_y + \frac{\partial p}{\partial t}\right)$$

$$\alpha^2(\bar{v}_x - v_x) = \frac{\partial p}{\partial x}\left(\frac{\partial p}{\partial x}v_x + \frac{\partial p}{\partial y}v_y + \frac{\partial p}{\partial t}\right)$$

$$\left(\left(\frac{\partial p}{\partial x}\right)^2 + \alpha^2\right)v_x + \frac{\partial p}{\partial x}\frac{\partial p}{\partial y}v_y = \alpha^2\bar{v}_x - \frac{\partial p}{\partial x}\frac{\partial p}{\partial t} \qquad (4.4.20)$$

$$\bar{v}_y - v_y = \frac{\frac{\partial p}{\partial y}}{\alpha^2}\left(\frac{\partial p}{\partial x}v_x + \frac{\partial p}{\partial y}v_y + \frac{\partial p}{\partial t}\right)$$

$$\alpha^2(\bar{v}_y - v_y) = \frac{\partial p}{\partial y}\left(\frac{\partial p}{\partial x}v_x + \frac{\partial p}{\partial y}v_y + \frac{\partial p}{\partial t}\right)$$

$$\frac{\partial p}{\partial x}\frac{\partial p}{\partial y}v_x + \left(\alpha^2 + \left(\frac{\partial p}{\partial y}\right)^2\right)v_y = \alpha^2\bar{v}_y - \frac{\partial p}{\partial y}\frac{\partial p}{\partial t} \qquad (4.4.21)$$

Eqs. (4.4.20) and (4.4.21) can be arranged as a matrix-

$$\begin{bmatrix} \left(\frac{\partial p}{\partial x}\right)^2 + \alpha^2 & \frac{\partial p}{\partial x}\frac{\partial p}{\partial y} \\ \frac{\partial p}{\partial x}\frac{\partial p}{\partial y} & \alpha^2 + \left(\frac{\partial p}{\partial y}\right)^2 \end{bmatrix}\begin{bmatrix} v_x \\ v_y \end{bmatrix} = -\begin{bmatrix} \alpha^2\bar{v}_x - \frac{\partial p}{\partial x}\frac{\partial p}{\partial t} \\ \alpha^2\bar{v}_y - \frac{\partial p}{\partial y}\frac{\partial p}{\partial t} \end{bmatrix} \qquad (4.4.22)$$

The value of v_x and v_y [appendix II.] is given below

$$v_x = \bar{v}_x - \frac{\frac{\partial p}{\partial x}\left(\frac{\partial p}{\partial x}v_x + \frac{\partial p}{\partial y}v_y + \frac{\partial p}{\partial t}\right)}{\alpha^2 + \frac{\partial^2 p}{\partial x^2} + \frac{\partial^2 p}{\partial y^2}} \qquad (4.4.23)$$

$$v_y = \bar{v}_y - \frac{\frac{\partial p}{\partial y}\left(\frac{\partial p}{\partial x}v_x + \frac{\partial p}{\partial y}v_y + \frac{\partial p}{\partial t}\right)}{\alpha^2 + \frac{\partial^2 p}{\partial x^2} + \frac{\partial^2 p}{\partial y^2}} \qquad (4.4.24)$$

If the velocity estimations are $({v_x}^{n+1}, {v_y}^{n+1})$ and the average of previous velocity estimations are $({v_x}^{n}, {v_y}^{n})$ where n is iteration number, then the estimated velocity at any pixel position (i, j, k) is given by

$$v_x{}^{n+1} = \bar{v}_x{}^{-n} - \frac{\frac{\partial p}{\partial x}\left(v_x{}^{-n}\frac{\partial p}{\partial x} + v_y{}^{-n}\frac{\partial p}{\partial y} + \frac{\partial p}{\partial t}\right)}{\alpha^2 + \frac{\partial^2 p}{\partial x^2} + \frac{\partial^2 p}{\partial y^2}} \tag{4.4.25}$$

$$v_y{}^{n+1} = \bar{v}_y{}^{-n} - \frac{\frac{\partial p}{\partial y}\left(v_x{}^{-n}\frac{\partial p}{\partial x} + v_y{}^{-n}\frac{\partial p}{\partial y} + \frac{\partial p}{\partial t}\right)}{\alpha^2 + \frac{\partial^2 p}{\partial x^2} + \frac{\partial^2 p}{\partial y^2}} \tag{4.4.26}$$

The local average is defined as follows [7]:

$$\begin{aligned} v_{x(i,j,k)}^{-n} &= \left[v_{xi-1,j-1,k} + v_{xi-1,j+1,k} + v_{xi+1,j-1,k} + v_{xi+1,j+1,k}\right] \times \frac{1}{12} \\ &+ \left[v_{xi-1,j,k} + v_{xi+1,j,k} + v_{xi,j-1,k} + v_{xi,j+1,k}\right] \times \frac{1}{6} \end{aligned} \tag{4.4.27}$$

$$\begin{aligned} v_{y(i,j,k)}^{-n} &= \left[v_{yi-1,j-1,k} + v_{yi-1,j+1,k} + v_{yi+1,j-1,k} + v_{yi+1,j+1,k}\right] \times \frac{1}{12} \\ &+ \left[v_{yi-1,j,k} + v_{yi+1,j,k} + v_{yi,j-1,k} + v_{yi,j+1,k}\right] \times \frac{1}{6} \end{aligned} \tag{4.4.28}$$

4.4.5 Combined Local and Global (CLG) optimization

As discussed before, to solve the problem of sensitivity to noise, Bruhn et al. [27] proposed a method to combine local [28] with global [8]. To give a combined local-global method, let us reformulate the previous formulae:

The spatio-temporal CLG motion can be expressed as $w = [v_x, v_y, 1]^t$ at a pixel $x = (x, y)$ in time t. The velocity gradient is $\nabla w = |\nabla v_x|^2 + |\nabla v_y|^2$ and the intensity gradient is $\nabla_{3p} = (p_x, p_y, p_t)^T$. We also define the motion tensor:$\nabla_p(\nabla_{3p}) = K_p(\nabla_{3p}\nabla_{3p}{}^T)$. K_p is the smoothing kernel (spatial or spatial-temporal). It is evident that Lucas-Kanade minimizes the quadratic form of the energy function, E_{LK} and we get(4.4.29).

$$\begin{aligned} E_{LK} &= K_p(p_x v_x + p_y v + p_t)^2 \\ &= w^T.\begin{pmatrix} (P_x)^2 & P_x P_y & P_x P_t \\ P_x P_y & (P_y)^2 & P_y P_t \\ P_x P_t & P_y P_t & (P_t)^2 \end{pmatrix}.w \\ &= w^T J_p(\nabla_{3p}).w \end{aligned} \tag{4.4.29}$$

where p_x, p_y, p_t denote the image intensity gradient with respect to Cartesian and temporal dimensions. We have a similar formulation for Horn and Schunck with an iterative recursion in (4.4.30).

$$E_{HS}(w) = \int_{\Omega} (w^T J_0(\nabla_{3p}).w + \alpha|\nabla w|^2 dydx) \quad (4.4.30)$$

where, E_{HS} is the energy function of HS (Horn-Schunck), J is the motion tensor and w is the motion vector [14, 29]. Then we can rewrite:

$$\nabla_{3p} = (p_x, p_y, p_t)^T = J_p(\nabla_{3p}) = K_p * (\nabla_{3p}.\nabla_{3p}{}^T) \quad (4.4.31)$$

By replacing the structure tensor $J_0(\nabla_{3p})$ instead of matrix$J_p(\nabla_{3p})$, we will have:

$$\Delta v_x - \frac{1}{\alpha}(p_x{}^2 v_x + p_x p_y v_y + p_t p_x) = 0 \quad (4.4.32)$$

$$\Delta v_y - \frac{1}{\alpha}(p_x p_y v_x + p_x{}^2 v_y + p_t p_y) = 0 \quad (4.4.33)$$

Its minimization induces to (4.4.34) and (4.4.35) which satisfies Euler-Lagrange formula:

$$\Delta v_x - \frac{1}{\alpha}(K_p p_x{}^2 v_x + K_p p_x p_y v_y + K_p p_t p_x) = 0 \quad (4.4.34)$$

$$\Delta v_y - \frac{1}{\alpha}(K_p p_x p_y v_x + K_p p_y{}^2 v_y + K_p p_y p_t) = 0 \quad (4.4.35)$$

Now, the spatiotemporal combined local-global approach is defined in (4.4.36).

$$E_{CLG}(w) = \int_{\Omega} (w^T J_p(\nabla_{3p}).w + \alpha|\nabla w|^2 dxdy) \quad (4.4.36)$$

Combining the temporal extended variant of both [8] and [28] method, we obtain a spatio-temporal version of the combined local-global functional which is given in(4.4.37).

$$E_{CLG}(w) = \int_{\text{video}} (w^T J_p(\nabla_{3p}).w + \alpha|\nabla w|^2 dxdydt) \quad (4.4.37)$$

Therefore, based on Lagrange equations, we have:

$$0 = \sum_{j\epsilon N(i)} \frac{v_{x_j} - v_{x_i}}{h^2} - \frac{1}{\alpha}\left(J_{11i} v_{x_i} + J_{12i} v_{y_i} + J_{13i}\right) \quad (4.4.38)$$

$$0 = \sum_{j\epsilon N(i)} \frac{v_j - v_i}{h^2} - \frac{1}{\alpha}\left(J_{21i} v_{x_i} + J_{22i} v_{y_i} + J_{23i}\right) \quad (4.4.39)$$

for $i = 1,2,\ldots..,N$ and $N(i)$ denotes the set of neighborhood of pixel i. After some manipulation, the iterative formulations of (4.4.40) and (4.4.41) are found.

$$v_{x_i}^{k+1} = (1-\omega)v_{x_i}^{k} + \omega \frac{\sum_{j\epsilon N-(i)} v_{x_j}^{k+1} + \sum_{j\epsilon N+(i)} v_{x_j}^{k} - \frac{h^2}{\alpha}(J_{12i}v_{y_i}^{k} + J_{13i})}{|N(i)| + \frac{h^2}{\alpha}J_{11i}} \quad (4.4.40)$$

$$v_{y_i}^{k+1} = (1-\omega)v_{y_i}^{k} + \omega \frac{\sum_{j\epsilon N-(i)} v_{y_j}^{k+1} + \sum_{j\epsilon N+(i)} v_{y_j}^{k} - \frac{h^2}{\alpha}(J_{21i}v_{y_i}^{k} + J_{23i})}{|N(i)| + \frac{h^2}{\alpha}J_{22i}} \quad (4.4.41)$$

Where

$$N^{-}(i) = j\epsilon N(i)\,|j < i,$$
$$N^{+}(i) = j\epsilon N(i)\,|j > i,$$

and $|N(i)|$ are the numbers of neighborhood pixel region for implementing Gauss-Seidel iteration. Here, i *and* j indices determine the backward and forward Gauss-Seidel iterative pixels and k defines the iteration number. From motion components, the values of the magnitude of tissue motion and the phase angle may be determined by

$$V(x,y,t) = \sqrt{v_x^2 + v_y^2}$$
$$\emptyset = arctan(v_y/v_x)$$

4.4.6 Estimation of gradients

The gradient constraint equation contains the horizontal and vertical spatial gradients, $\frac{\partial p}{\partial x}$ *and* $\frac{\partial p}{\partial y}$ temporal gradient, $\frac{\partial p}{\partial t}$ and the optical flow velocity components(v_x, v_y). How these gradients are calculated from three consecutive image frames which can make a large difference in the result. It is important that the estimation of $\frac{\partial p}{\partial x}, \frac{\partial p}{\partial y}$ *and* $\frac{\partial p}{\partial t}$ should be consistent. Many formulas can be used for such estimations. Figure 4.2 shows the $3 \times 3 \times 3$ for estimating gradients from an ultrasonographic movie. If $f, g,$ *and* h denote the variables i, j *and* k then

First method: In this method, the spatial and temporal gradients were estimated by using forward or central differences.

Using first method, the gradients are;

$$\frac{\partial p}{\partial x}_{(i,j,k)} \approx \frac{1}{2}[p(i+\Delta i, j, k) - p(i-\Delta i, j, k)]$$
$$\frac{\partial p}{\partial y}_{(i,j,k)} \approx \frac{1}{2}[p(i, j+\Delta j, k) - p(i, j-\Delta j, k)] \quad (4.4.42)$$
$$\frac{\partial p}{\partial t}_{(i,j,k)} \approx \frac{1}{2}[p(i, j, k+\Delta k) - p(i, j, k-\Delta k)]$$

Second method: In this method, the gradients are estimated from forward and central differences of three consecutive frames and making averages of them.

$$\frac{\partial p}{\partial x}_{(i,j,k)} \approx \frac{1}{18} \sum_{h=k-\Delta k,k,k+\Delta k} \sum_{g=j-\Delta j,j,j+\Delta j} [p(i+\Delta i,g,h) - p(i-\Delta i,g,h)]$$

$$\frac{\partial p}{\partial y}_{(i,j,k)} \approx \frac{1}{18} \sum_{h=k-\Delta k,k,k+\Delta k} \sum_{f=i-\Delta i,i,i+\Delta i} [p(f,j+\Delta j,h) - p(f,j-\Delta j,h)] \quad (4.4.43)$$

$$\frac{\partial p}{\partial t}_{(i,j,k)} \approx \frac{1}{18} \sum_{g=j-\Delta j,j,j+\Delta j} \sum_{f=i-\Delta i,i,i+\Delta i} [p(f,g,k+\Delta k) - p(f,g,k-\Delta k)]$$

Third method: In this method, all points in the middle frame of three consecutive frames are considered and the gradients are estimated by forward or central differences and making averages of them.

$$\frac{\partial p}{\partial x}_{(i,j,k)} \approx \frac{1}{6} \sum_{g=j-\Delta j,j,j+\Delta j} [p(i+\Delta i,g,k) - p(i-\Delta i,g,k)]$$

$$\frac{\partial p}{\partial y}_{(i,j,k)} \approx \frac{1}{6} \sum_{f=i-\Delta i,i,i+\Delta i} [p(f,j+\Delta j,k) - p(f,j-\Delta j,k)] \quad (4.4.44)$$

$$\frac{\partial p}{\partial t}_{(i,j,k)} \approx \frac{1}{10} \sum_{\substack{f=i-\Delta i,i,i+\Delta i \\ g=j,j-\Delta j,j,j+\Delta j,j}} [p(f,g,k+\Delta k) - p(f,g,k-\Delta k)]$$

In the tissue-motion velocity analysis, first method is used for estimating gradients.

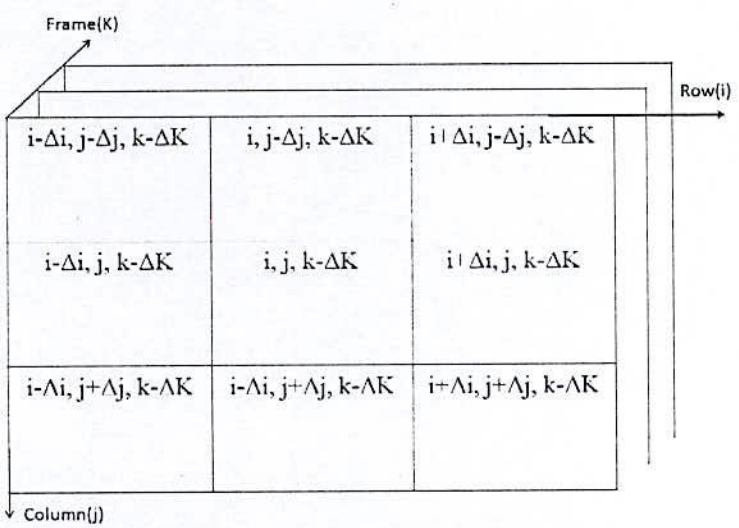

Figure 4.2: A 3×3×3 window for estimating gradients. Row index i corresponds to horizontal direction, Column index corresponds to vertical direction, and frame index k corresponds to time variation of the ultrasonographic movie.

4.4.7 Error Analysis

In order to estimate the degree to which the optical flow constraint equation is satisfied at each pixel, we normalized the residual (or error) by the spatial gradient of image brightness at each pixel, because the magnitude of residual depends on the spatial gradient of brightness. The normalized residual or error at any pixel is defined as the normalized distance from the pixel point to the gradient constraint line in a small region. We define the

region by 3 × 3 × 3 pixels. Equation (4.4.45) represents the error, e at any pixel.

$$e = d(i,j,k) = \frac{|p_x u + p_y v + p_t|}{\sqrt{(p_x)^2 + (p_y)^2}} \tag{4.4.45}$$

where, $d(I,j,k)$ is the normalized distance. The values of p_x, p_y *and* p_t can be estimated by (4.4.46) , (4.4.46) and (4.4.46) respectively.

$$p_x(i,j,k) = \frac{P(i+1,j,k) - P(i-1,j,k)}{2} \tag{4.4.46}$$

$$p_y(i,j,k) = \frac{P(i,j+1,k) - P(i,j-1,k)}{2} \tag{4.4.47}$$

$$p_t(i,j,k) = \frac{P(i,j,k+1) - P(i,j,k-1)}{2} \tag{4.4.48}$$

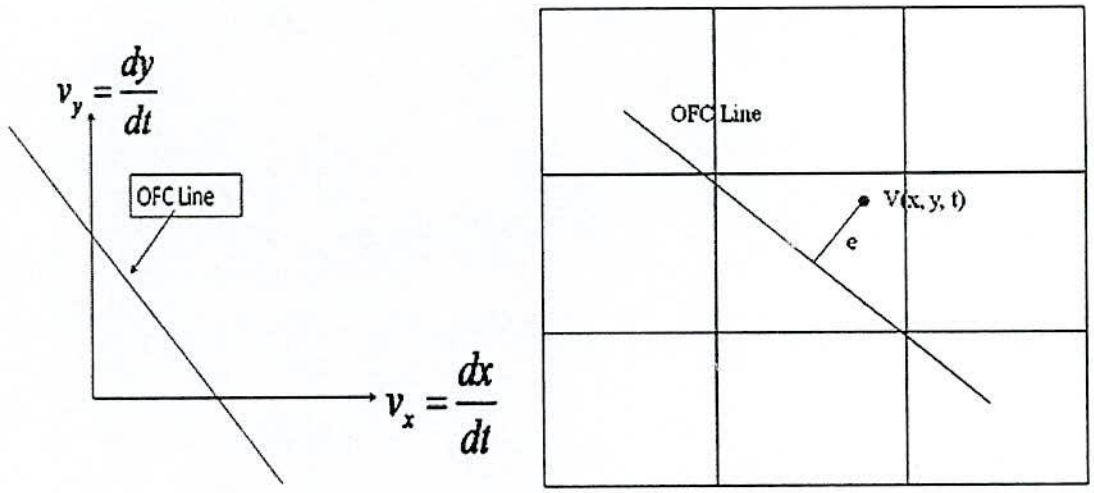

(a) (b)

Figure 4.3: Error calculation in our method. (a) The OFC line in the v_x-v_y plane. (b) The distance (normalized error or residual error) between OFC line and velocity is shown in the image plane.

Equation (4.4.45) gives the minimum distance between the approximated V and OFC line shown in Figure 4.3. If OFC line completely satisfied over a local region, e becomes zero. From the gradient values, it is seen that $\sqrt{(p_x)^2 + (p_y)^2}$ may become zero. In this case e becomes infinity. If the errors have some value, then gradient constraint line is not completely satisfied over defined small region. We use average value of e calculated at each pixel over the small region as an index of the degree to which the OFC equations are satisfied.

4.4.8 Estimation of Tissue-motion Velocity with different brightness condition

Ultrasonographic movie or image sequences are used for estimating tissue-motion velocity from neonatal cranial ultrasonogram. The original ultrasonographic movie was taken by using an ultrasound probe of 5MHz at the side of pediatricians. Port Royal method [3] is used for sections scan through the anterior fontanel of the neonate. Then a series of ultrasound echo images (32 frames, 640×480 pixels/frame, 8 bits/pixel, 33 ms/frame) was captured by a PCI-based PC with video digitizer. The tissue-motion velocity is calculated at each pixel by using a local region of window around the calculated pixel in consecutive three frames of ultrasound echo images.

Figure 4.4 shows the first frame of a series of ultrasonographic echo images with different brightness in the anterior coronal section of a neonatal cranium with tissue-motion velocity images. The pixel value at any position of the image is assumed to be in Figure 4.4(a). Similarly, Figures 4.4(c), 4.4(e) and 4.4(g) show the same images but corresponding brightness respectively. The brightness value of Figure 4.4(b) represents the first frame of optical flow velocity as well as tissue-motion velocity image corresponds to Figure 4.4(a). This image can be represented as the pulsation image since artery pulsation can be represented by the magnitude of tissue motion velocity. Figures 4.4(d), 4.4(f) and 4.4(h) represent the first frame of velocity as well as tissue-motion velocity image corresponds to Figure 4.4(c), 4.4(e) and 4.4(g). The tissue-motion velocity for each position in these images remains same.

For all cases in Figure 4.4, the first frame of ultrasonographic movie is shown and corresponding tissue-motion velocity images are shown. It is observed that the brightness is varied in ultrasound echo images but the brightness of tissue-motion velocity is same. Therefore, if echo images are taken under the condition of low brightness in the same section as Figure 4.4(a) and their tissue-motion velocity are calculated by gradient-based

method of optical flow technique, then it can be confirmed that tissue-motion velocity is not affected by the spatial variation of brightness of echo image.

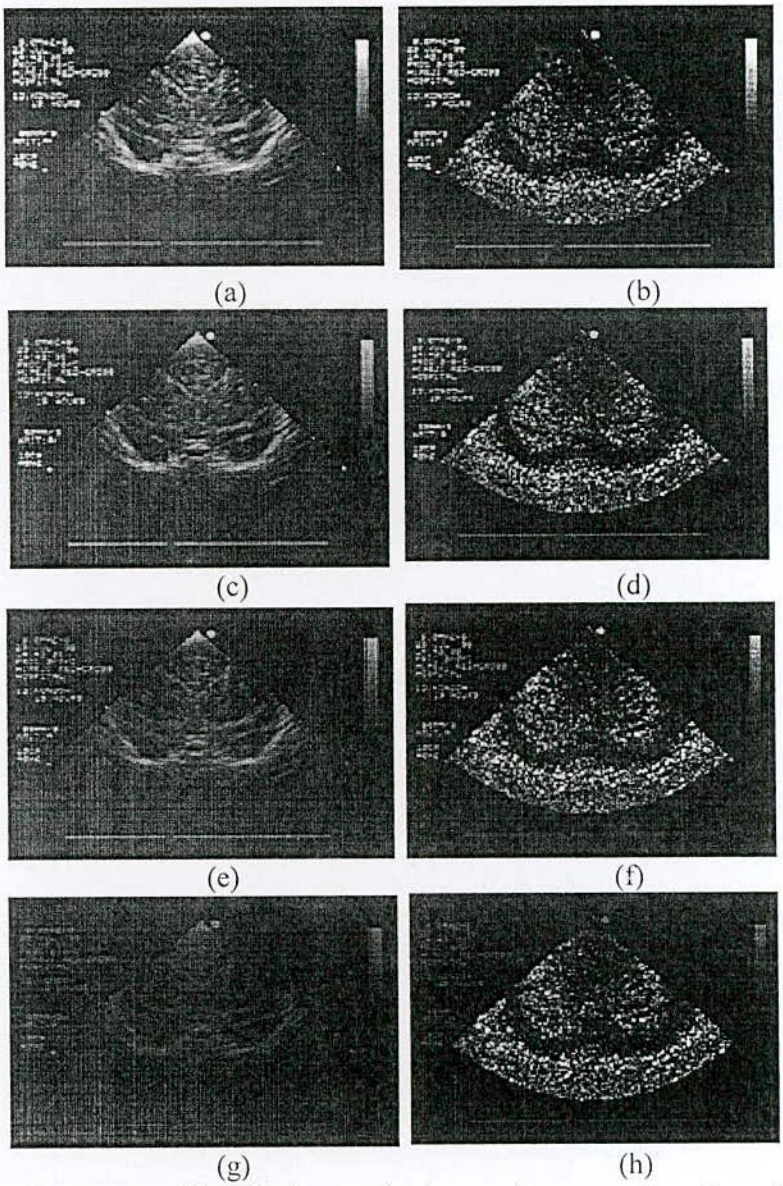

Figure 4.4: Ultrasonographic echo images in the anterior coronal section with different brightness condition and their optical flow velocity images

4.4.8 Estimation of Tissue-motion Velocity

For estimating tissue-motion velocity from neonatal cranial ultrasonogram image sequences, we have used gradient based approach and estimated the tissue motion velocity using local optimization, global optimization and combined local and global optimization. Figure 4.5 shows the estimation of optical flow velocity with different optimization methods of indicating block A of anterior coronal section of a new born baby. Table 4.1 represents some typical values of optical flow velocity estimation of same ultrasound image sequence with local optimization, global optimization and combined local and global optimization method. Figure 4.6, 4.7 and 4.8 show the Tissue motion velocity images of 30 frames in anterior coronal section using local, global and combined local global optimization of a newborn baby (Baby code: mt22h), the motion vectors are super imposed on original ultrasonogram image inside the cranial bone)

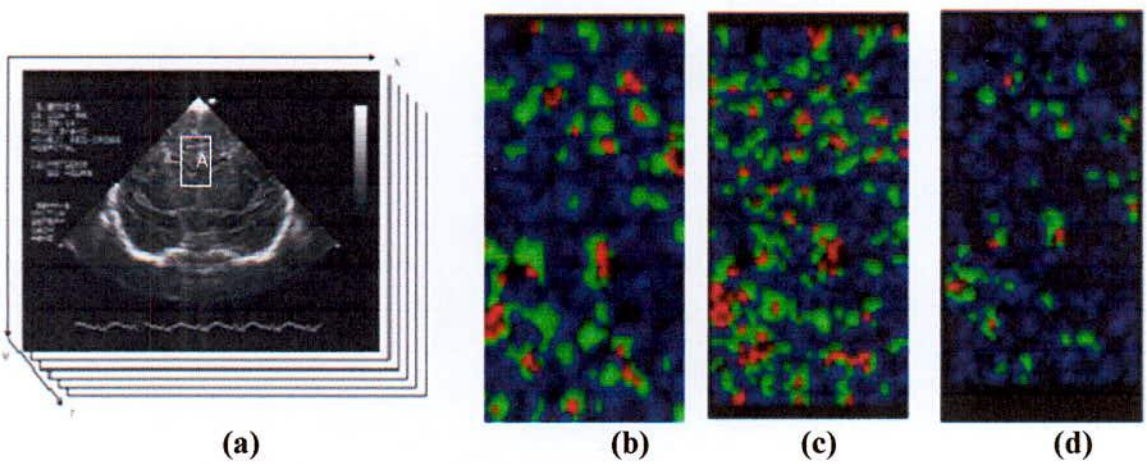

Figure 4.5: Estimation of optical flow velocity with different estimation methods of indicating block A. (a)Original ultrasonogram image sequence and optical flow images obtained by (b) Local Optimization (c) Global Optimization (d) Combined Local Global Optimization

Table 4.1: Typical optical flow velocity estimation of same ultrasound image sequence with different optimization methods

Pixel Position		Local Optimization		Global Optimization		Combined Local Global Optimization	
x	y	v_x	v_y	v_x	v_y	v_x	v_y
164	53	0.222364	0.050301	0.151495	0.027013	0.128056	0.012453
165	53	-0.007433	0.134826	0.063414	0.408364	0.000247	0.125019
166	53	-0.150040	0.147002	-0.145644	0.456895	-0.141738	0.125511
167	53	-0.125092	0.148560	-0.127871	0.219029	-0.125061	0.125035
168	53	-0.056244	0.089305	-0.006550	0.216347	-0.000189	0.009064
169	53	0.015870	-0.006073	-0.105554	0.066432	0.015625	0.000244
173	53	0.672330	0.029510	0.243566	-0.132365	0.164098	0.007906
174	53	0.432633	-0.042585	0.184174	-0.153856	0.152832	-0.008548
175	53	0.202060	-0.099701	0.076491	-0.216512	0.008583	-0.012463
176	53	0.127389	-0.110305	0.033599	-0.053990	0.007817	-0.047154
177	53	0.026485	-0.071795	0.077640	0.022309	0.018555	0.017822
178	53	-0.064793	-0.002065	0.025116	0.167806	0.016174	0.000501
179	53	-0.078643	0.076028	0.112409	0.011049	0.078136	0.008851
180	53	-0.014516	0.262262	-0.095746	0.266993	-0.011967	0.250024
181	53	0.105279	0.623765	-0.358323	0.888652	0.018442	0.512421
182	53	-0.121706	0.529756	0.623861	1.409816	0.078249	0.502197
183	53	-0.330965	0.267104	-0.060415	0.536018	0.133988	0.250494
184	53	-0.309634	0.069100	-0.008843	0.046867	-0.009155	0.033447
185	53	-0.192077	0.003266	0.092463	-0.007225	-0.007851	0.000143
186	53	-0.017380	0.003688	0.150478	-0.038620	0.017120	0.003428
187	53	0.172103	0.023179	0.255194	0.014788	0.140697	0.009529
188	53	0.322463	0.038554	0.370577	0.213679	0.250067	0.008807
189	53	0.386550	0.056893	0.443460	0.544295	0.261049	0.012209
190	53	0.346930	0.112596	0.398530	0.250726	0.314453	0.031754
191	53	0.269886	0.182931	1.014642	0.169100	0.265718	0.125313
192	53	0.393657	-0.123100	0.460162	-0.381594	0.253031	0.010500
193	53	0.284517	-0.128864	0.107436	0.045470	0.252991	-0.128297
194	53	-0.009695	-0.061873	-0.296789	-0.058527	0.009523	0.044966
195	53	-0.382507	-0.060777	-0.790799	-0.495991	-0.257483	-0.056809
196	53	-0.735039	-0.138686	-0.004105	-0.814139	-0.531761	-0.136728
197	53	-0.707225	-0.239596	-0.264907	-0.217549	-0.566476	-0.175784
198	53	-0.279193	-0.268828	0.151495	0.027013	-0.001026	-0.125135
199	53	-0.074042	0.040274	0.063414	0.408364	-0.016557	0.008103

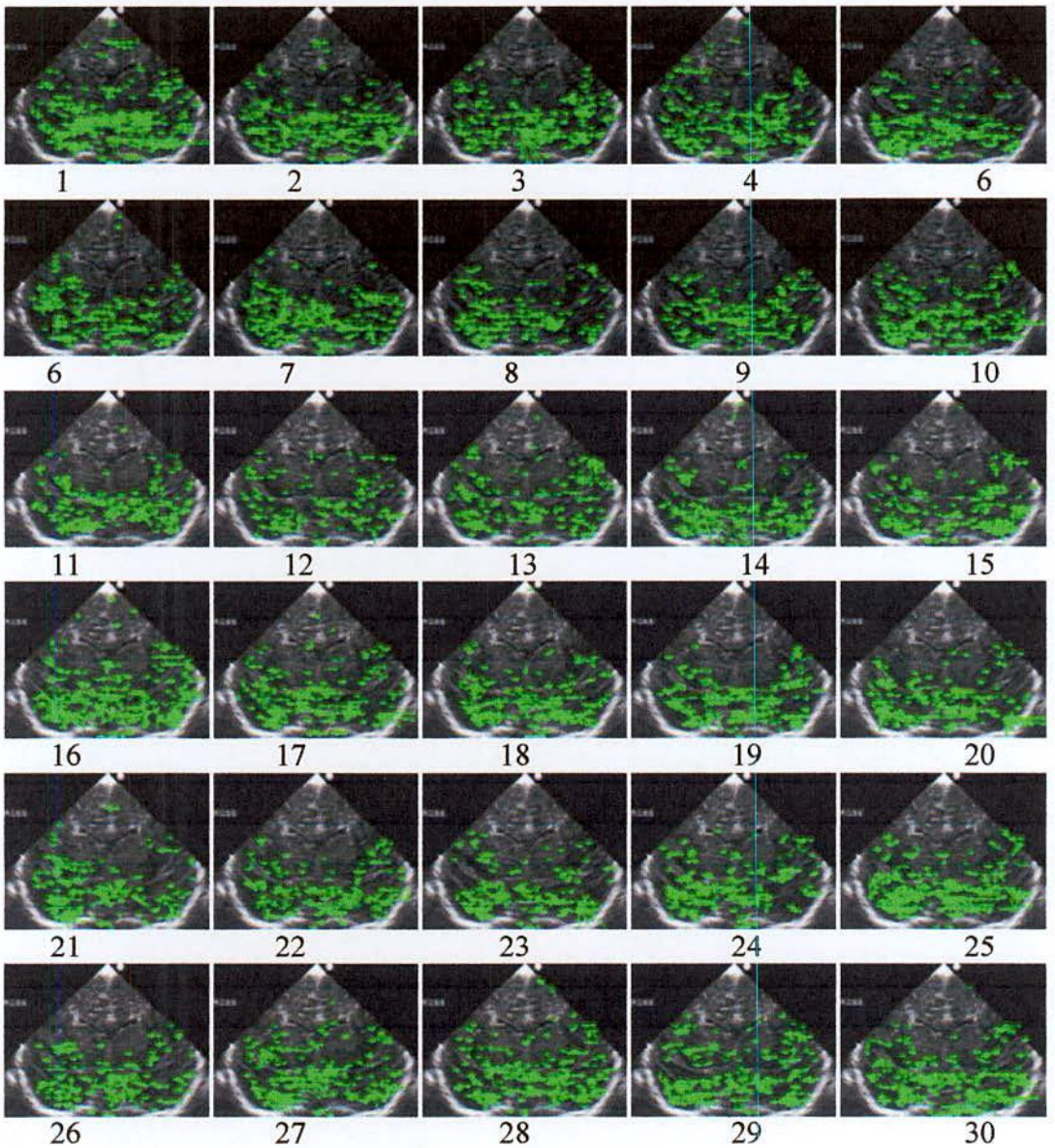

Figure 4.6: Tissue motion velocity images (motion vectors are super imposed on original ultrasonogram image inside the cranial bone) of 30 frames in anterior coronal section using local Optimization (Baby code: mt22h)

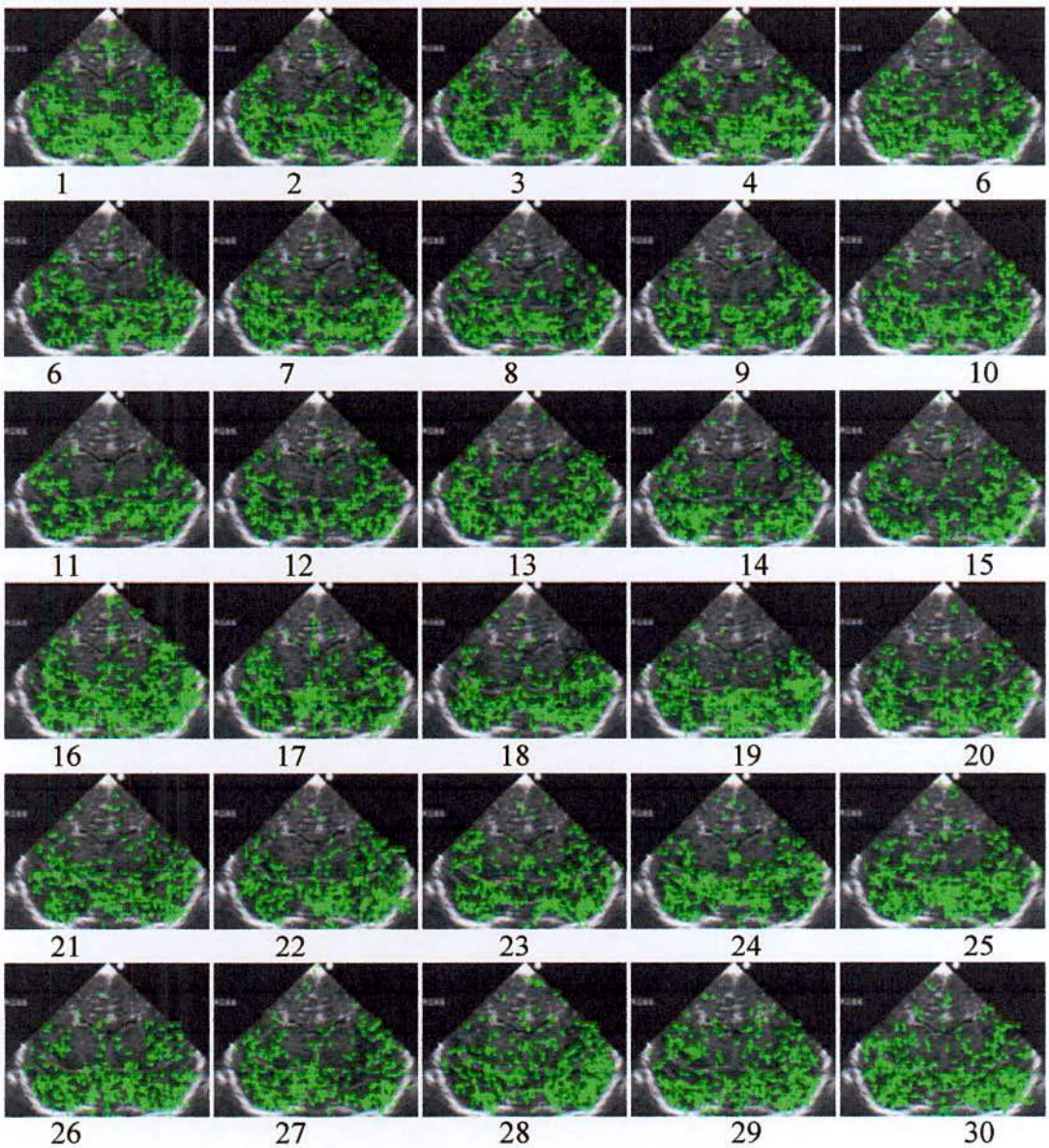

Figure 4.7: Tissue motion velocity images (motion vectors are super imposed on original ultrasonogram image inside the cranial bone) of 30 frames in anterior coronal section using Global Optimization (Baby code: mt22h)

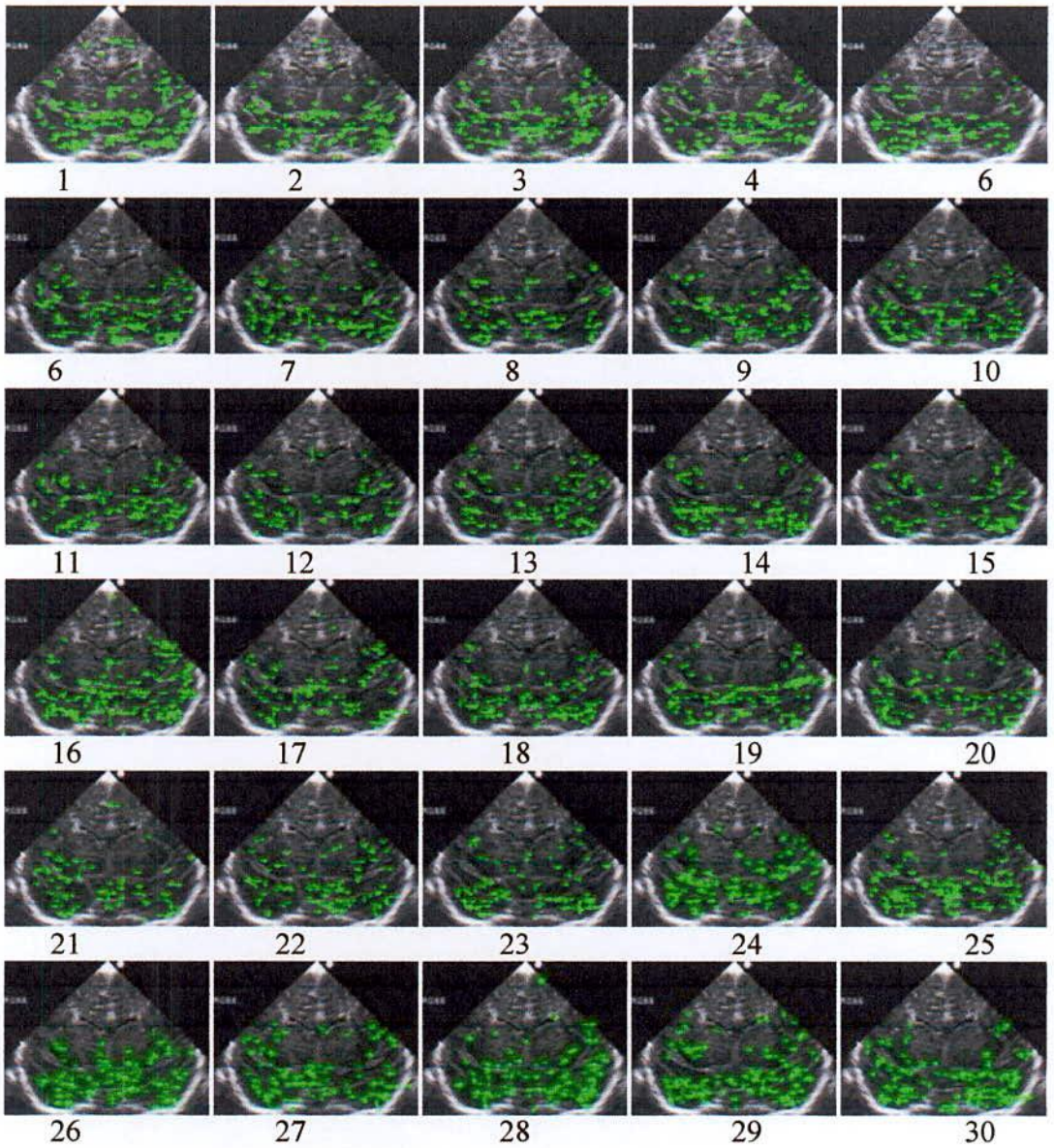

Figure 4.8: Tissue motion velocity images (motion vectors are super imposed on original ultrasonogram image inside the cranial bone) of 30 frames in anterior coronal section two using Combined local and global Optimization (Baby code: mt22h)

4.4.10 Estimation of errors in different optical flow techniques

Figure 4.9 shows the estimated error in different optical flow techniques that are applied to cranial ultrasound images. The errors are estimated of a typical section for local, global and combined local global optimization. Figure represents that the average error or normalized error is lowest in case of combined local global optimization. Combined local global optimization is more suitable for the analysis of tissue motion. Two types of average errors are also mentioned in the following tables 4.2 and 4.3. In table 4.2, we show percentage of pixels which have errors more than 1 pixel in the local region. Section II, III, IV and V represent the different coronal sections e.g. anterior coronal, Coronal through foramen of Monro, Coronal through foramen magnum, slightly posterior coronal section respectively. From the table it is shown that the percentage of error pixel is lowest in case of combined local global optimization. Moreover, the average error in each frame is shown in table 4.3 which is calculated by using(4.4.45). It represents the residual error or normalized error in different coronal section of a newborn baby. It is found that combined local global optical flow technique contains least error in both tables.

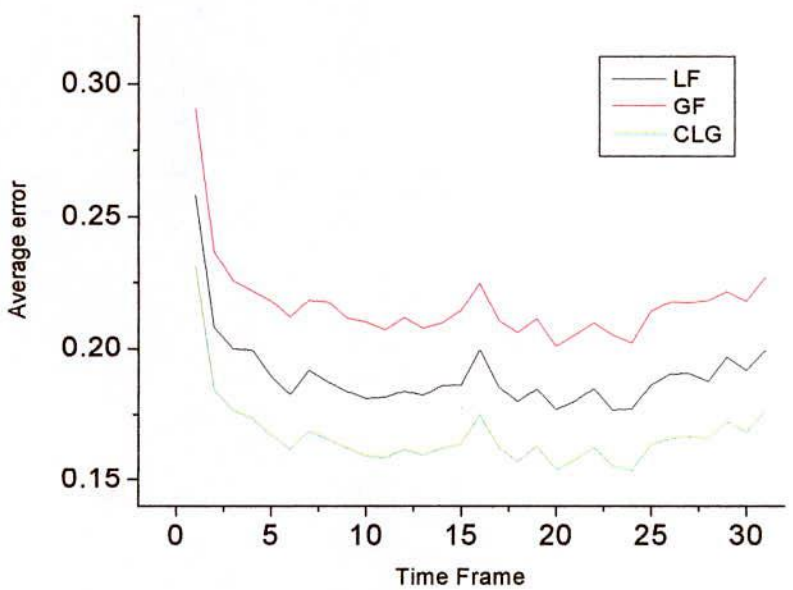

Figure 4.9: Average error of different optical flow estimation as a function of time frame.

Table 4.2: Error pixel (%) in different coronal sections

Method	Section II	Section III	Section IV	Section V
LF	2.08	2.43	2.91	2.93
GF	2.78	3.25	3.91	3.81
CLG	1.66	1.98	2.34	2.30

Table 4.3: Error value (%) in different coronal sections

Method	Section II	Section III	Section IV	Section V
LF	18.08	18.43	19.34	19.79
GF	21.21	21.57	22.53	22.84
CLG	16.03	16.33	17.18	17.55

4.5 Frequency analysis of tissue motion using Fourier transform

In mathematics, Fourier analysis is a subject area which grew out the study of Fourier series. The subject was started with trying to understand when it was possible to represent general functions by the summation of simpler trigonometric functions. The attempt to understand functions (or other objects) by breaking them into basic pieces that are easier to understand is one of the central themes in Fourier analysis. Fourier analysis is named after Joseph Fourier who showed that representing a function by a trigonometric series greatly simplified the study of heat propagation. Today the subject of Fourier analysis encompasses a vast spectrum of mathematics with parts that, at first glance, may appear quite different. In the sciences and engineering the process of decomposing a function into simpler pieces, is often called an analysis. The corresponding operation of rebuilding the function from these pieces is known as synthesis. In this section, the Fourier transform is discussed briefly for the basic understanding about it and about tissue motion analysis using Fourier transform.

4.5.1 The Fourier transform

In Fourier analysis, the term Fourier transforms often refers to the process that decomposes a given function into the basic pieces [29]. This process results in another function that describes how much of each basic piece are in the original function. However, the transform often gives a more specific name depending upon the domain and other properties of the function being transformed, as elaborated below. Moreover, the

original concept of Fourier analysis has been extended over time to apply in more abstract and general situations and the general field is often known as harmonic analysis.

Fourier transform (FT) is an operation that transforms one complex-valued function of a real variable into another. In such applications as signal processing, the domain of the original function is typically in time and is accordingly called the time domain. Since the new function is frequency, the Fourier transform is often called the frequency domain representation of the original function.

There are several common conventions for defining the Fourier transform as an integral function $f(x)$:

$$\hat{f}(\xi) = \int_{-\infty}^{\infty} f(x) e^{-2\pi i x \xi}\, dx \text{ for every real number } \xi \qquad (4.5.1)$$

When the independent variable x represents time (with SI unit of seconds), the transformed variable ξ represents frequency (in hertz). Under suitable conditions, f can be reconstructed from $\hat{f}$ by the inverse transform:

$$f(x) = \int_{-\infty}^{\infty} \hat{f}(\xi) e^{2\pi i x \xi}\, d\xi \text{ , for every real number } x \qquad (4.5.2)$$

For other common conventions and notations, including using the angular frequency ω is included instead of the frequency ξ.

4.5.2 Discrete Fourier transform

The discrete Fourier transform (DFT) computes the values of the z-transform for evenly spaced points around the unit circle for a given sequence. If the sequence to be represented is of finite duration i.e. has only a finite number of non-zero values, the transform used is discrete Fourier transform. DFT finds its applications in digital signal processing including linear filtering, correlation analysis and spectrum analysis.

If $x(n)$ be a finite duration sequence then N point DFT of the sequence is expressed by

$$X(k) = \sum_{n=0}^{N-1} x(n) e^{-j2\pi nk/N} \text{ , } k = 0,1, \ldots\ldots\ldots N-1 \qquad (4.5.3)$$

And corresponding IDFT is

$$x(n) = \sum_{k=0}^{N-1} X(k) e^{j2\pi nk/N} \quad \text{, } n = 0,1, \ldots\ldots\ldots N-1 \qquad (4.5.4)$$

In general, the transformation into the frequency domain will be a complex valued function, that is, with magnitude and phase.

$$magnitude = ||X(k)|| = \sqrt{X_{real}^2 + X_{imag}^2} \qquad (4.5.5)$$

$$phase = \tan^{-1} \frac{X_{imaq}}{X_{real}} \qquad (4.5.6)$$

DFT is ideal for processing information stored in computers. In particular, the DFT is widely employed in signal processing and related fields to analyze the frequencies contained in a sampled signal, to solve partial differential equations, and to perform other operations such as convolutions or multiplying large integers. A key enabling factor for these applications is the fact that the DFT can be computed efficiently in practice using a fast Fourier transform (FFT) algorithm.

4.5 .3 Fast Fourier transform

The fast Fourier transform (FFT) is an algorithm that efficiently computes the discrete Fourier transform (DFT). The DFT of a sequence $x(n)$ of length N is given by a complex valued sequence $X(k)$

$$X(k) = \sum_{n=0}^{N-1} x(n)\mathrm{e}^{-\mathrm{j}2\pi\mathrm{nk}/\mathrm{N}} \quad , k = 0,1, \dots \dots \dots N-1 \tag{4.5.7}$$

Let W_N be the complex-valued phase factor, which is an N^{th} root of unity expressed by $W_N = e^{-j2\pi/N}$

Hence *X(k)* becomes

$$X(k) = \sum_{n=0}^{N-1} x(n)\mathrm{W}_\mathrm{N}^{\mathrm{nk}} \quad , k = 0,1, \dots \dots \dots N-1 \tag{4.5.8}$$

Similarly, IDFT becomes

$$x(n) = \frac{1}{N}\sum_{k=0}^{N-1} X(k)\mathrm{W}_\mathrm{N}^{-\mathrm{nk}} \quad , n = 0,1, \dots \dots \dots N-1 \tag{4.5.9}$$

From the above Equation it is evident that to compute all N values of DFT N^2 complex multiplications and $N(N-1)$ complex additions are required.

The most well known FFT algorithms depend upon the factorization of N, but (contrary to popular misconception) there are FFTs with O ($N\ log\ N$) complexity for all N, even for prime N. Many FFT algorithms only depend on the fact that $e^{-\frac{2\pi}{N}}$ is an N^{th} primitive root of unity, and thus they can be applied to analogous transforms over any finite field, such as number-theoretic transforms. Since the inverse DFT is the same as the DFT, but with the opposite sign in the exponent and a $1/N$ factor, any FFT algorithm can easily be adapted for it.

4.5.4 Fourier Transform of Ultrasonogram Image sequences

Consider *f(x, y)* is an ultrasonogram image of size M×N, the two-dimensional DFT is given by:

$$F(k,l) = \frac{1}{MN}\sum_{x=0}^{M-1}\sum_{y=0}^{N-1} f(x,y)e^{-j2\pi(\frac{kx}{M}+\frac{ly}{N})} \quad (4.5.10)$$

Where $k=0\ 1\ 2\ldots\ldots\ldots\ldots M-1$ and $l=0\ 1\ 2\ldots\ldots\ldots\ldots N-1$

Inverse Fourier transform is given by

$$f(x,y) = \sum_{k=0}^{M-1}\sum_{l=0}^{N-1} F(k,l)e^{j2\pi(\frac{kx}{M}+\frac{ly}{N})} \quad (4.5.11)$$

Where $x=0\ 1\ 2\ldots\ldots\ldots\ldots M-1$ and $y=0\ 1\ 2\ldots\ldots\ldots\ldots N-1$

$$Magnitude = |F(k,l)| = \sqrt{F_{real}^2 + F_{imag}^2} \quad (4.5.12)$$

$$Phase = \tan^{-1}\frac{F_{imaq}}{F_{real}} \quad (4.5.13)$$

The basis functions are sine and cosine waves with increasing frequencies, *i.e.* $F(0,0)$ represents the DC-component of the image which corresponds to the average brightness and $F(M-1, N-1)$ represents the highest frequency. Using these two formulas, the spatial domain image is first transformed into an intermediate image using N one-dimensional Fourier Transforms. This intermediate image is then transformed into the final image, again using N one-dimensional Fourier Transforms. Expressing the two-dimensional Fourier Transform in terms of a series of $2N$ one-dimensional transforms decreases the number of required computations.

Even with these computational savings, the ordinary one-dimensional DFT has N^2complexity. This can be reduced to $Nlog_2N$ if we employ the *Fast Fourier Transform* (FFT) to compute the one-dimensional DFTs. This is a significant improvement, in particular, for large images.

4.5.4: Frequency analysis of tissue motion velocity

Table 4.4: Calculation of frequency resolution

Terms	Symbol or Equation	Value
Sampling rate	Δt	33 ms
Number of samples	N	32
Nyquist frequency	$f_n=1/2\Delta t$	15.15 Hz
Frequency resolution	$\Omega=2f_n/N$	0.95 Hz

The tissue motion velocity versus time representation and intensity (magnitude) versus frequency representation gives the complementary information about the same data. The discrete Fourier transform is meaningful to inspect magnitude versus frequency plot for the changes of the discrete tissue motion velocities versus time at a particular frequency than to observe the tissue velocity with time variation. Since time variant tissue motion contains different frequency components, so analysis by Fourier transform will be helpful to detect the frequencies in which pulsation occur.

For frequency analysis, we use the absolute value of motion the specified region in temporal variations. For computing the frequency components of tissue-motion, either discrete Fourier transform (DFT) or fast Fourier transform can be used [13]. The motion appeared outside the cranial bone is not considered in case of frequency analysis. In addition, no motion is found in the region of cranial bone. The motion vectors not only vary with place but also with time. Pulsation regions are found with strong pulsation and the magnitude of motion is high in the region of middle cerebral artery and near region. Thus, it is very useful to observe the periodical variation of motion as well as the magnitude of tissue motion over time in different area where different organs are involved. The heart rate of the typical baby is 140 per minute observed at the time of image sequence capturing. Therefore, the heartbeat interval of this typical baby is 429ms. The corresponding pulsation frequency is 2.33Hz. By using sampling interval 33 ms and the number of samples 32, the frequency resolution is obtained at 0.95 Hz. Therefore, fundamental frequency of the heartbeat occurs in between 2th and 3rd harmonic frequencies of tissue-motion. The power spectrum of tissue-motion at different frequency is shown in Figure 4.11, 4.12 and 4.13 using different optical flow method. The strong

pulsation is found in the image that corresponds to the frequency of 1.90Hz and 2.85 Hz. Therefore, strong pulsation is found in a frequency, which is not the fundamental frequency of heartbeat frequency but the harmonic frequency of pulsation frequency. This fact represents that pulsation is not sinusoidal, and the period of Fourier transform is not equal to the integer time of the period of heartbeats.

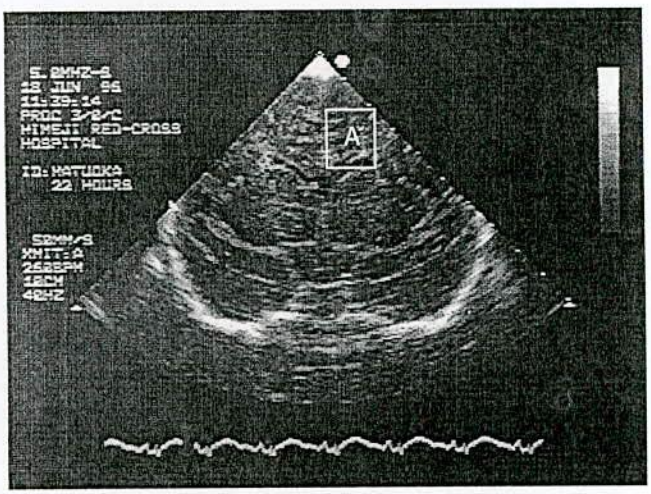

Figure 4.10: Corpus callosum region is indicated by block A in ultrasonogram image of anterior coronal section of a neonate.

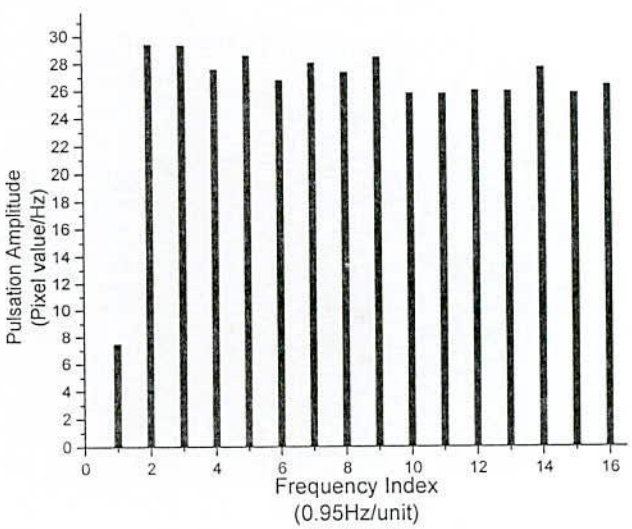

Figure 4.11: The pulsation amplitude spectrum density at different frequency of block A using local optimization.

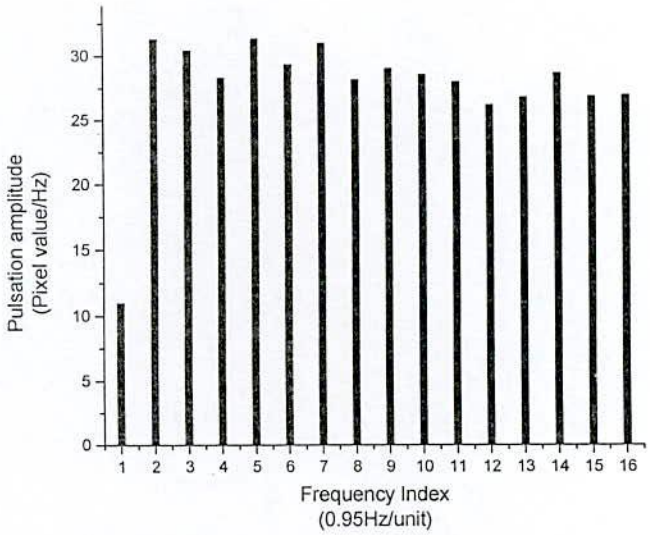

Figure 4.12 The pulsation amplitude spectrum density at different frequency of block A using global optimization.

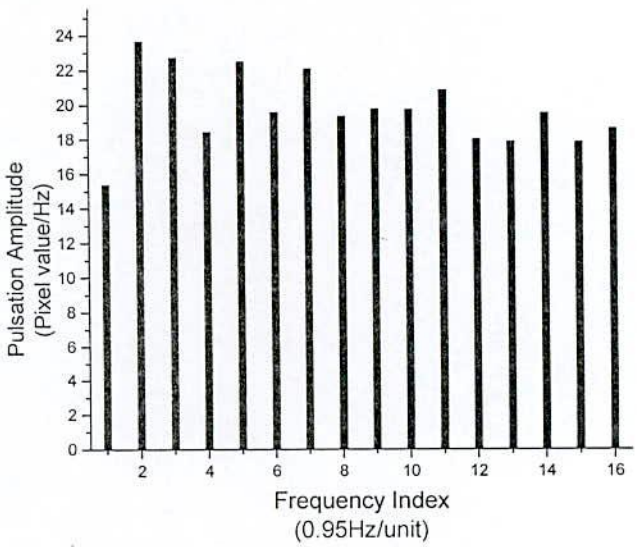

Figure 4.13: The pulsation amplitude spectrum density at different frequency of block A using Combined Local and Global optimization.

4.5.5 Strength of pulsation of tissue-motion

Figure 4.14(a) shows typical pulsation frequency image of coronal through the foramen magnum section of normal neonates and asphyxiated neonate. In a normal neonatal, the pulsation tissue-motion is appeared mainly along and around the middle cerebral artery and other essential arteries and organs in the brain. Here only anterior coronal section is shown in figure 4.14. In the figures, the red color shows the highest strength pulsation and blue color shows the lowest strength pulsation and green color is the midline of red and blue.

The pulsation tissue-motion is also found at the terminal branches of middle cerebral artery and around the corpus callosum. The corpus callosum and Middle cerebral artery are shown by white block (A) and (B) respectively in the anterior coronal section. It is sometimes difficult for conventional Doppler-based ultrasonograph to visualize such wide and fine distribution of blood flow as shown in Figure 4.14. This is because the sensitivity of the Doppler-based technique decreases with the blood flow perpendicular to the propagation direction of the ultrasound beam.

Figure 4.14(b) shows pulsation frequency image of coronal through the foramen magnum section of an asphyxiated neonate, where the pulsation tissue-motion is shown around the thalamus and corpus callosum in common with that in the normal neonate. However, the area of pulsation motion region is much less than that appeared in the normal one. The averaged strength of pulsation tissue-motion is also less than that of the normal neonate.

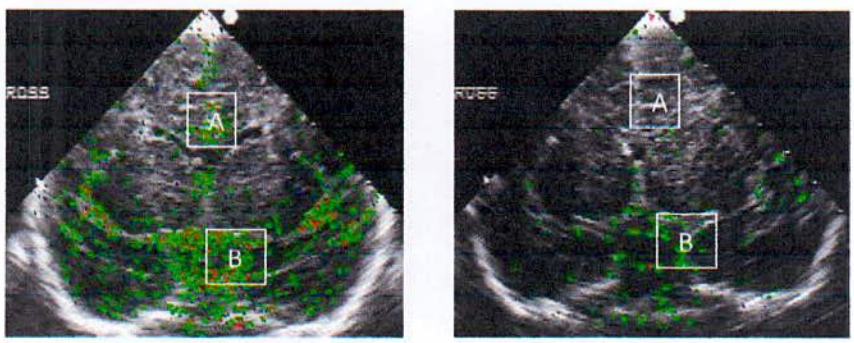

(a) (b)

Figure 4.14: Pulsation amplitude image of anterior coronal section using Fourier transform approach (a) Normal Development. (b) Asphyxiated Neonate.

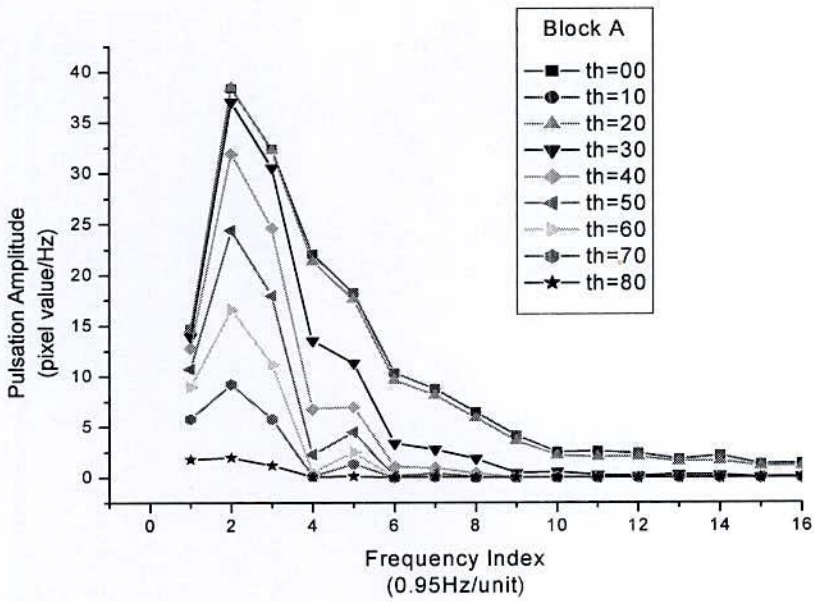

(a)

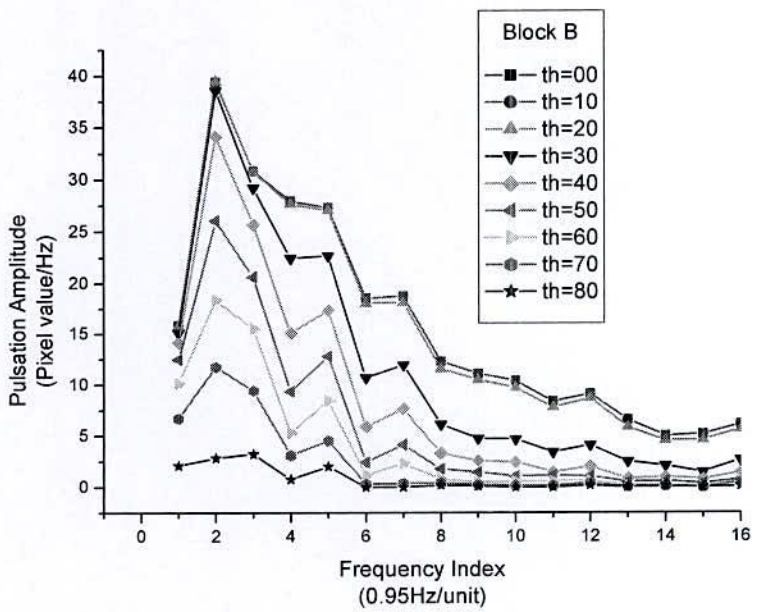

(b)

Figure 4.15: Pulsation amplitude as a function of frequency index in the mentioned block (a) Block A and (b) Block B of anterior coronal section for normal neonate (Baby code: mt22h)

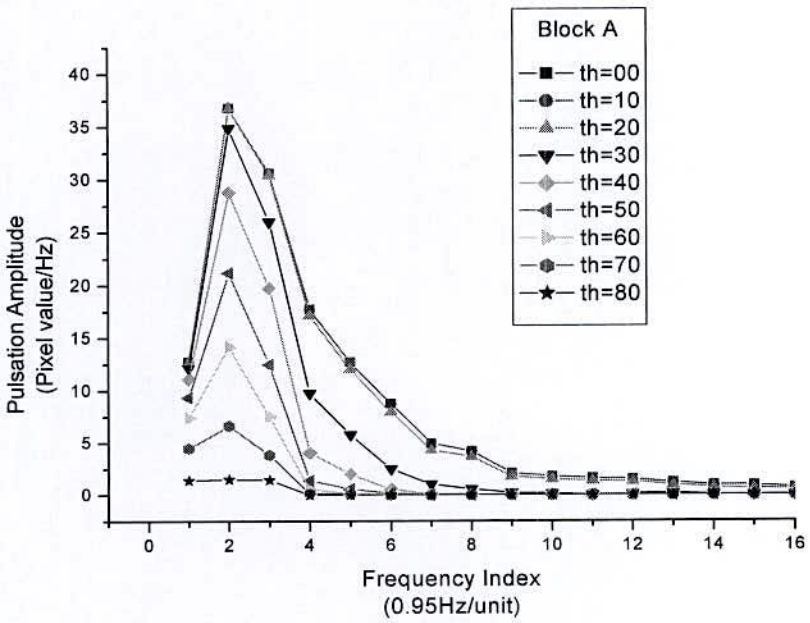

(a)

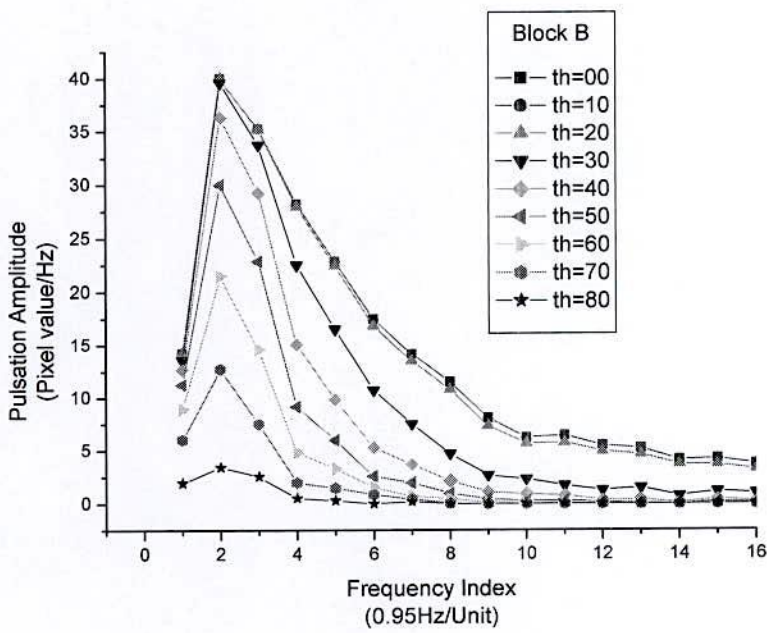

(b)

Figure 4.16: Pulsation amplitude as a function of frequency index in the mentioned block (a) Block A and (b) Block B of anterior coronal section for normal neonate (Baby code: ko19h)

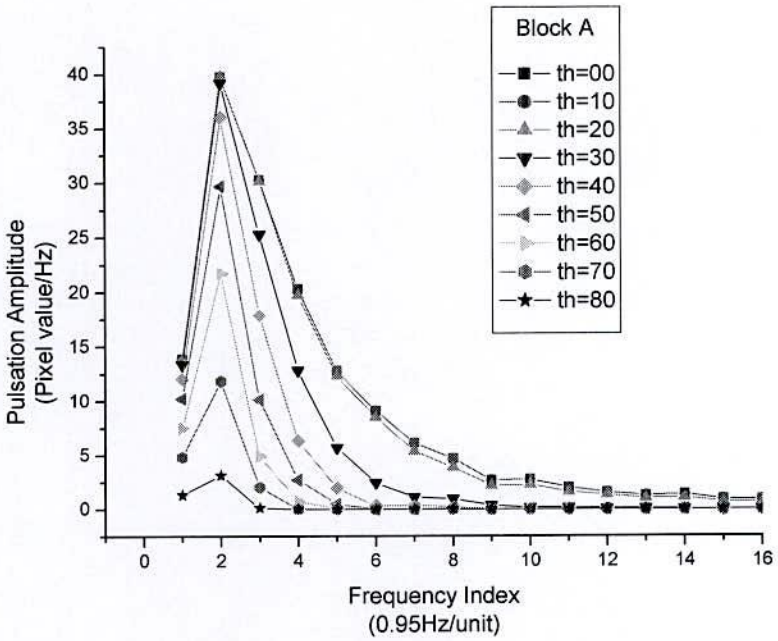

(a)

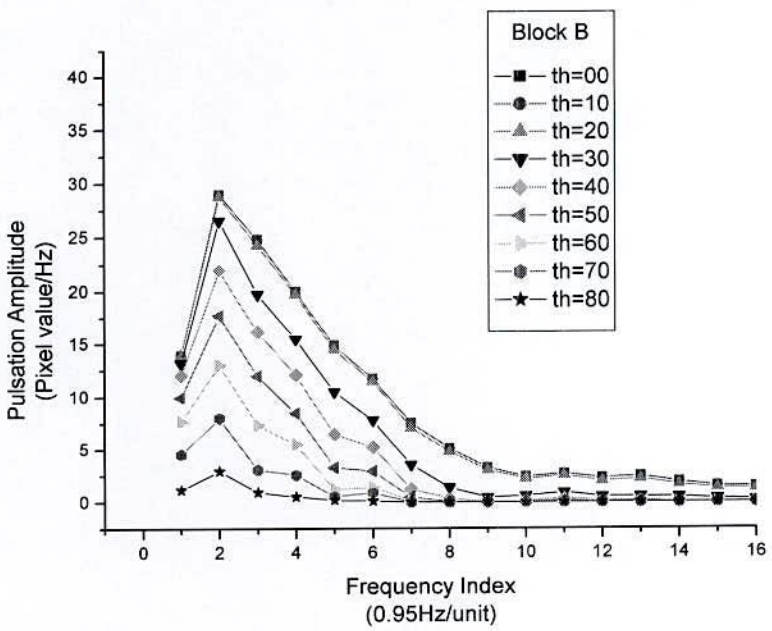

(b)

Figure 4.17/1: Pulsation amplitude as a function of frequency index in the mentioned block (a) Block A and (b) Block B of asphyxiated neonate of anterior coronal after three hours of birth (Baby code: ya03h)

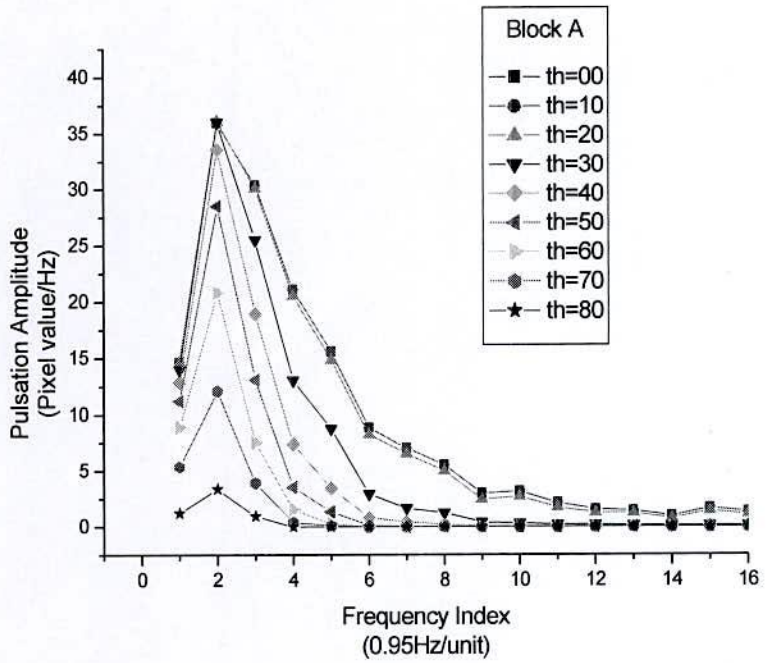

(a)

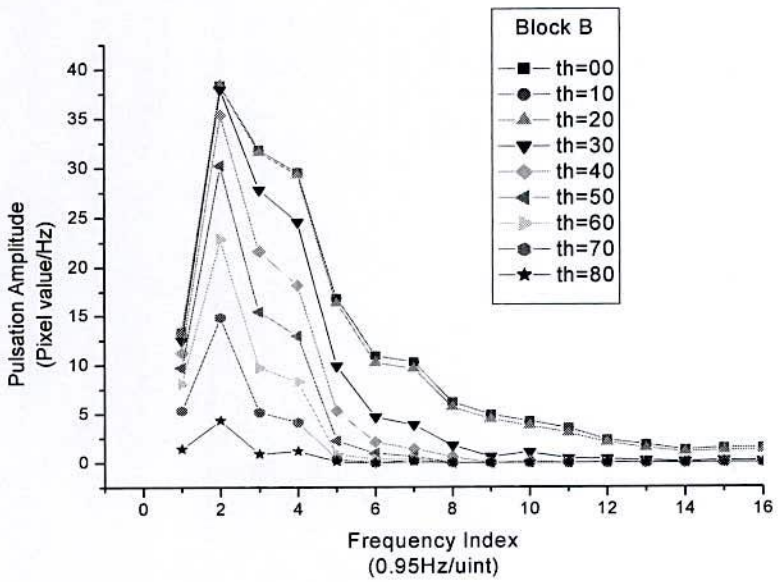

(b)

Figure 4.17/2: Pulsation amplitude as a function of frequency index in the mentioned block (a) Block A and (b) Block B of asphyxiated neonate of anterior coronal section after one day of birth (Baby code: ya01D)

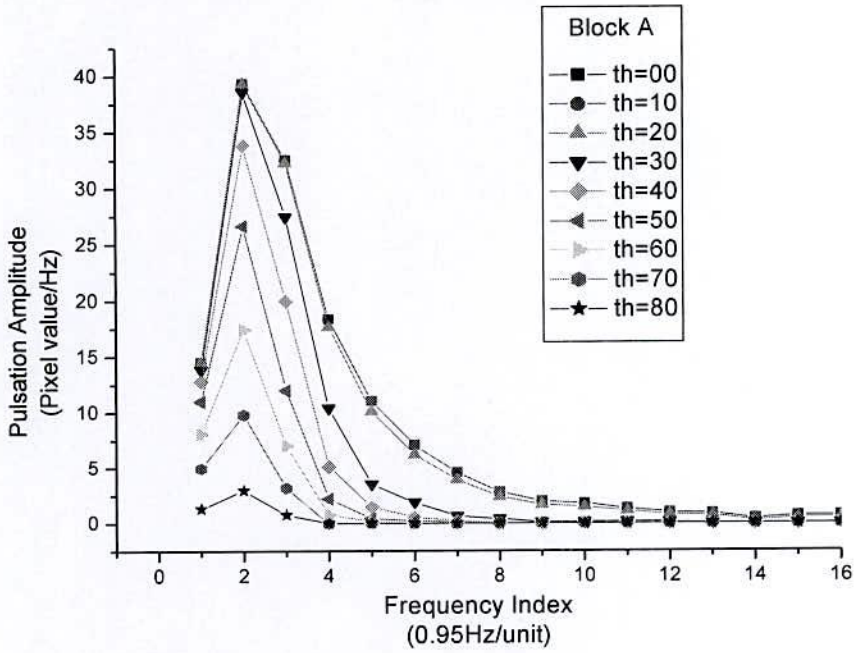

(a)

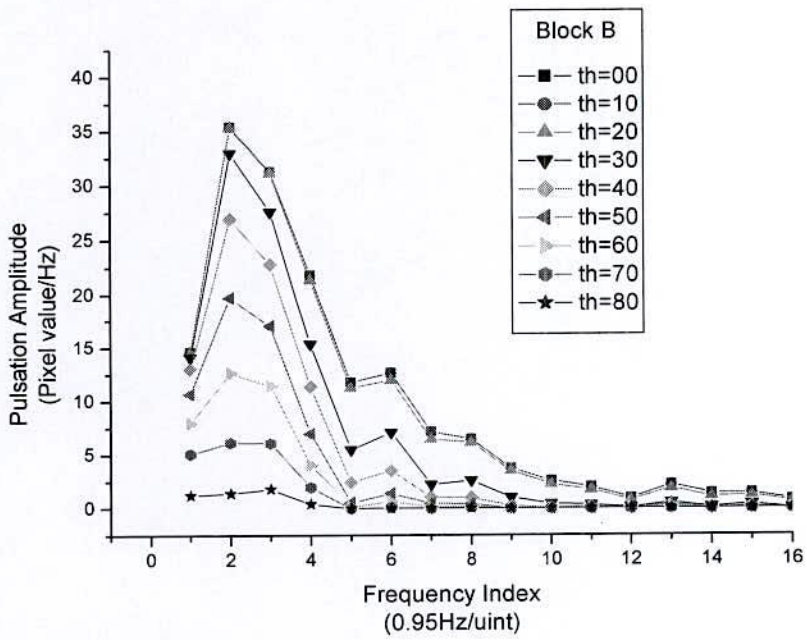

(b)

Figure 4.17/3 Pulsation amplitude as a function of frequency index in the mentioned block (a) Block A and (b) Block B of asphyxiated neonate of anterior coronal section after two day of birth (Baby code: ya02D)

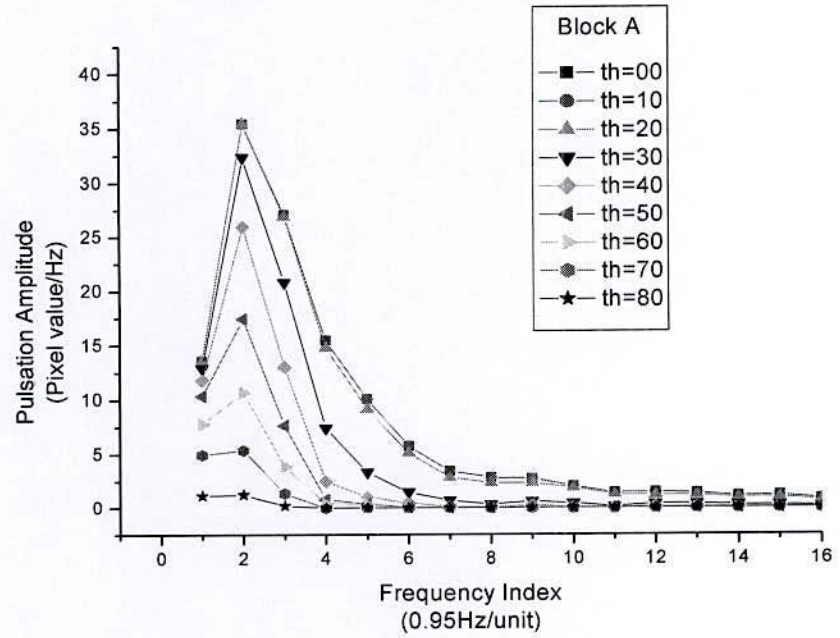

(a)

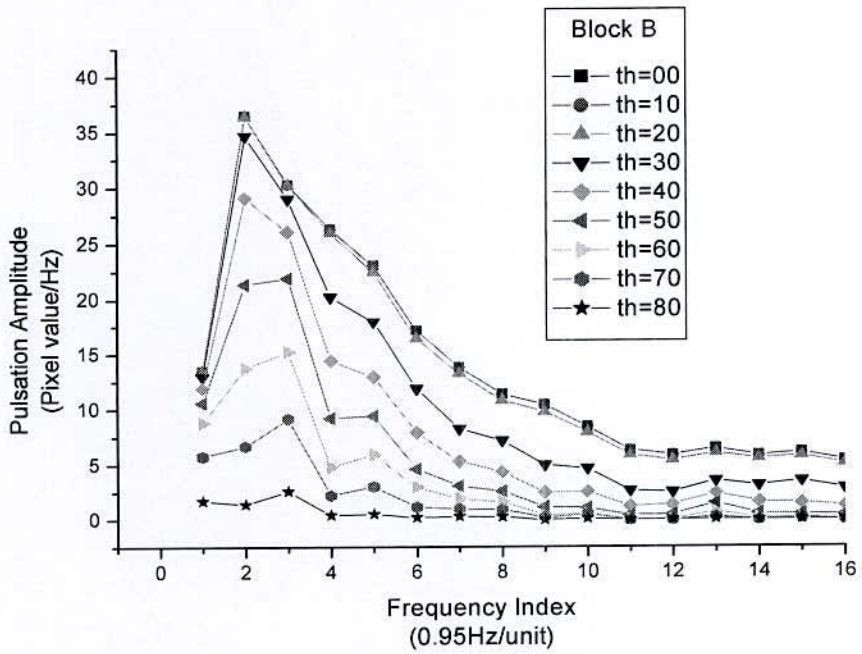

(b)

Figure 4.17/4 Pulsation amplitude as a function of frequency index in the mentioned block (a) Block A and (b) Block B of asphyxiated neonate of anterior coronal section after five days of birth (Baby code: ya05D)

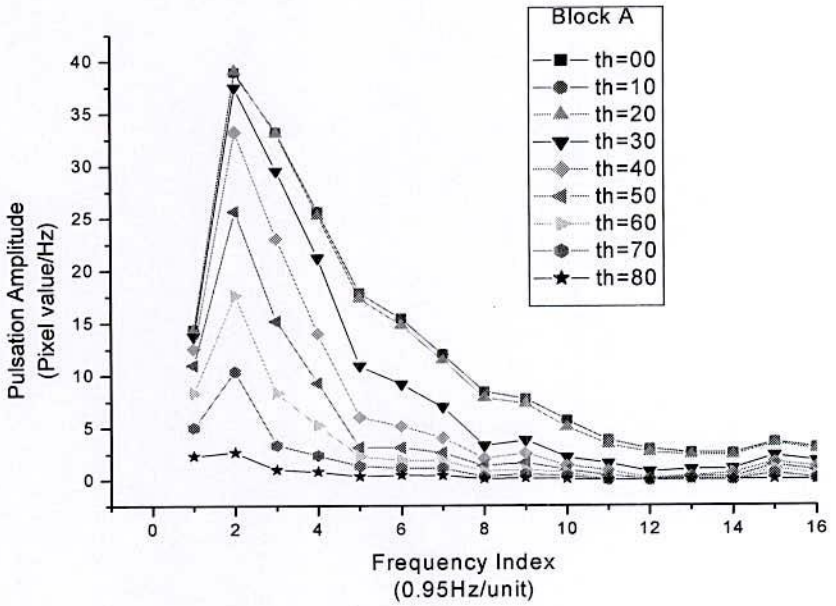

(a)

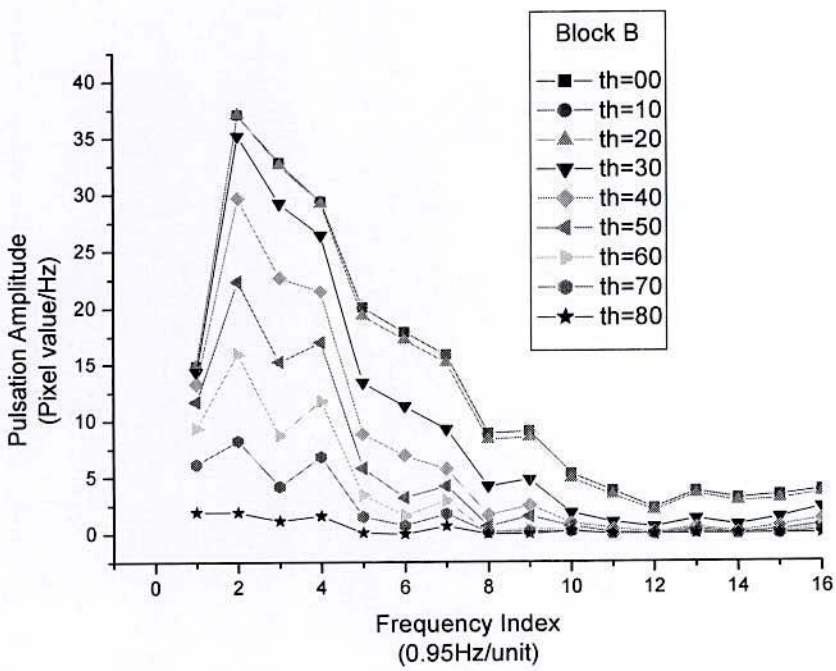

(b)

Figure 4.17/5: Pulsation amplitude as a function of frequency index in the mentioned block (a) Block A and (b) Block B of asphyxiated neonate of anterior coronal section after 20 days of birth (Baby code: ya20D)

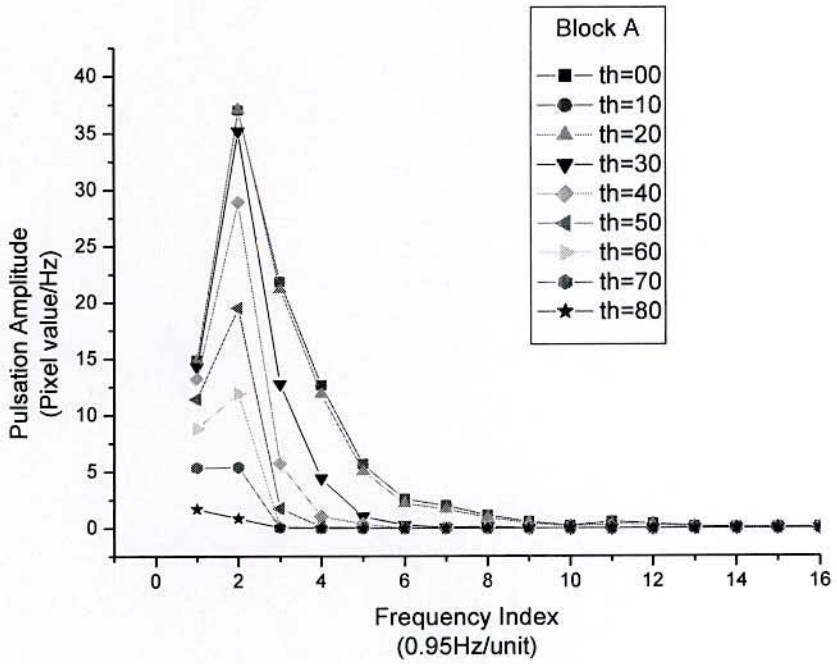

(a)

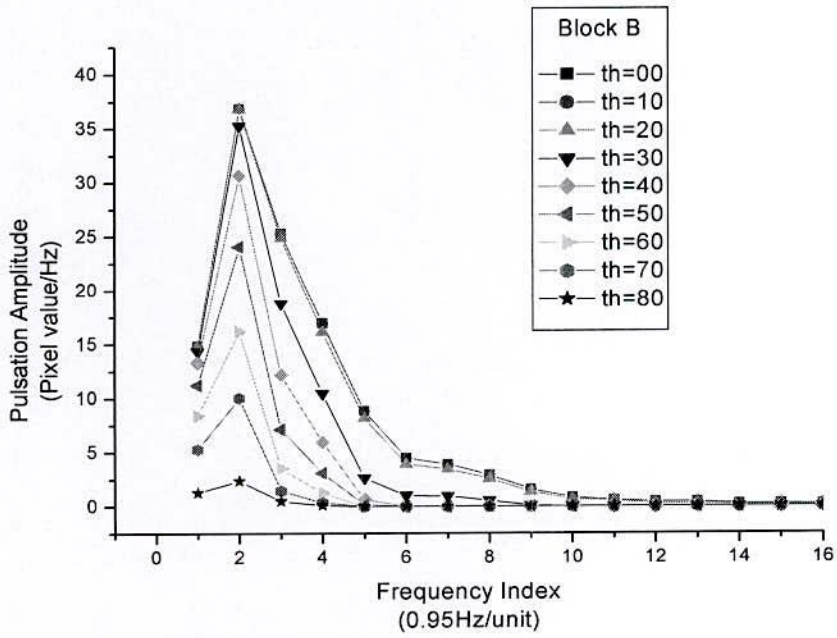

(b)

Figure 4.18/1 Pulsation amplitude as a function of frequency index in the mentioned block (a) Block A and (b) Block B of asphyxiated neonate of anterior coronal section after 15 hours of birth (Baby code: yz15h)

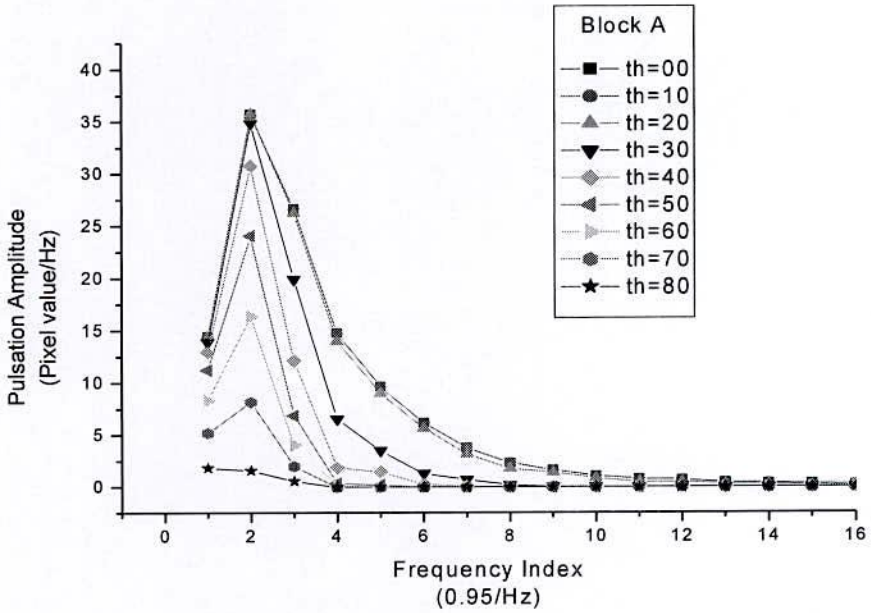

(a)

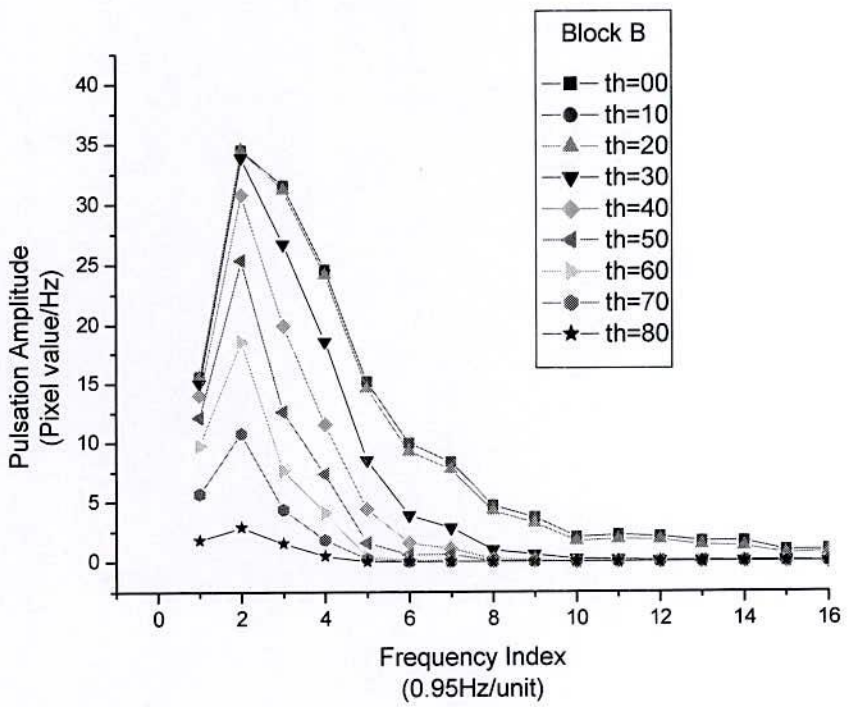

(b)

Figure 4.18/2: Pulsation amplitude as a function of frequency index in the mentioned block (a) Block A and (b) Block B of asphyxiated neonate of anterior coronal section after 01day of birth (Baby code: yz 01D)

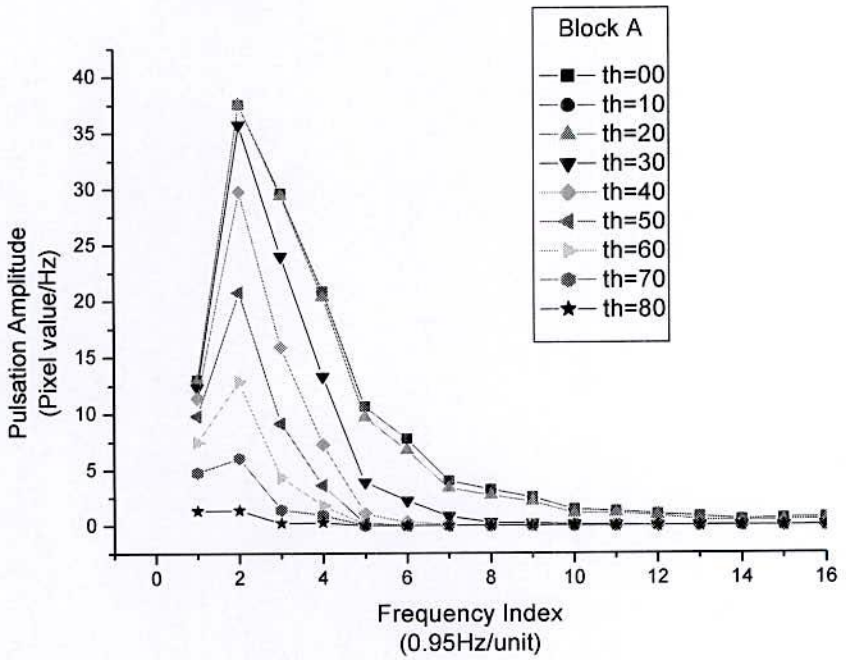

(a)

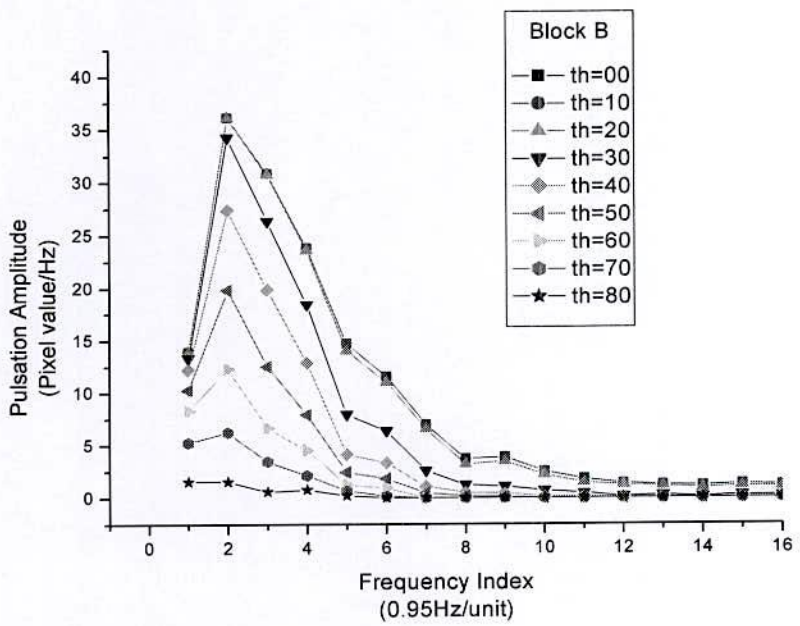

(b)

Figure 4.18/3: Pulsation amplitude as a function of frequency index in the mentioned block (a) Block A and (b) Block B of asphyxiated neonate of anterior coronal section after 02day of birth (Baby code: yz 02D)

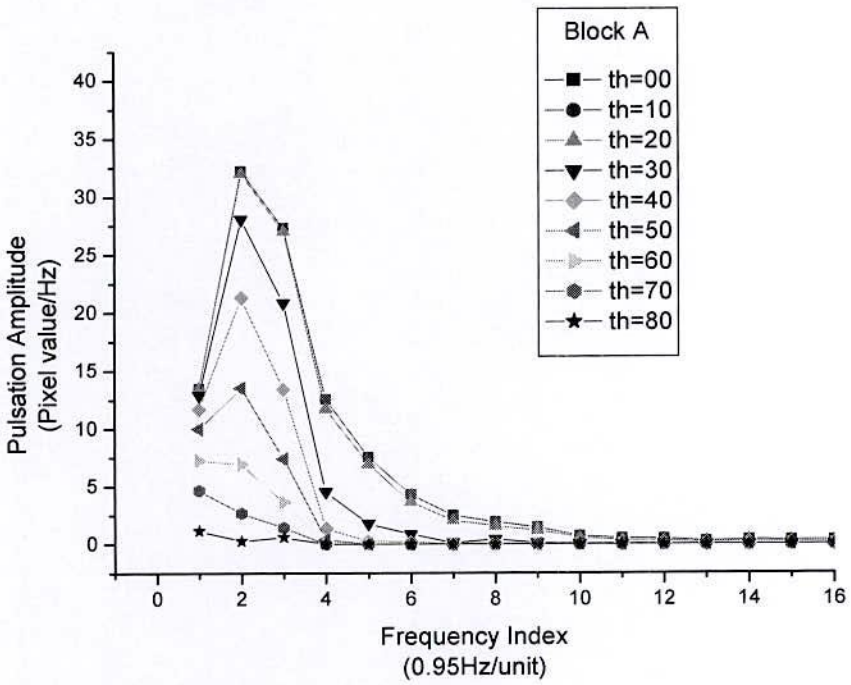

(a)

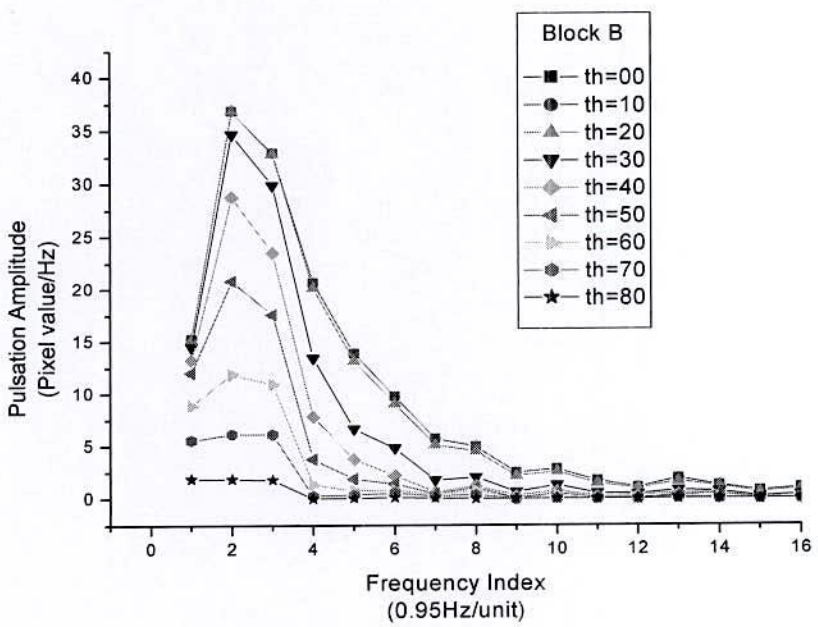

(b)

Figure 4.18/4 Pulsation amplitude as a function of frequency index in the mentioned block (a) Block A and (b) Block B of asphyxiated neonate of anterior coronal section after 05day of birth (Baby code: yz 05D)

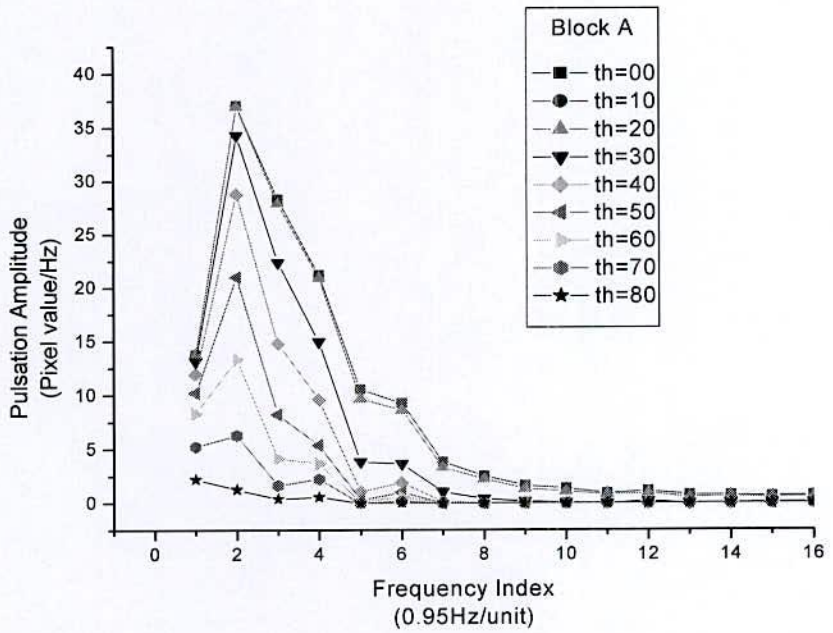

(a)

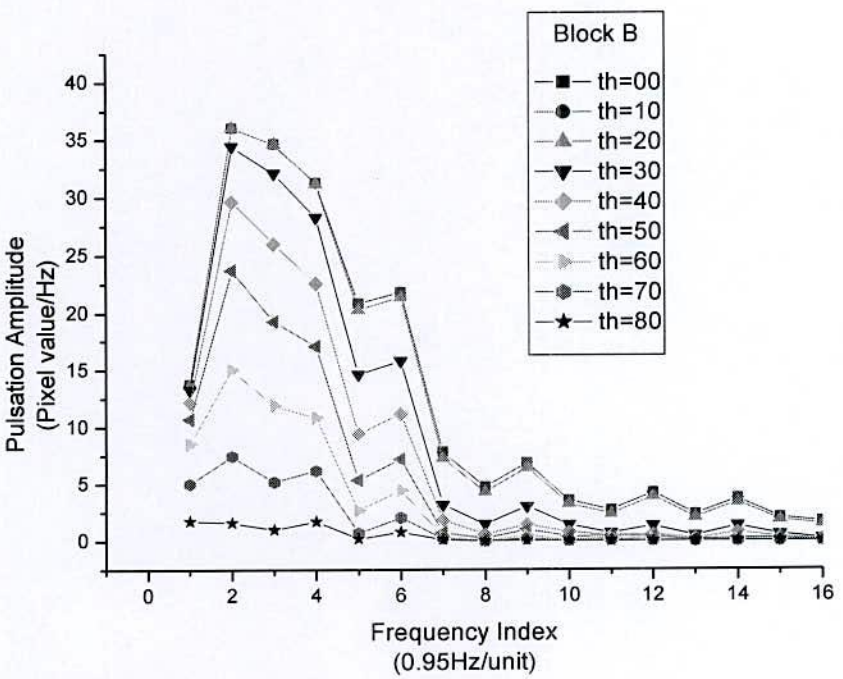

(b)

Figure 4.18/5: Pulsation amplitude as a function of frequency index in the mentioned block (a) Block A and (b) Block B of asphyxiated neonate of anterior coronal section after 07day of birth (Baby code: yz 07D)

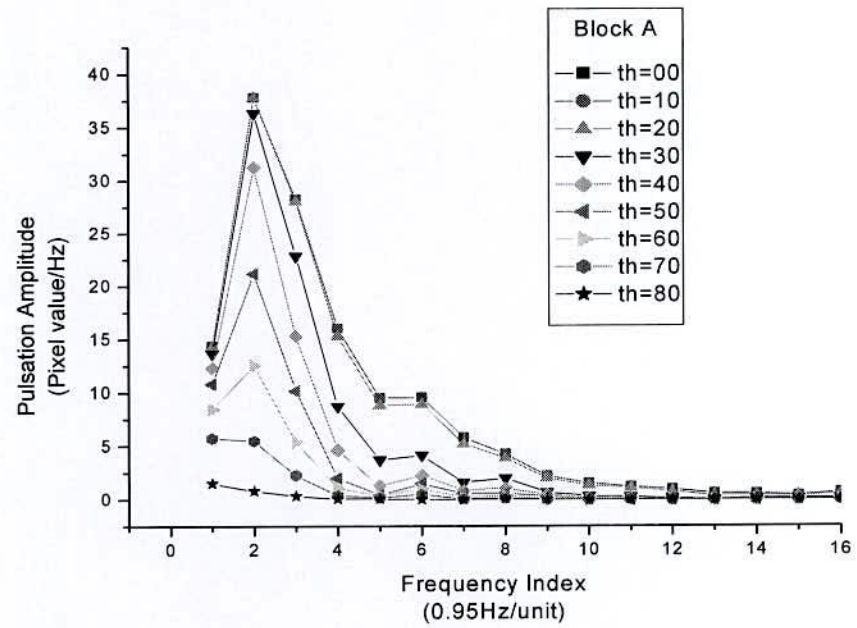

(a)

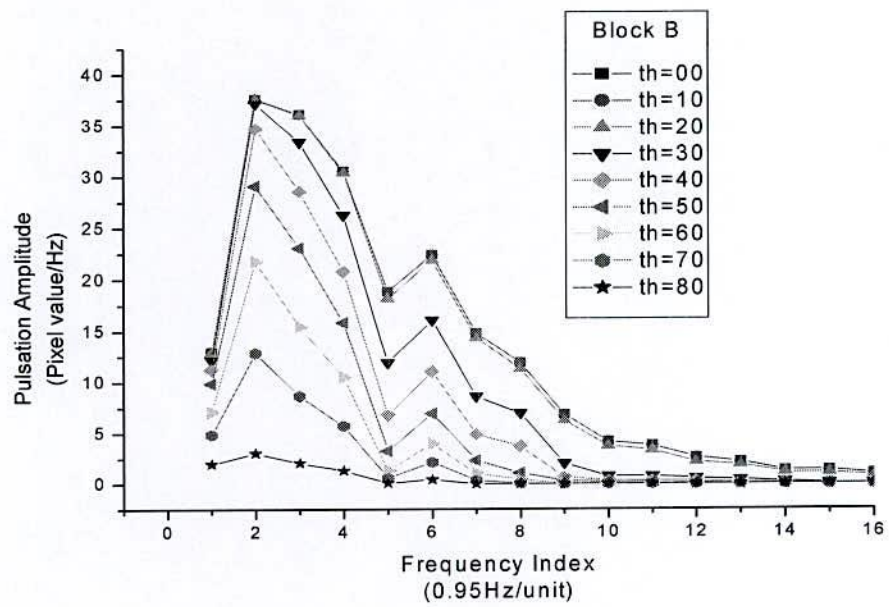

(b)

Figure 4.18/6: Pulsation amplitude as a function of frequency index in the mentioned block (a) Block A and (b) Block B of asphyxiated neonate of anterior coronal section after 09day of birth (Baby code: yz 09D)

Figure 4.15 and 4.16 show the pulsation amplitude at different frequency for block A and B of anterior coronal section for two normal neonates. Since N=32, therefore only 16 frequency components are shown. In these plots, "Th" represents the threshold value. The heart rate of these babies was in the range of 120- 140 BPM at the time of capturing images. Therefore, the heartbeat interval is 500-429 ms and the corresponding pulsation frequency is 2.00-2.33Hz. By using sampling interval 33 ms and N=32, the frequency resolution is 0.95Hz. 2^{nd} harmonics occurs at 1.90Hz and 3^{rd} harmonics occurs at 2.85Hz. Therefore, fundamental frequency of the heartbeat occurs in between 2nd and 3rd harmonic frequency of tissue-motion.

Figure 4.17 and 4.18 show the pulsation amplitude at different frequency for block A and B of coronal through the foramen of monro for two asphyxiated neonates at different time interval after birth. Table 4.5 and 4.6 represent the maximum pulsation amplitude in block A and B of anterior coronal section for asphyxiated baby, Baby code: 'ya' and 'yz' at different time intervals after birth

Table 4.5: The maximum pulsation amplitude in block A and B of anterior coronal section for asphyxiated baby, (Baby code: ya) at different time interval after birth.

Anterior Coronal Section; Baby code: ya			
No. of observations	Time of observation after	Maximum pulsation amplitude in	
		Block A	**Block B**
01	3 Hours	39.77	28.99
02	1 Day	35.99	38.37
03	2 Days	39.32	35.40
04	5 Days	35.43	36.50
05	7 Days	36.20	38.54
06	20 Days	38.93	37.12

Table 4.6: The maximum pulsation amplitude in block A and B of anterior coronal section for asphyxiated baby, (Baby code: yz) at different time interval after birth.

Anterior Coronal Section; Baby code: yz			
No. of observations	Time of observation after	Maximum pulsation amplitude in	
		Block A	**Block B**
01	15 Hours	37.02	36.89
02	1 Day	35.75	34.52
03	2 Days	37.55	36.17
04	5 Days	32.23	36.87
05	7 Days	37.07	36.03
06	9 Days	37.82	37.63

From the pulsation amplitude images of coronal section and sagittal section, the following analyses are noted:

(i) Several pulsations exhibit a periodic time variation and several of them are noisy.

(ii) The strong pulsation is observed in the region of middle cerebral artery of normal babies without asphyxia. The magnitude of such pulsation is relatively small in babies with asphyxia.

(iii) Similar situation was obtained from the region of sylvian fissure, temporal lobe, and corpus callosum, foramen of monro, cerebellum, and pons.

(iv) In some regions such as lenticular nucleus, choroid plexus and ventricle, almost no pulsation was found.

(v) In corpus callosum, strong pulsation is found in normal development but in asphyxiated neonates, weak pulsation was found.

It is verified by a pediatrician that pulsation amplitude image has significant difference between normal and asphyxiated neonates. This fact strongly supports the usefulness of the proposed method and which is useful for pediatric diagnosis. The visualization of the strength by frequency amplitude of the artery pulsation is a post processing of the conventional ultrasound image sequence. The pulsation amplitude of the neonatal cranium describes the well distribution of blood flow than that by conventional Doppler-based technique. In addition, it gives additional information about blood flow such as obstruction and local disturbance. By visualizing the pulsation in real-time, the diagnostic potential of ultrasonogram will be expanded. Therefore, the proposed technique can be useful not only for pediatrics but also for medical diagnosis in similar medical modalities.

CHAPTER 5

Visualization of Tissue-motion

5.1 Introduction

Tissue motion in neonatal cranium is an important physical parameter that is considered in discussing the pulsation strength of newborn baby for pediatric diagnosis of Ischemic diseases. From ultrasonogram movie or ultrasonogram image sequences the neonatal cranial tissue motion and the tissues with artery pulsation can be observed. For diagnosis of Ischemic diseases direct visualization and quantitative characterization of tissue motion of neonatal cranium are needed. In this research work brain tissue motion due to artery pulsation in neonatal cranium has been tried to analyze quantitatively in case of both normal and asphyxiated neonate from cranial ultrasonogram image sequences to assist pediatricians for early detection of ischemia.

5.2 Visualization of brain-tissue motion

The contribution in this work is to detect and visualize the tissue-motion in a movie of B-mode cranial ultrasound image sequence. The visualization procedure is shown block diagram of Fig. 5.1. Some parts of this work were published in [30~32]. In [14] neonatal cranial tissue motion is estimated using CLG optical flow approach, but in [30], neonatal brain tissue motion was estimated with different optical flow approaches e.g. local optimization, global optimization and combined local global optimization. Moreover, error analyses had been done in [30].

The B-mode cranial ultrasound images were taken as movies and recorded with a video tape at neonatal intensive care unit by a conventional ultrasonograph apparatus with the ultrasound probe of 5~7MHz. It was reported that the sway of the ultrasound probe and/or the movement of newborn baby head may cause artifacts of strong pulsation and the poor optimization of brightness and contrast may decrease the sensitivity of tissue motion [13]. From captured ultrasound images, some critical conditions, such as (i) sway of the ultrasound probe, (ii) sway of the head of baby, (iii) discontinuity of the image frames are checked. From ultrasound image sequence, the image data are extracted from tissue-motion image using optical flow and direct pixel value. The brain tissue motion can be visualized using optical flow magnitude and optical flow vector from ultrasound image sequences. For frequency analysis of brain tissue motion 1D Fourier transform is applied.

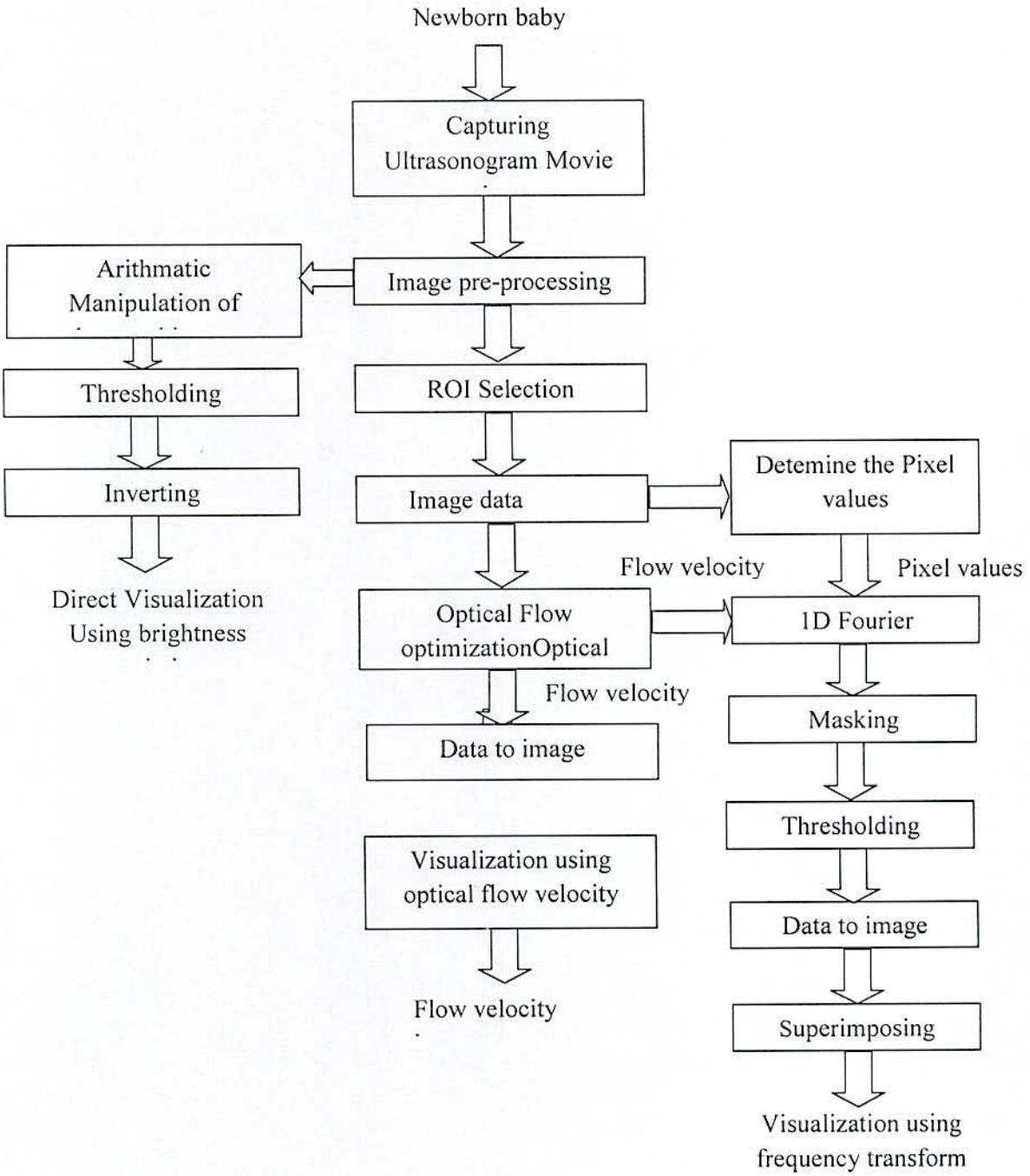

Figure 5.1: Operational flow chart for visualizing the neonatal brain tissue motion.

The 1D FFT is applied to each pixel value and simultaneously applied to whole images since the pixel values were taken carefully under constant brightness and contrast condition. The pulsation amplitude of the brain-tissue at each pixel is determined by evaluating the absolute value and argument of a heartbeat-frequency component. Different threshold values are selected for visualizing the pulsation amplitude at different harmonic frequencies. The heartbeat interval as well as frequency of heartbeat (or BPM) is determined without electrocardiograph by searching a fundamental peak in amplitude spectra in frequency domain. Moreover, the heartbeat interval can be determined by considering a small region in the ultrasonogram movie which has a relation with strong artery pulsation by Fourier transform as mentioned in [14, 29]. For clear visualization of tissue motion and strength of pulsation some threshold values are arbitrarily chosen. Finally, visualization of pulsation amplitude is obtained by superimposition of color gradation proportional to the motion strength on the original ultrasonogram at which the strength exceeds the threshold value

5.2.1 Direct Visualization using brightness variation:

The tissue motion can be observed directly from ultrasound movie. But tissue motion cannot be realized from single ultrasound image. For detection of tissue motion one image of a sequence mat be subtracted from the next image of the sequence where brightness variation represents the tissue motion. Figure 5.2(a), (b) and (c) represent the first, second and third frame of anterior coronal section and Figure 5.2(d), (e) and (f) shows the image brightness variation of successive four frames respectively. Figure 5.3(a), (b) and (c) represent the first, second and third frame of midline sagittal section and Figure 5.3(d), (e) and (f) shows the image brightness variation of successive four frames respectively. The brightness variation image is obtained by subtracting an image frame of a sequence from the next frame of the same sequences and inverting pixel values. From these images, the tissue motion can be estimated from the variation of image brightness change.

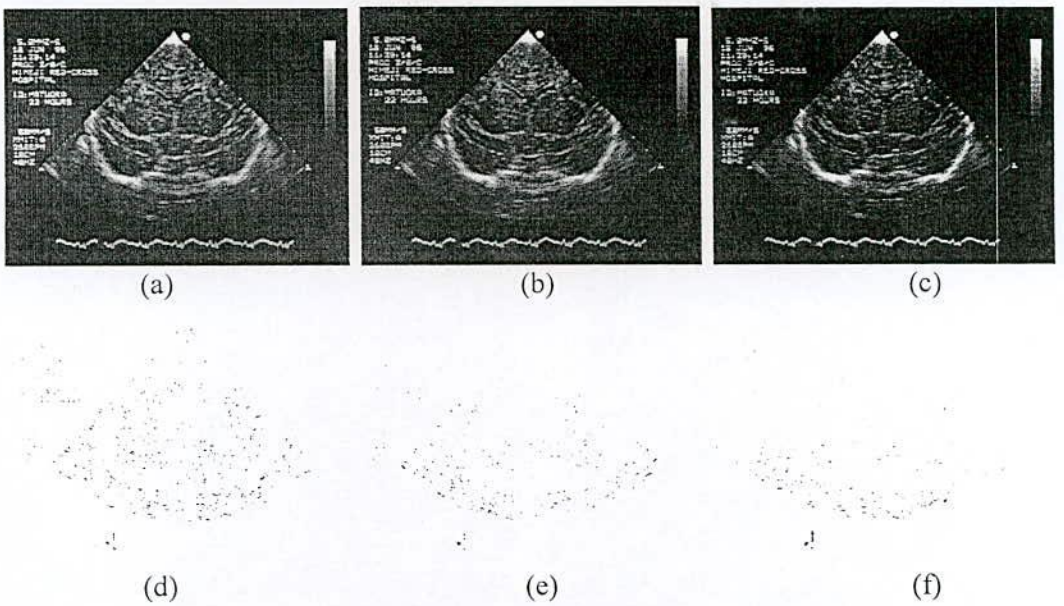

(a) (b) (c)

(d) (e) (f)

Figure 5.2: Visualization of tissue motion using brightness variation from anterior coronal image sequences.

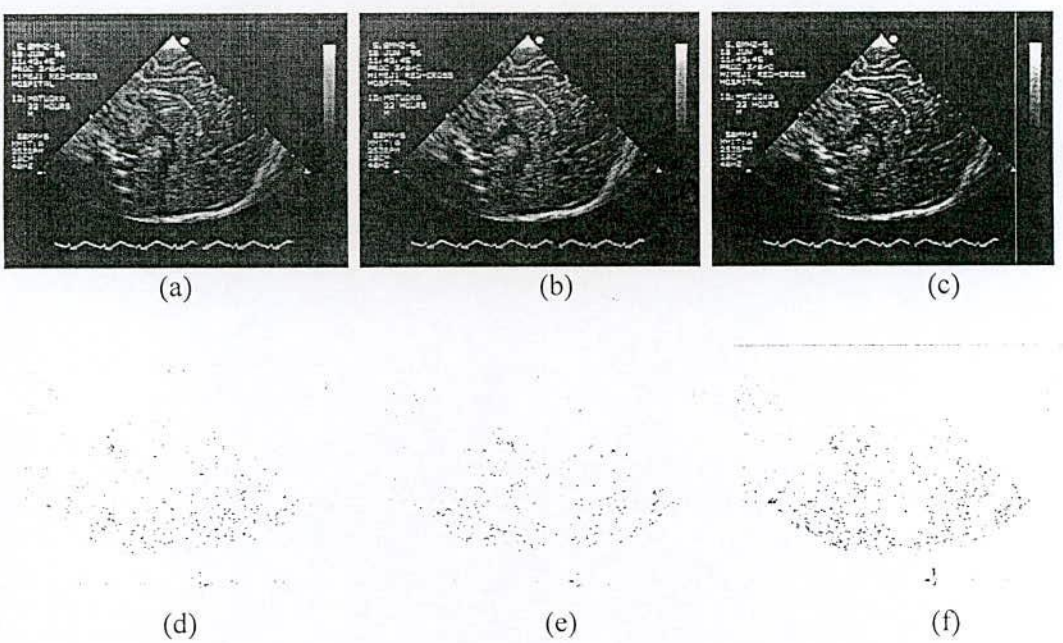

(a) (b) (c)

(d) (e) (f)

Figure 5.3: Visualization of tissue motion using brightness variation from midline sagittal image sequences.

5.2.2 Visualization using optical flow magnitude

Figure 5.4 shows the ultrasonographic images of different coronal sections and the overlapped tissue-motion velocity images are shown. LF, GF, and CLG represent the local flow, global flow, and combined localglobal flow, respectively. In Figure 5.4OI-(a) the first frame of a series of ultrasonographic echo images of frontal coronal section of a neonatal cranium is shown. This section contains several tissues and organs, such as falx cerebri-interhemispheric fissure, frontal lobe. Figure 5.4 LF-(a) shows the optical flow velocity or tissue motion velocity image in the first frame using local optimization. This image can also be regarded as the pulsation image since artery pulsation can be represented by the magnitude of tissue-motion velocity. The red region shows the strong pulsation. It is observed that the distribution of pulsation is not same within all over the image. The strength of pulsation is significant in some regions however it is very low in other regions. Weak pulsation is represented by the blue color and green region represents medium pulsation. Figure 5.4 GF-(a) and Figure 5.4 CLG-(a) represent the tissue motion velocity image of frontal coronal section using global optimization and combined local global optimization respectively. Similarly the tissue motion velocity images of different coronal planes are shown by (b): Anterior coronal (c): Coronal through foramen of Monro (d): Coronal through foramen magnum (e): Slightly posterior coronal. Figure 5.5 shows the ultrasonographic images of different sagittal sections and the overlapped tissue-motion amplitude images with local, global and combined local global optimization.

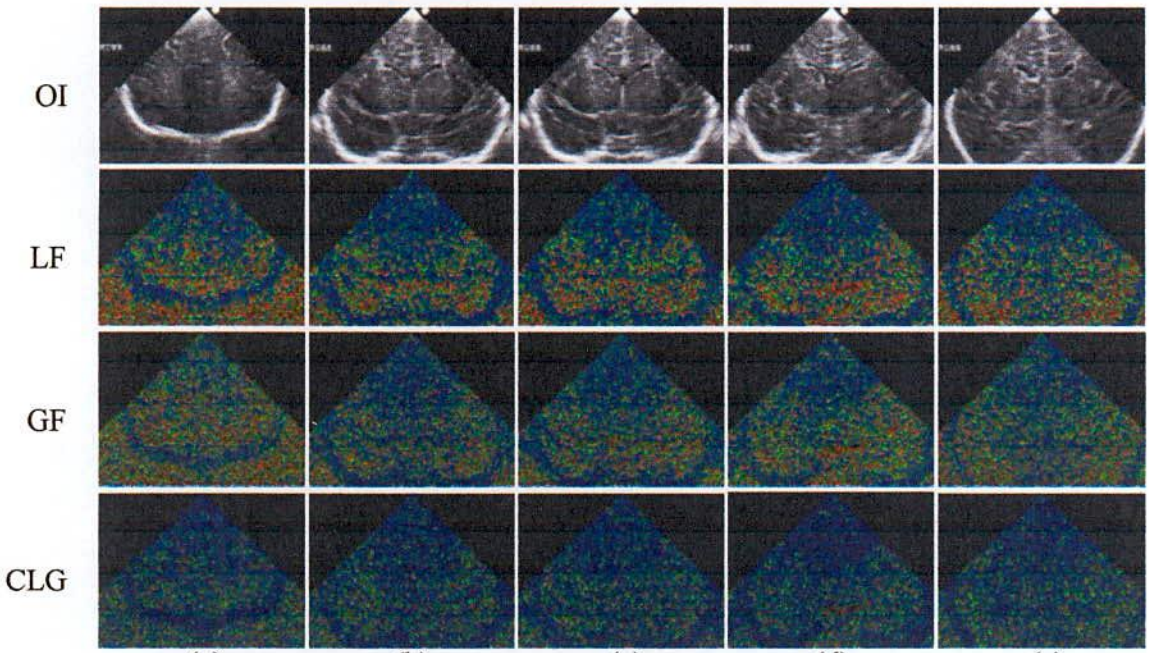

Figure 5.4: Ultrasonographic images of different coronal sections and the overlapped tissue-motion amplitude images are shown. LF, GF, and CLG represent the local flow, global flow, and combined localglobal flow, respectively. a) Frontal (b)Anterior coronal (c) Coronal through foramen of Monro (d) Coronal through foramen magnum (e) Slightly posterior coronal

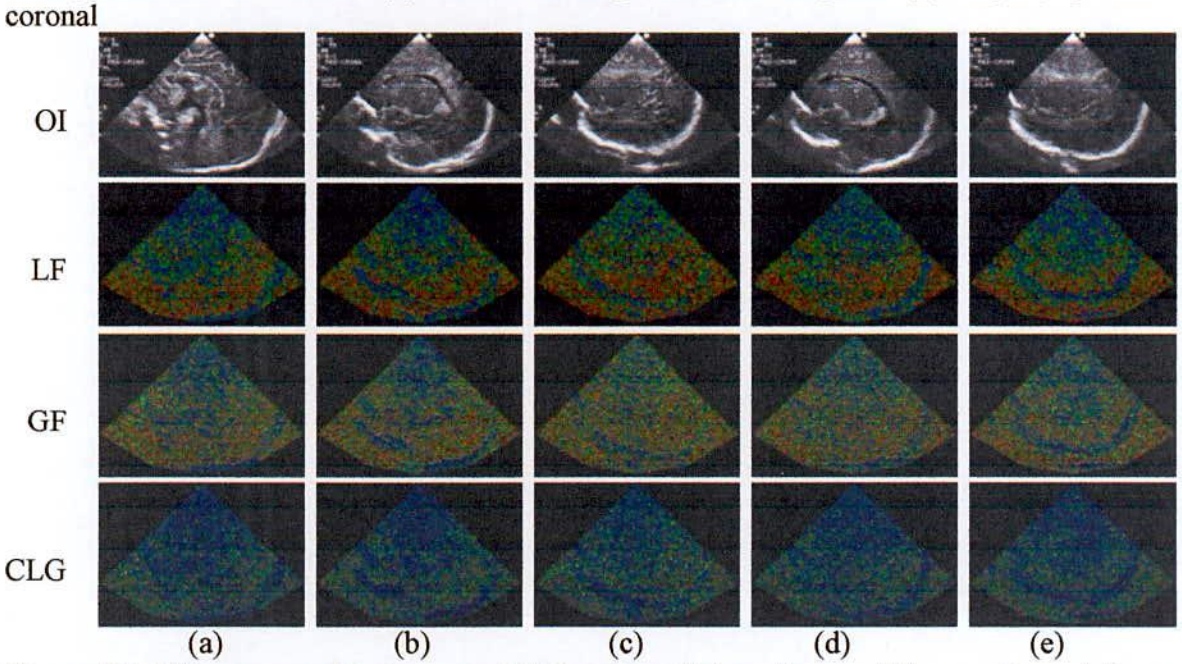

Figure 5.5: Ultrasonographic images of different sagittal sections and the overlapped tissue-motion amplitude images are shown. LF, GF, and CLG represent the local flow, global flow, and combined localglobal flow, respectively. (a) Midline sagittal (b) Lateral sagittal left (c) Most Lateral sagittal left (d) Lateral sagittal right (e) Most Lateral sagittal right

5.2.3 Visualization of tissue motion using optical flow vector

Figure 5.6 and 5.7 show the original ultrasound images of different coronal and sagittal sections and two-dimensional maps of time-variant tissue motion vector of the portion of cranial ultrasonogram. The magnitudes of tissue-motion vectors are normalized so that the distance between two neighbor pixels in the map corresponds to 0.5 pixels/frame. The tissue-motion vectors vary with place and its magnitude becomes up to a few pixel/frame at several regions within the cranial bone. The middle cerebral artery is one of the essential arteries in the brain and there are fine arteries around sylvian fissure and corpus callosum. The spatial distribution of large motion vectors has been found in the above regions. On the other hand, motion vectors become zero on the cranial bone and such tissues which is also shown in Figure 5.7 e.g. lenticular nucleus. Furthermore, the maximum vectors are aligned to the same directions at many regions of the images. The tissue-motion velocities are estimated at each pixel by using local optimization, global optimization and combined local global method for all the coronal and sagittal sections in consecutive two frames of cranial ultrasound echo images of the newborn baby head by using the spatial and temporal gradients. The ultrasound images as well as the tissue-motions overlapping the images are shown in Fig 5.6 and 5.7. We also show the amplitude of tissue-motion velocity using colour grading principle of the specified region in Fig. 5.4 and 5.5.

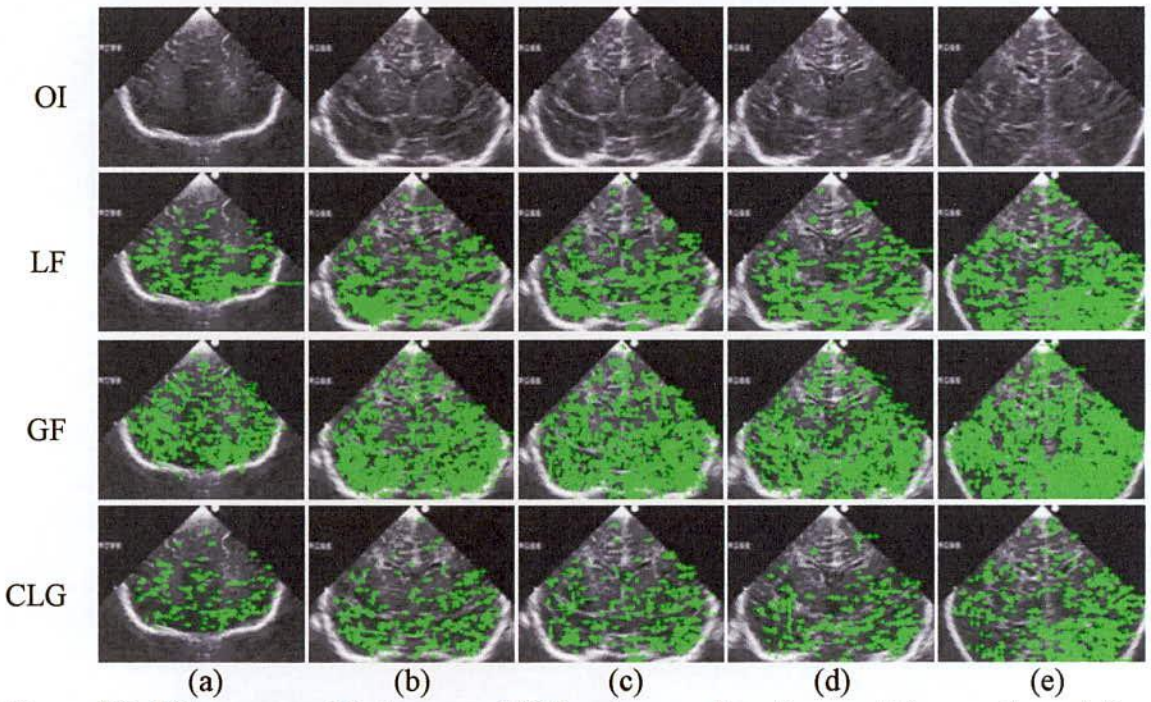

Figure 5.6: Ultrasonographic images of different coronal sections and the overlapped tissue-motion images using optical flow vectors are shown. LF, GF, and CLG represent the local flow, global flow, and combined localglobal flow, respectively. (a) Frontal (b)Anterior coronal (c) Coronal through foramen of Monro (d) Coronal through foramen magnum (e) Slightly posterior coronal

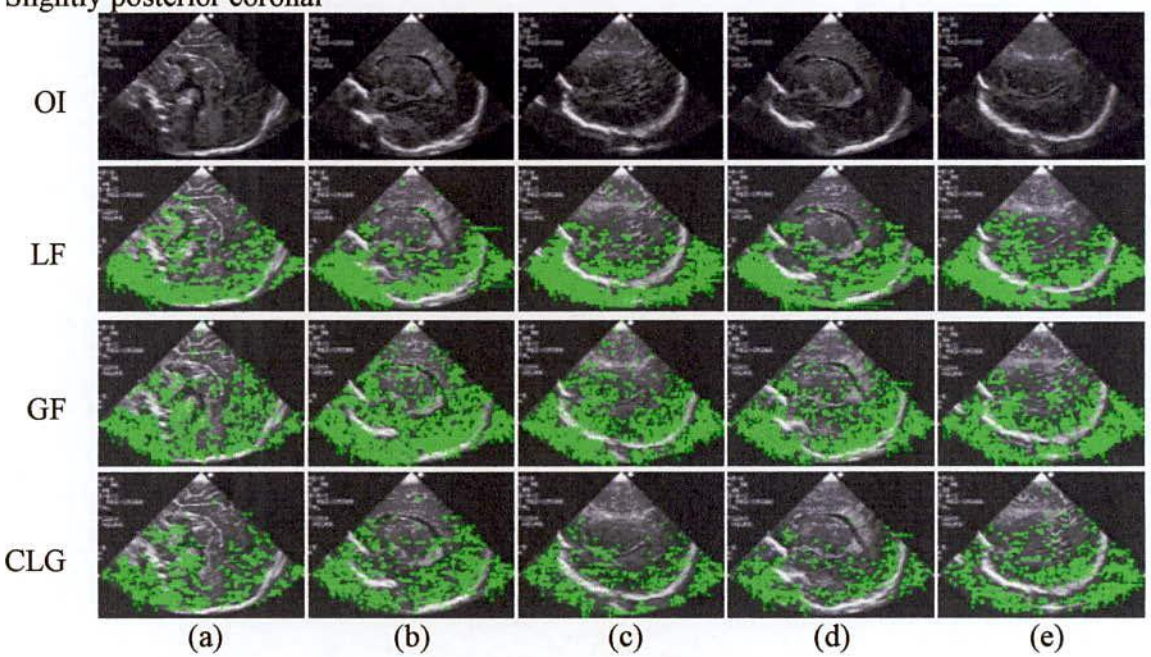

Figure 5.7: Ultrasonographic images of different sagittal sections and the overlapped tissue-motion images using optical flow vectors are shown. LF, GF, and CLG represent the local flow, global flow, and combined localglobal flow, respectively (a) Midline sagittal (b) Lateral sagittal left (c) Most Lateral sagittal left (d) Lateral sagittal right (e) Most Lateral sagittal right

5.2.4 Visualization using frequency transform of optical flow velocity

Frequency analysis is necessary to detect the frequency at which the strong pulsation occurs. The nature of the tissue motion velocity is periodic due to periodic nature of heartbeat and it varies time to time, baby to baby, and it depends on physical conditions of the prematured baby. Therefore, tissue motion contains many harmonic components of the pulsation frequency. The tissue-motion velocities repeat themselves due to the periodic nature of heartbeat. Since the heartbeat also varies due to physical condition of newborn babies, the tissue motion velocities vary from time to time, baby to baby. Artery pulsation is the periodic beating of arteries as blood pumps through arteries, and pulsation strength represents the rating of blood flow to the brain-tissue through essential arteries in the brain. The tissue motion velocity is associated with blood flow. Therefore, pulsation strength can be considered as the magnitude of tissue motion velocity, and therefore, a relationship exists between motion and heartbeat interval. Therefore, pulsation strength is lower or higher depends upon the blood flow rate or flow velocity. We use fast Fourier transform for the frequency analysis of tissue motion from optical flow velocity. Strong pulsation is found in the fundamental frequency of heartbeat frequency. Fundamental frequency of heartbeat occurs in between 2^{nd} and 3^{rd} harmonic frequencies of Nyquist frequency. The strong pulsation is also found in a frequency which is not fundamental frequency of heartbeat frequency. This fact represents that the pulsation is not sinusoidal and the period of Fourier transform is not equal to the integer times of the period of heartbeats. Figure 5.8 and 5.9 represent the Ultrasonographic images of different coronal sections and sagittal sections. The overlapped 3^{rd} harmonics of frequency pulsation images using different optical flow optimizations are shown. LF, GF, and CLG represent the local flow, global flow, and combined localglobal flow, respectively. The frequency pulsation images have been obtaind by Fast Fourier tranform of tissue motion velocity and visualised pulsation strength by color grading. Red pixels are corresponding to strong pulsation, green pixels are corresponding to medium pulsation and blue pixels are corresponding to weak pulsation.

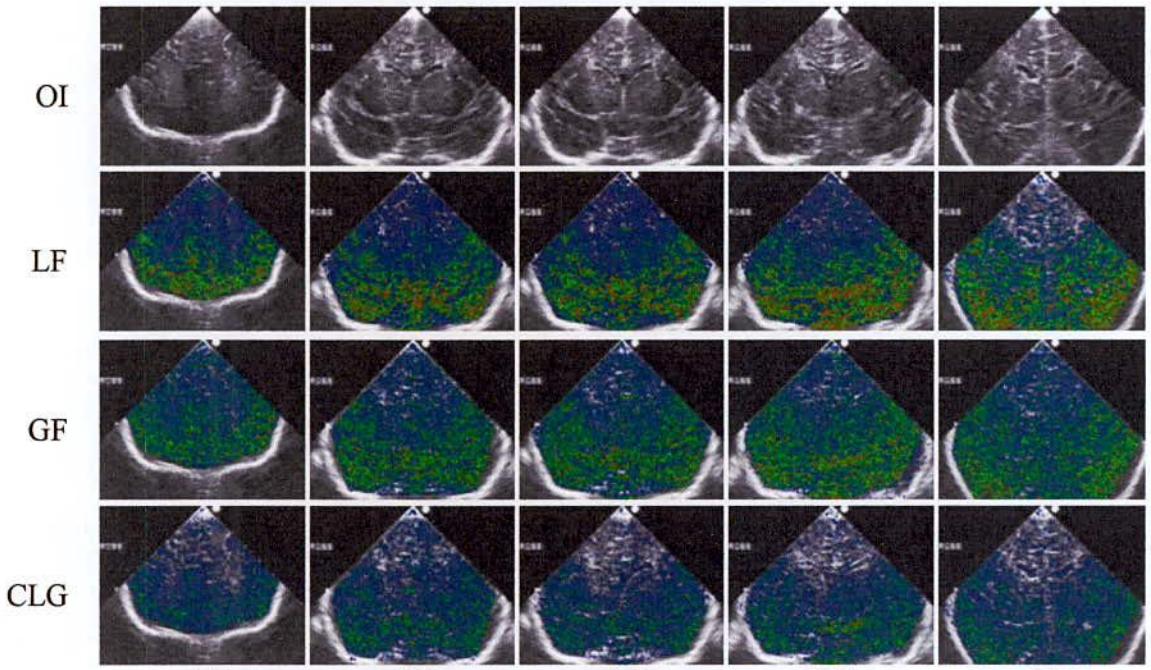

Figure 5.8: Ultrasonographic images of different coronal sections and the overlapped frequency pulsation images using different optical flow optimization are shown. (a) Frontal (b)Anterior coronal (c) Coronal through foramen of Monro (d) Coronal through foramen magnum (e) Slightly posterior coronal

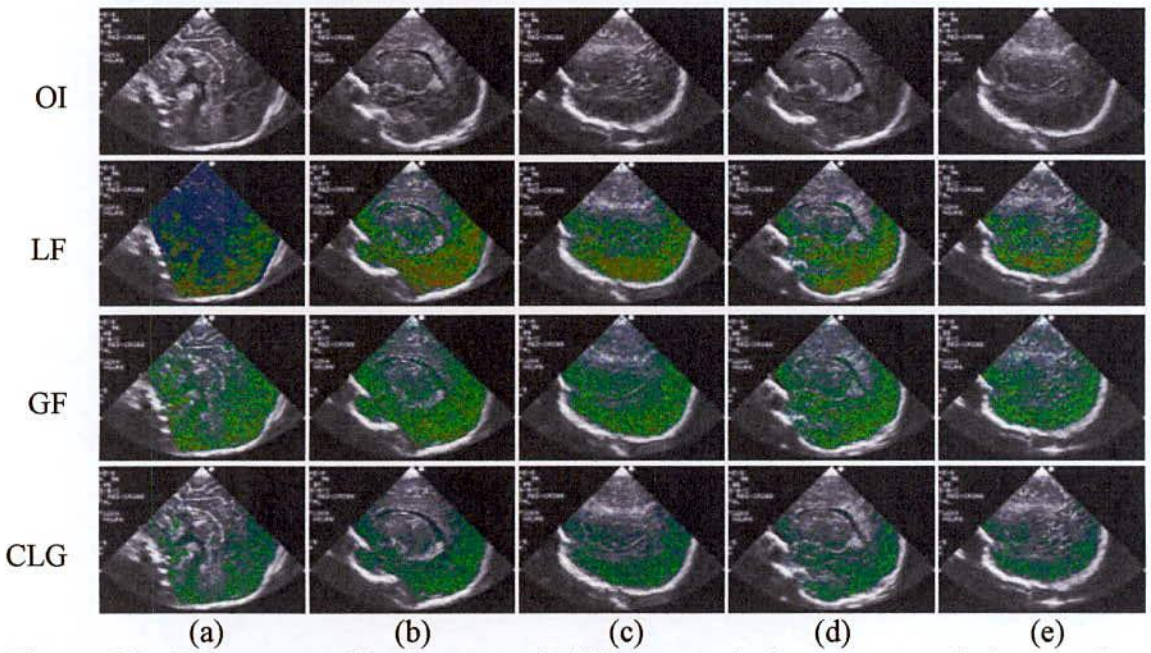

Figure 5.9: Ultrasonographic images of different sagittal sections and the overlapped frequency pulsation images using different optical flow optimization are shown. (a) Midline sagittal (b) Lateral sagittal left (c) Most Lateral sagittal left (d) Lateral sagittal right (e) Most Lateral sagittal right

5.2.5 Visualization using Fourier transform of direct pixel value

In the visualization process FFT is used for efficient computation and reduced. The frequency pulsation images are obtained from a series of B-mode ultrasonogram image with a neonate of normal development and a neonate of low birth weight (LBW) with asphyxia at birth using fast Fourier transform. These frequency pulsation images are very useful for the pediatricians in diagnosis of newborn baby's ischemic diseases. Ischemia is one of the serious diseases of newborn babies. Typical disease due to ischemia is hypoxic ischemic encephalomalacia (HIE). It is a term for brain damage caused by lack of oxygen and lack of blood flow to the brain. Once brain damage occurs, it is irreversible. The main cause of HIE is asphyxia. It is the temporal death or stoppage of the pulse, causes inadequate intake of oxygen and under supply of blood flow. It is well known that asphyxiated babies and/or LBW neonate have a high risk of ischemic diseases such as HIE. Since the blood flow of the neonate is significant, so pediatricians have great interests for observing brain tissue in asphyxia neonates through anterior fontanelle. So the frequency pulsation images are very useful in ischemia diagnostic process. FFT is used in analyses of Tissue-motion in B-mode cranial ultrasonogram. Region of interest of different coronal and sagittal sections are selected and Fig. 5.10 and 5.11 show the FFT of original ROI in case of a normal neonate and Fig. 5.12 and 5.13 show the FFT of original ROI in case of a asphyxiated neonate of different coronal and sagittal sections. Here only 3rd coefficient images of FFT are shown for different coronal and sagittal section. It is observed that strong pulsation occurs in normal neonate and weak pulsation occurs in asphyxiated neonate.

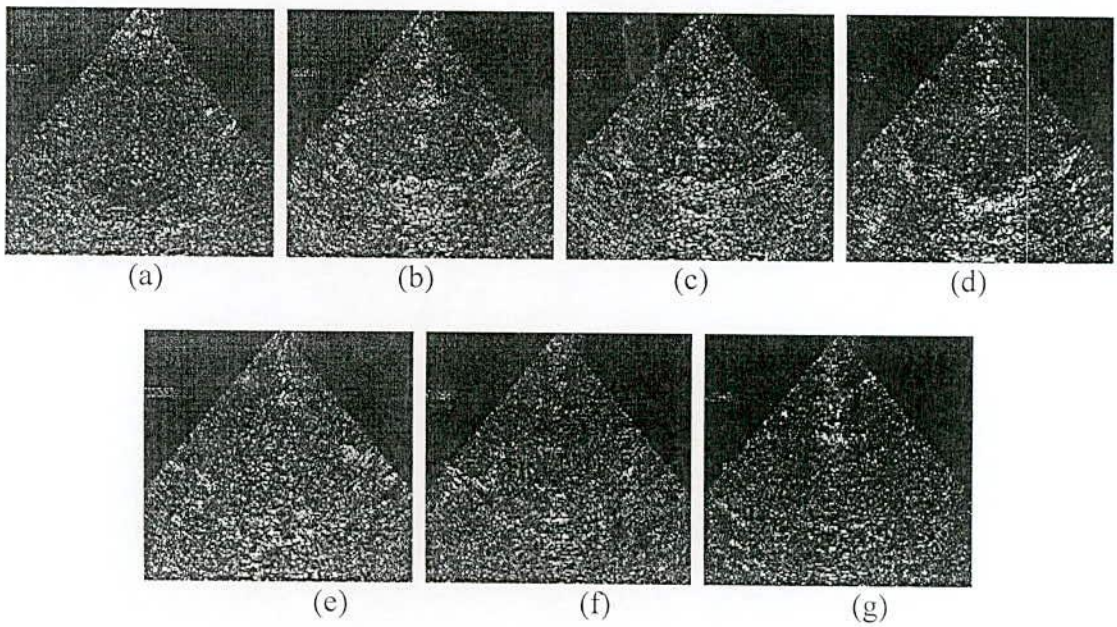

Figure 5.10: FFT of original ROI for different sections of a normal development (a) Frontal (b) Anterior coronal (c) Coronal through foramen of Monro (d) Coronal through foramen magnum (e) Slightly posterior coronal (f) Posterior coronal (g) Most posterior coronal.

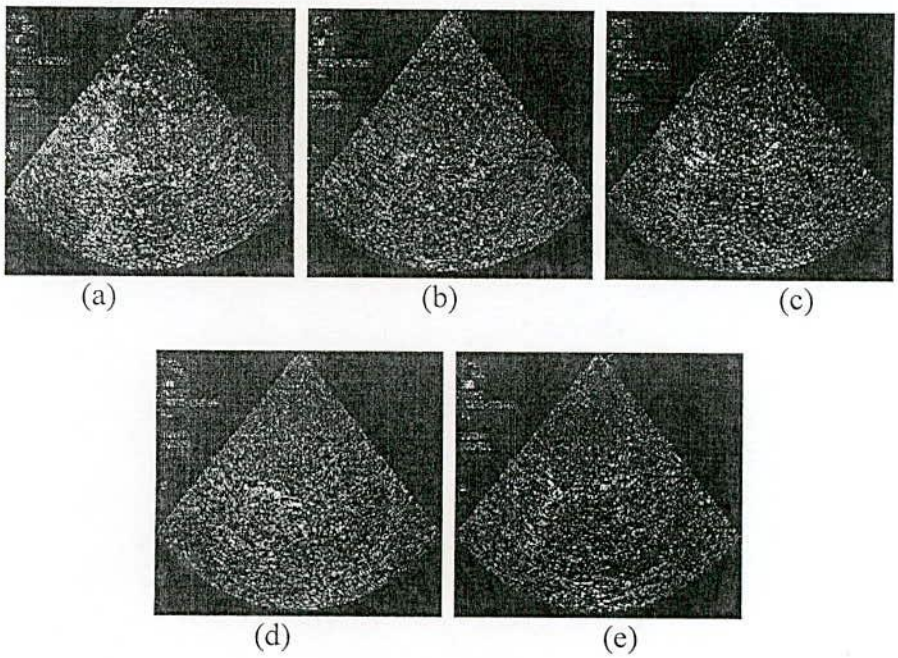

Figure 5.11: FFT of original ROI for different sagittal sections of a normal development (a) Midline sagittal (b) Lateral sagittal left (c) Most Lateral sagittal left (d) Lateral sagittal right (e) Most Lateral sagittal right

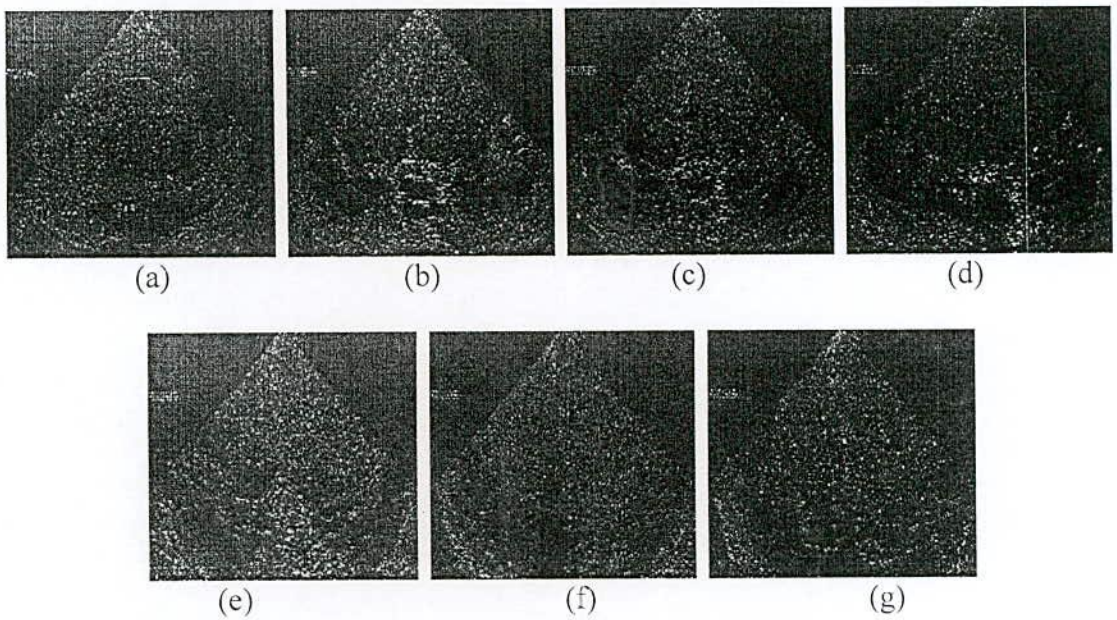

Figure 5.12: FFT of original ROI for different coronal sections of an asphyxiated neonate (a) Frontal (b) Anterior coronal (c) Coronal through foramen of Monro (d) Coronal through foramen magnum (e) Slightly posterior coronal (f) Posterior coronal (g) Most posterior coronal.

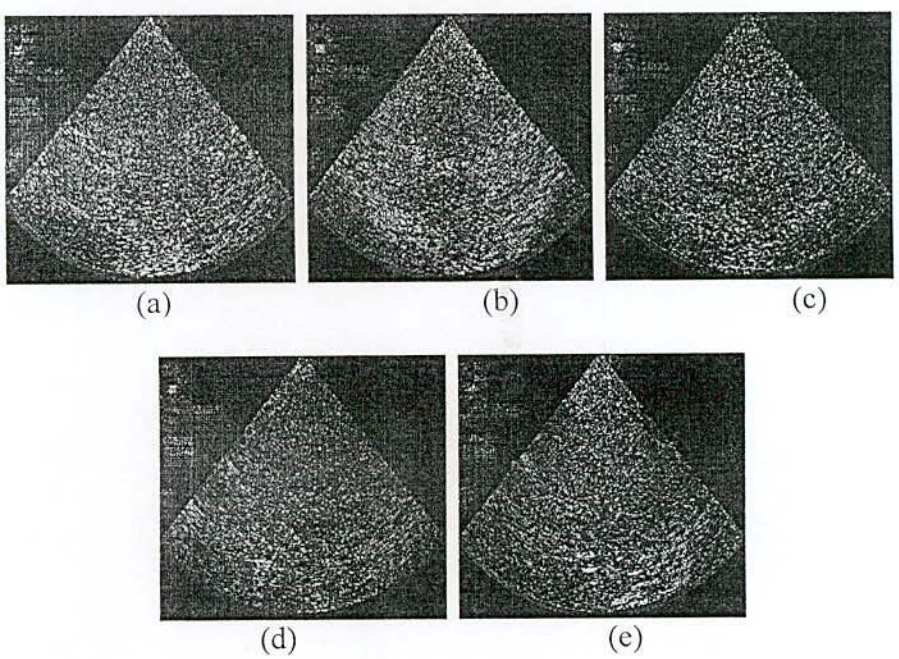

Figure 5.13: FFT of original ROI for different sagittal sections of an asphyxiated neonate (a) Midline sagittal (b) Lateral sagittal left (c) Most Lateral sagittal left (d) Lateral sagittal right (e) Most Lateral sagittal right

5.2.6 Pulsation Amplitude image

The pulsation amplitude images were obtained from a neonate of normal development and a neonate of low birth weight (LBW) with asphyxia at birth. It is well known that the asphyxiated and/or LBW neonate have a high risk of ischemic diseases such as Hypoxic-ischemic encephalomalacia. Therefore, pediatricians have great interests in blood flow of the brain tissue in asphyxiated neonates. The pulsation amplitude images are obtained by superimposition of colour gradation proportional to the amplitude of pulsation tissue-motion on the original ultrasonogram images. Pulsation amplitude images of normal development and an asphyxiated neonate of different coronal sections using Fourier transform approach is shown in Figure 5.14 and 5.15, respectively. Here only the third harmonics are shown in Figure 5.14 and 5.15. Pulsation amplitude images of normal development and an asphyxiated neonate of different sagittal sections using Fourier transform approach is shown in Figure 5.16 and 5.17, respectively. Here, the pulsation amplitude is appeared mainly along and around the middle cerebral artery and other essential arteries and organs. In the figures, red, green, and blue represent the highest, middle, and lowest strength of artery pulsation, respectively.

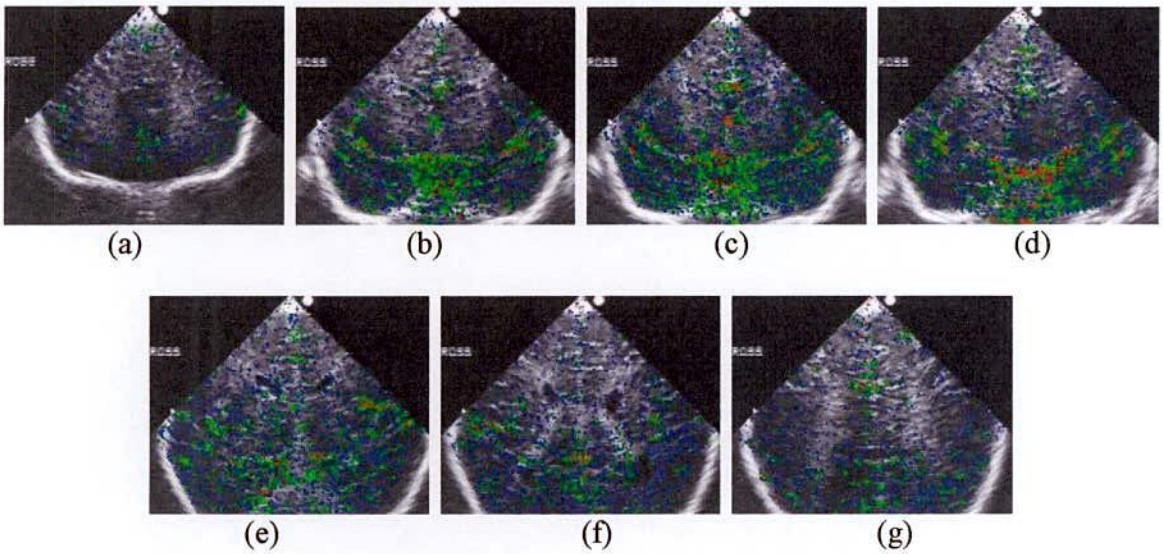

Figure 5.14: Pulsation amplitude images of normal development using Fourier transform approach. (a)Frontal (b)Anterior coronal (c) Coronal through foramen of Monro (d) Coronal through foramen magnum (e) Slightly posterior coronal (f)Posterior coronal (g)Most posterior coronal.

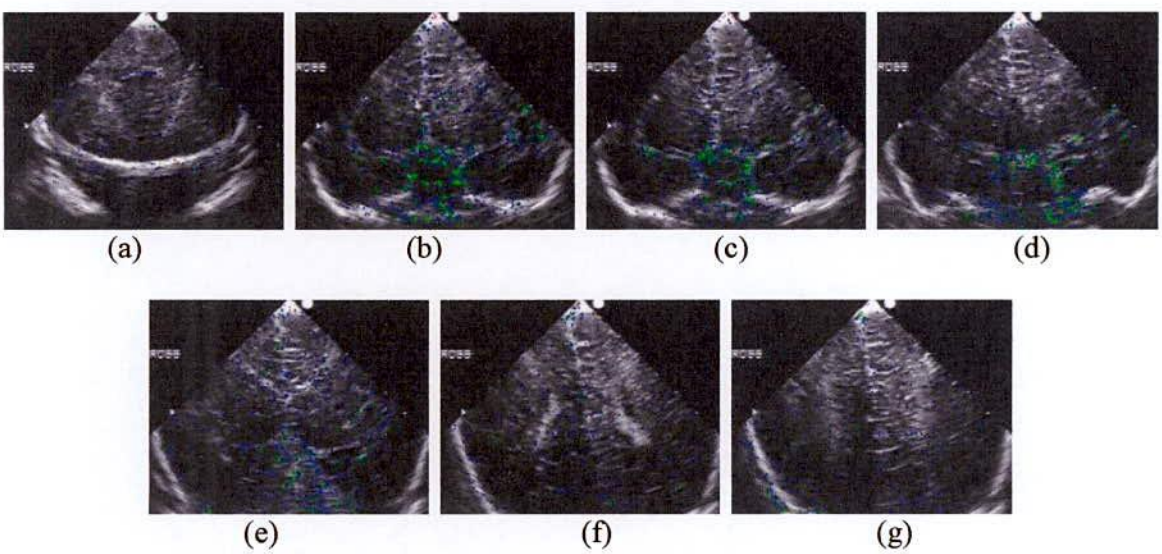

Figure 5.15: Pulsation amplitude images of asphyxiated neonate using Fourier transform approach. (a)Frontal (b)Anterior coronal (c) Coronal through foramen of Monro (d) Coronal through foramen magnum (e) Slightly posterior coronal (f)Posterior coronal (g)Most posterior coronal.

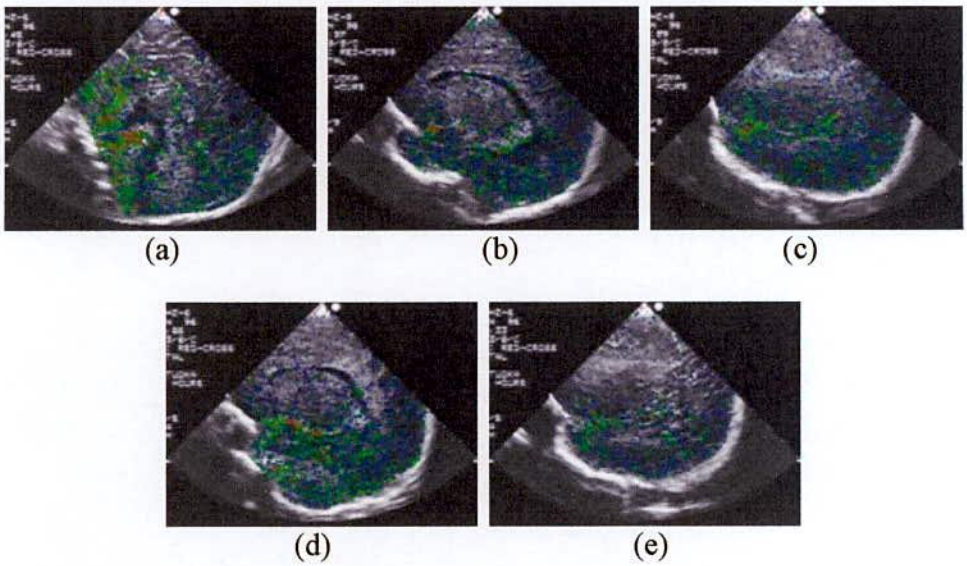

Figure 5.16: Pulsation amplitude images of different sagittal sections for normal development using Fourier transform approach. (a)Midline sagittal. (b)Lateral sagittal left (c) Most Lateral sagittal left (d) Lateral sagittal right (e) Most Lateral sagittal right

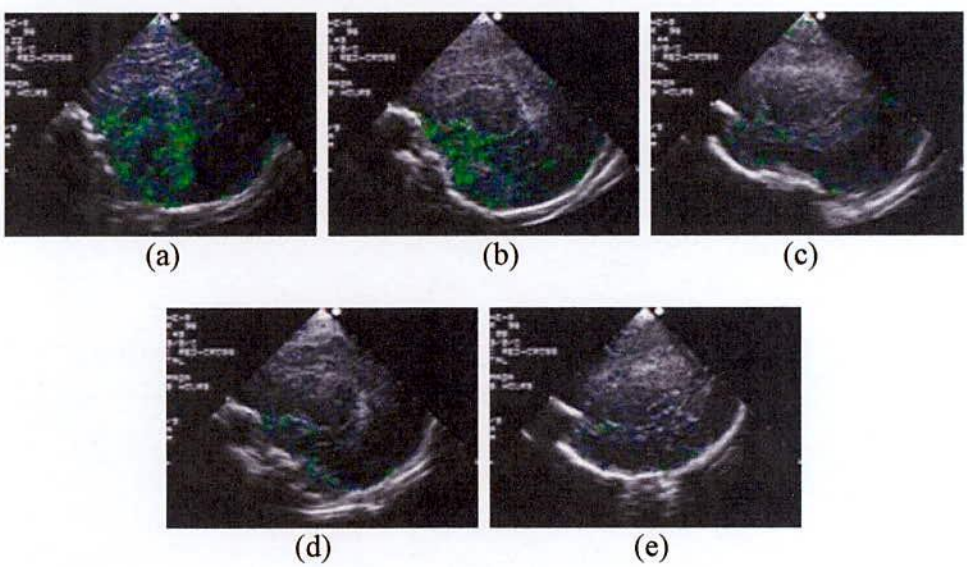

Figure 5.17: Pulsation amplitude images of an asphyxiated neonate using Fourier transform approach. (a) Anterior coronal (b) Coronal through foramen of Monro (c) Coronal through foramen magnum (d) Slightly posterior coronal (e) Midline sagittal.

CHAPTER 6

Conclusion and Future Scope

6.1 Conclusion

In this work, neonatal cranial ultrasonogram image sequences of different coronal and sagittal section are studied and neonatal brain-tissue motion due to artery pulsation are analyzed and visualized in the B-mode cranial ultrasound images for future diagnosis. There is a strong correlation of the blood flow in the newborn baby head with the artery pulsation. The tissue-motion has a relationship with artery pulsation. The tissue-motion are successfully computed by using different optical flow methods, such as: optical flow with local optimization, optical flow with global optimization for characterizing the brain tissue motion in neonatal cranium due to artery pulsation. Both local and global optimization method have some limitations. In this thesis a novel method is proposed to estimate the tissue motion quantitatively by combining local and global motion estimation methods namely combined local-global (CLG) optical flow technique in cranial ultrasonogram of newborn babies. Since tissue-motion are not affected by spatial variation of image brightness, therefore the strength of artery pulsation can be quantitatively estimated by using the magnitude of tissue-motion velocity.

CLG optical flow shows less error pixel and error values compared to local or global optimization of optical flow. CLG optical flow can overcome the difficulty of either local or global flows. Therefore, CLG optical flow method is more suitable for characterizing artery pulsation quantitatively without losing the benefits of local and global method.

The ultrasound images were also analyzed by using Fourier transform. It is found that the pulsation is associated with blood flow which periodically changes with heartbeat, which is verified by using Fourier transform of time variant tissue motion velocity. Strong pulsations are found at a harmonics of heartbeat frequencies and amplitude spectrums in other frequencies are also obtained, since the tissue motions are not sinusoidal.

The pixel value variation of the ultrasonogram images are also used for visualizing the amplitude spectrum images. We proposed pulsation amplitude image obtained by superimposition of color gradation proportional to the amplitude of pulsation tissue-motion on the original ultrasonogram only at which the strength of pulsation tissue-motion

exceeds a proper threshold. Several threshold values were used for checking the significant tissue motion in the ultrasound image sequences.

The analysis has the advantages of observing pulsation amplitude that may strongly contribute paediatricians in diagnosis of newborn baby's ischemic diseases. In the proposed method, different coronal and sagittal sections of normal neonatal cranial and asphyxiated neonatal cranial are checked. The strength of pulsation for different time interval after the birth of neonate can be achieved by the visualization of pulsation amplitude at different harmonic frequencies. Since it was confirmed by a paediatrician that the pulsation amplitude image reveals significant difference between normal and asphyxiated neonates, therefore, it can be concluded that our proposed method is useful for paediatric diagnosis.

6.2 Future Scope

The tissue-motion in neonatal cranium using different optical flow optimization techniques have been analysed and visualized successfully. The frequencies of pulsation of tissue motion are also analysed using fast Fourier transform of optical flow velocity and direct pixel value. But these analyses of tissue motion have the limitations to the discontinuity of the pixel values and the time-frequency information at the same time. Fourier Transform only gives which frequency components exist in the signal. The time and frequency information cannot be seen at the same time. So time-frequency representation of the signal is needed. Short-time Fourier transform can be used for this purpose but it has the limitations, such as unchanged window, dilemma of resolution. Narrow window causes poor frequency resolution and wide window causes poor time resolution and Heisenberg uncertainty principle. Wavelet transform has the advantages of changing the width of the window as the transform is computed for every spectral component, hence altered resolutions are placed and greater accuracy is obtained when signals are associated with some discontinuities.

Future work includes precise and automatic detection and estimation of artery pulsation from noisy cranial ultrasound image sequences and the quantitative analysis amplitude, phase, and power of pulsation for all coronal and sagittal sections and to correlate among them. More works will include the pulsation for poor optimized conditions.

REFERENCES

[1] http://emedicine.medscape.com/article/973501-overview

[2] Ramesh Agarwal, Ashish Jain, Ashok Deorari, Vinod K Paul "Post-resuscitation management of asphyxiated neonates" AIIMS- NICU protocols 2007.

[3] Y. Kitsunezuka and H. Nakamora, "Syonika-Rinsyo", vol. 38, pp. 297-308, [in Japanese], 1985.

[4] M. Yamada, M. Fukuzawa, Y. Kitsunezuka, J. Kishida, N. Nakamori, H. Kanamori, T. Sakurai and S. Kodama, "Pulsation detection from noisy ultrasound echo moving images of newborn baby head using Fourier transform," Jpn. J. Appl. Phys., vol. 34, p. 2854–2856, 1995.

[5] M. Fukuzawa, Y. Kitsunezuka and M. Yamada, "A real-time processing system for pulsation detection in neonatal cranial ultrasonogram," Jpn. J. Appl. Physics, vol. 37, pp. 3106–3109, 1998.

[6] M. Fukuzawa, M. Yamada, "Real time processing of ultrasound echo moving images using one dimensional processor array," Proceedings of the International Symposium on Future of Intellectual Electronics (ISFIIE), Sendai international center, Sendai, Japan, March, 1999

[7] M. Fukuzawa, Y. Kitsunezuka, S. Kodama and M. Yamada, "Distribution of artery pulsation in cranial ultrasonogram of newborn baby with intraventricular hemorrhage," MII, vol. 16, No.2, May 1999.

[8] Berthold K. P. Horn and Brian G. Schunck, "Determining optical flow", Artificial Intelligence 17, pp.185-203, 1981.

[9] Brian G. Schunck, "The image flow constraint equation", Computer Vision, Graphics & Image Processing, vol. 35, pp. 20-46, 1986.

[10] B. G. Schunck, "Image flow segmentation and estimation by constraints line clustering", IEEE trans. Pattern Analysis and Machine Intelligence, vol.11, pp. 1010-1027, October 1989.

[11] J. K. Kearney, W.B. Thompson and D.L. Boley, "Optical flow estimation: an error analysis of gradient-based method with local optimization", IEEE trans. Pattern Analysis and Machine Intelligence, vol.9, pp. 229-244, March 1987.

[12] M. Ahmad, M. S. Yusuf, M. Z. Chowdhury, and M. Yamada, "Global optimization of optical flow technique on the computation of tissue-motion in neonatal cranial ultrasonogram," Journal of Electrical & Electronic Engg, Istanbul University, vol. 4, no. 1, pp. 1007–1016, 2004.

[13] M. Fukazawa, H. Kubo, Y. Kitsunezuka, and M. Yamada, "Motion analysis of artery pulsation in neonatal cranial ultrasonogram," Proc. of SPIE, vol. 3661, pp. 122–130, 1999.

[14] M. Ahmad, T. Taslima, L. Lata, and M. Yamada, "A combined local-global optical flow approach for cranial ultrasonogram image sequence analysis," Proc. of ICCIT, pp. 323–328, Khulna, Bangladesh, 2008.

[15] G. van Wezel-Meijler, "Neonatal Cranial Ultrasonography", Springer, Berlin Heidelberg, Newyork, 2007

[16] E. Enkelmann, "Investigation of multigrid algorithms for the estimation of optical flow fields in image sequences," Computer Vision, Graphics & Image processing, vol.43,pp.150-177,1998

[17] A. Del Bimbo, P. Nesi and Jorge L.C. Sanz, " Analysis of optical flow Constraint", IEEE Trans. on Image Processing, vol.4, no.4,pp.460-469, April 1995.

[18] A. D. Bimbo, P. Nesi and J. L.C. Sanz, "Optical flow computation using extended constraints", IEEE Trans. on Image Processing, vol.5, no.5,pp.720-739, May 1996

[19] H. H. Nagel, "Displacement vector derived from second order intensity variations in image sequences", Computer Vision, Graphics, and Image Processing, vol.21, pp.85-117, 1983.

[20] J. H. Duncan and T.-C. Chou, "On the detection of motion and computation of optical flow", IEEE transactions on Pattern analysis and Machine intelligence, vol. 14, no. 3, pp. 346-352, March 1992.

[21] H. H. Nagel, "On the Estimation of optical flow: Relations between different approaches and some new results", Artificial intelligence, vol.33, pp.299-324, January 1987.

[22] Masanobu Yamamoto, "A general aperture problem for direct estimation of 3-D motion parameters," IEEE transactions on Pattern analysis and Machine intelligence, Vol. 11, no. 5, pp. 529-536, May 1989.

[23] M. Subbarao, "Interpretation of image flow: a spatio-temporal approach," IEEE Trans. Pattern Analysis and Machine Intelligence, vol.11, no.3, pp.266-278, March, 1989.

[24] Masahiko Yachida, "Determining velocity maps by spatio-temporal neighborhoods from image sequences," Computer Vision, Graphics & Image Processing, vol.21, pp.262-279, 1983.

[25] M. G. Strintzis and I. Kokkinidis, "Maximum likelihood Motion estimation in ultrasound image sequences", IEEE Signal Processing Letters, vol.4, no. 6, pp. 156-157, June 1997.

[26] H. H. Nagel and W. Enkelmann, "An investigation of smoothness constraints for the estimation of displacement vector fields from image sequences," IEEE Trans. Pattern Analysis and Machine Intelligence, vol. PAMI-8, no.5, pp. 565-593, September, 1986.

[27] A. Bruhn, J. Weikert, and C. Schnorr, "Lucas-Kanade meets Horn and Schucnk: combining local and global optic flow methods," Int'l J. Computer Vision, vol. 61, no. 3, pp. 211-231, 2005.

[28] B. Lucas and T. Kanade, "An iterative image registration technique with an application to stereo vision," In Proc. Seventh Int'l Joint Conf. on Artificial Intelligence, pp. 674-679, Vancouver, Canada, 1981.

[29] S. Salivahanan, A. Vallavaraj, and C Gnanapriya, "Digital Signal Processing," Tata McGraw-Hill Publication, 2002.

[30] M. Ahmad, M. M. Islam, L. Lata, T. Taslima and M. Yamada, "CLG optical flow approach and frequency analysis of cranial ultrasonogram image sequences" Journal of Multimedia, Vol. 5, pp. 47-54, February 2010.

[31] M. M. Islam, M. Ahmad, and M. Yamada, "Analysis and visualization of pulsation in B-mode cranial ultrasound images," Proc. 6th International Conference on Electrical & Computer Engineering (ICECE) 2010, December 18-20, 2010, Dhaka, Bangladesh, pp. 494-497.

[32] M. Ahmad, M. A. Khan, M. M. Islam, and M. Yamada, "Neonatal Brain Pulsation Strength Analysis using Wavelet Transform," Proc. 6th International Conference on Electrical & Computer Engineering (ICECE), December 18-20, 2010, Dhaka, Bangladesh, pp. 167-170.

[33] D. S. Babcock and B. K. Han, "Cranial ultrasonography of infants," Williams and Wilkins, Baltimore, USA, 1982.

APPENDIX

APPENDIX I. Calculation of v_x and v_y by Local optimization method

From equation (4.4.10) we can define

$$\Delta = \begin{vmatrix} \sum \frac{\partial p}{\partial x}\frac{\partial p}{\partial x} & \sum \frac{\partial p}{\partial x}\frac{\partial p}{\partial y} \\ \sum \frac{\partial p}{\partial x}\frac{\partial p}{\partial y} & \sum \frac{\partial p}{\partial y}\frac{\partial p}{\partial y} \end{vmatrix}$$

$$\Delta 1 = \begin{vmatrix} -\sum \frac{\partial p}{\partial t}\frac{\partial p}{\partial x} & \sum \frac{\partial p}{\partial x}\frac{\partial p}{\partial y} \\ -\sum \frac{\partial p}{\partial t}\frac{\partial p}{\partial y} & \sum \frac{\partial p}{\partial y}\frac{\partial p}{\partial y} \end{vmatrix}$$

$$\Delta 2 = \begin{vmatrix} \sum \frac{\partial p}{\partial x}\frac{\partial p}{\partial x} & -\sum \frac{\partial p}{\partial t}\frac{\partial p}{\partial y} \\ \sum \frac{\partial p}{\partial x}\frac{\partial p}{\partial y} & -\sum \frac{\partial p}{\partial t}\frac{\partial p}{\partial y} \end{vmatrix}$$

Now the flow velocity components are

$$v_x = \frac{\Delta 1}{\Delta}$$

$$v_y = \frac{\Delta 2}{\Delta}$$

The approximated value of $v_x(i,j,k)$ and $v_y(i,j,k)$ at any pixel location in the local region can be determined by the following summation

$$v_x(i,j,k) = \frac{\Sigma_i \Sigma_j \left(\frac{\partial p}{\partial x}\right)\left(\frac{\partial p}{\partial y}\right) \Sigma_k \Sigma_j \left(\frac{\partial p}{\partial t}\right)\left(\frac{\partial p}{\partial y}\right) - \Sigma_j \Sigma_j \left(\frac{\partial p}{\partial y}\right)^2 \Sigma_k \Sigma_i \left(\frac{\partial p}{\partial t}\right)\left(\frac{\partial p}{\partial x}\right)}{\Sigma_i \Sigma_i \left(\frac{\partial p}{\partial x}\right)^2 \Sigma_j \Sigma_j \left(\frac{\partial p}{\partial y}\right)^2 - \left(\Sigma_i \Sigma_j \left(\frac{\partial p}{\partial x}\right)\left(\frac{\partial p}{\partial y}\right)\right)^2}$$

$$v_y(i,j,k) = \frac{\Sigma_i \Sigma_j \left(\frac{\partial p}{\partial x}\right)\left(\frac{\partial p}{\partial y}\right) \Sigma_k \Sigma_j \left(\frac{\partial p}{\partial t}\right)\left(\frac{\partial p}{\partial x}\right) - \Sigma_i \Sigma_i \left(\frac{\partial p}{\partial x}\right)^2 \Sigma_k \Sigma_j \left(\frac{\partial p}{\partial t}\right)\left(\frac{\partial p}{\partial y}\right)}{\Sigma_i \Sigma_i \left(\frac{\partial p}{\partial x}\right)^2 \Sigma_j \Sigma_j \left(\frac{\partial p}{\partial y}\right)^2 - \left(\Sigma_i \Sigma_j \left(\frac{\partial p}{\partial x}\right)\left(\frac{\partial p}{\partial y}\right)\right)^2}$$

APPENDIX II. Calculation of v_x and v_y by Global optimization method

From equation(4.4.22) , let us define

$$\Delta=\begin{bmatrix}\frac{\partial^2 p}{\partial x^2}+\alpha^2 & \frac{\partial p}{\partial x}\frac{\partial p}{\partial y}\\ \frac{\partial p}{\partial x}\frac{\partial p}{\partial y} & \alpha^2+\frac{\partial^2 p}{\partial y^2}\end{bmatrix};\Delta 1=\begin{bmatrix}\alpha^2\overline{v_x}-\frac{\partial p}{\partial x}\frac{\partial p}{\partial t} & \frac{\partial p}{\partial x}\frac{\partial p}{\partial y}\\ \alpha^2\overline{v_y}-\frac{\partial p}{\partial y}\frac{\partial p}{\partial t} & \alpha^2+\frac{\partial^2 p}{\partial y^2}\end{bmatrix};\Delta$$

$$=\begin{bmatrix}\frac{\partial^2 p}{\partial x^2}+\alpha^2 & \alpha^2\overline{v_x}-\frac{\partial p}{\partial x}\frac{\partial p}{\partial t}\\ \frac{\partial p}{\partial x}\frac{\partial p}{\partial y} & \alpha^2\overline{v_y}-\frac{\partial p}{\partial y}\frac{\partial p}{\partial t}\end{bmatrix}$$

Now Δ can be written as,

$$\Delta=\left(\frac{\partial^2 p}{\partial x^2}+\alpha^2\right)\left(\alpha^2+\frac{\partial^2 p}{\partial y^2}\right)-\left(\frac{\partial p}{\partial x}\frac{\partial p}{\partial y}\right)^2=\alpha^2\left(\alpha^2+\frac{\partial^2 p}{\partial x^2}+\frac{\partial^2 p}{\partial y^2}\right)$$

$$v_x=\frac{\Delta 1}{\Delta}=\frac{\alpha^2\left(\alpha^2\overline{v_x}+\frac{\partial^2 p}{\partial y^2}\overline{v_x}-\frac{\partial p}{\partial x}\frac{\partial p}{\partial y}\overline{v_y}-\frac{\partial p}{\partial t}\frac{\partial p}{\partial x}\right)}{\alpha^2\left(\alpha^2+\frac{\partial^2 p}{\partial x^2}+\frac{\partial^2 p}{\partial y^2}\right)}=\frac{\alpha^2\overline{v_x}+\frac{\partial^2 p}{\partial y^2}\overline{v_x}-\frac{\partial p}{\partial x}\frac{\partial p}{\partial y}\overline{v_y}-\frac{\partial p}{\partial t}\frac{\partial p}{\partial x}}{\alpha^2+\frac{\partial^2 p}{\partial x^2}+\frac{\partial^2 p}{\partial y^2}}$$

$$or\ v_x=\frac{\overline{v_x}\left(\alpha^2+\frac{\partial^2 p}{\partial x^2}+\frac{\partial^2 p}{\partial y^2}\right)-\frac{\partial p}{\partial x}\left(\frac{\partial p}{\partial x}\overline{v_x}+\frac{\partial p}{\partial y}\overline{v_y}+\frac{\partial p}{\partial t}\right)}{\alpha^2+\frac{\partial^2 p}{\partial x^2}+\frac{\partial^2 p}{\partial y^2}}$$

$$\therefore v_x=\overline{v_x}-\frac{\frac{\partial p}{\partial x}\left(\frac{\partial p}{\partial x}\overline{v_x}+\frac{\partial p}{\partial y}\overline{v_y}+\frac{\partial p}{\partial t}\right)}{\alpha^2+\frac{\partial^2 p}{\partial x^2}+\frac{\partial^2 p}{\partial y^2}}$$

$$v_y=\frac{\Delta 2}{\Delta}=\frac{\alpha^2\left(\alpha^2\overline{v_y}+\frac{\partial^2 p}{\partial x^2}\overline{v_y}-\frac{\partial p}{\partial x}\frac{\partial p}{\partial y}\overline{v_x}-\frac{\partial p}{\partial t}\frac{\partial p}{\partial y}\right)}{\alpha^2\left(\alpha^2+\frac{\partial^2 p}{\partial x^2}+\frac{\partial^2 p}{\partial y^2}\right)}=\frac{\alpha^2\overline{v_y}+\frac{\partial^2 p}{\partial x^2}\overline{v_y}-\frac{\partial p}{\partial x}\frac{\partial p}{\partial y}\overline{v_x}-\frac{\partial p}{\partial t}\frac{\partial p}{\partial y}}{\alpha^2+\frac{\partial^2 p}{\partial x^2}+\frac{\partial^2 p}{\partial y^2}}$$

$$or\ v_y=\frac{\overline{v_y}\left(\alpha^2+\frac{\partial^2 p}{\partial x^2}+\frac{\partial^2 p}{\partial y^2}\right)-\frac{\partial p}{\partial y}\left(\frac{\partial p}{\partial x}\overline{v_x}+\frac{\partial p}{\partial y}\overline{v_y}+\frac{\partial p}{\partial t}\right)}{\alpha^2+\frac{\partial^2 p}{\partial x^2}+\frac{\partial^2 p}{\partial y^2}}$$

$$\therefore v_y=\overline{v_y}-\frac{\frac{\partial p}{\partial y}\left(\frac{\partial p}{\partial x}\overline{v_x}+\frac{\partial p}{\partial y}\overline{v_y}+\frac{\partial p}{\partial t}\right)}{\alpha^2+\frac{\partial^2 p}{\partial x^2}+\frac{\partial^2 p}{\partial y^2}}$$